ENGINEERED MARROW MACROPHAGES FOR CANCER THERAPY: ENGORGEMENT, ACCUMULATION, DIFFERENTIATION, AND ACQUIRED IMMUNITY

Cory Michael Alvey

A DISSERTATION
In
Pharmacology

Presented to the Faculties of the University of Pennsylvania in Partial Fulfillment of the Requirement for the Degree of Doctor of Philosophy

2017

Supervisor of Dissertation

_____

Dr. Dennis E. Discher, Ph.D, Robert D. Bent Professor of Chemical and Biomolecular Engineering

Graduate Group Chairperson

_____

Dr. Julie A. Blendy, Ph.D. Professor of Pharmacology

Dissertation Committee

Dr. Jeffrey M. Field, Ph.D. Professor of Pharmacology
Dr. Vladimir Muzykantov, M.D., Ph.D., Professor of Pharmacology
Dr. Wenchao Song, Ph.D. Professor of Pharmacology
Dr. Ellen Pure, Ph.D. Professor of Biomedical Sciences

ENGINEERED MARROW MACROPHAGES FOR CANCER THERAPY: ENGORGEMENT, ACCUMULATION, DIFFERENTIATION, AND ACQUIRED IMMUNITY

ACKNOWLEDGEMENTS

I would like to express my sincere gratitude to my mentor and thesis advisor Dr. Dennis Discher for believing in me and taking me in his laboratory to pursue my dissertation. I am fortunate to work with a mentor who is a champion of cross-disciplinary approaches to medical research. Though his approach of, "let's have three progress updates a day" was intense, it was this tactic that kept me on my toes and allowed me to make great progress with my publications. I am grateful that he was open to many ideas I proposed and allowed me to pursue them. His ability to interact with each of the laboratory members with equal intensity, in addition to his large family, made a strong impression on me.

I would also like to thank all members of my thesis committee: Dr. Jeff Fields, Dr. Vladimir Muzykantov, Dr. Wenchao Song, and Dr. Ellen Pure for their guidance and support throughout my graduate career. Each meeting with my committee was productive and helped me significantly with the development of my thesis work.

I would like to thank the University of Pennsylvania Pharmacology Program with a specific shout-out to the class of 2017. My first year here was my hardest and you made it easier to push through those difficult times.

Within the work environment, I would like to thank my colleagues and friends: Dr. Jerome Irianto, Dr. Lucas Smith, Dr. Manu Tewari, Dr. Dave Dingal, Dr. Nisha Sosale, Dr. Kyle Spinler, Dr. Praful Nair, Charlotte Pfeifer, Yuntao Xia, SangKun Cho, Jake Hsu, and Brandon Hayes for productive discussions on research and other non-work-related matters throughout my time in the Discher laboratory. You made it a pleasure to come

into work day after day. I couldn't have asked for better co-workers and friends. Throughout my life, I will never forget the times we shared. I wish you all the best!

I would like to give special thanks to my close friend Ian Johnston. I can't imagine a better person to have shared my hobbies with during my time here in Philadelphia. I hope we stay in contact throughout our lives. I will always consider you family.

I would like to express my gratitude to my mentors outside the laboratory for their guidance throughout my professional career. Specifically, I would like to thank Dr. Mas Iimura for his mentorship and friendship throughout my years at Ripon College and beyond. We got to know each other during a time when I made the hardest decisions of my life. I was extremely lucky to have met you and truly believe I would not be where I am or the person I am today without you. I can never thank you enough.

Finally, I owe a tremendous amount of gratitude to my family. To one of the most important people in my life, my mom, thank you for believing in me and supporting me throughout my entire life despite being overwhelmed with the dreams I had for myself. You are the strongest person I know and it is your strength that I admire most about you and hope I've inherited. You've had a hard life and have done far too much for your family with little in return. I will do everything I can to repay you and give you the gratitude you deserve. Lastly, I would like to thank the love of my life, Elizabeth. No matter the sense of accomplishment I feel from my achievements in life, they will never compare to the love I have for you. You will always be the most important person in my life. You are an incredible person and I couldn't have wished for a better partner with whom to share my life.

ABSTRACT

ENGINEERED MARROW MACROPHAGES FOR CANCER THERAPY: ENGORGEMENT, ACCUMULATION, DIFFERENTIATION, AND ACQUIRED IMMUNITY

Cory M. Alvey

Dennis E. Discher

The ability of a macrophage to engulf and break down invading cells and other targets provides a first line of immune defense in nearly all tissues. This defining ability to 'phagos' or devour can subsequently activate the entire immune system against foreign and diseased cells, and progress is now being made on a decades-old idea of directing macrophages to phagocytose specific targets such as cancer cells. Physical properties of cancer cells influence phagocytosis and relate via cytoskeleton forces to differentiation pathways in solid tumors. Here, SIRPα on macrophages from mouse and human marrow was inhibited to block recognition of CD47, a 'marker of self.' These macrophages were then systemically injected into mice with fluorescent human tumors. Within days, the tumors regressed, and fluorescence analyses showed that the more the SIRPα-inhibited macrophages engulfed, the more they accumulated within tumors. *In vitro* phagocytosis experiments on transwells revealed that macrophage migration through micropores was inhibited by eating. However, during the 1-2 weeks of tumor residency, donor macrophages quickly differentiated toward non-phagocytic, high-SIRPα tumor associated macrophage. Analyses of macrophages on soft or stiff collagenous gels demonstrated a stiffness-driven upregulation of SIRPα. Tissue stiffness also seems to have a role in the

development of cancer. Meta-analyses suggest that genomic variation across tumors scales with the stiffness of the tumor tissue of origin. These genomic changes give rise to neoantigens that are important for the development of monocyte/macrophage immunotherapies. Indeed, marrow-derived macrophages can phagocytose melanoma cells and present neoantigens leading to the activation of T-cells. Unlike past injections of anti-CD47 which cause anemia, no measurable impact on blood profiles, weight, or development of GvHD was observed from systemic injections of SIRPα-inhibited donor macrophages.

TABLE OF CONTENTS

LIST OF TABLES

LIST OF FIGURES

LIST OF ABBREVIATIONS

7-AAD: 7-Aminoactinomycin D
Ab: Antibody
APB MΦ: antibody opsonized cancer cell plus SIRPα blocked macrophage
A'PB MΦ: Antibody Fc primed macrophage plus SIRPα block
ATCC: American Type Culture Collection
BFU-E: Erythroid Burst-Forming Units
BM: Bone Marrow
BMT: Human Bone Marrow Transplantation
BSA: Bovine Serum Albumin
C: Celsius
CD: Clusters of Differentiation
CFSE: Carboxy-Fluorescein Succinimidyl Ester
CFU-E: Colony Forming Unit-Erythroid
CFU-GEMM: Colony Forming Unit-Granulocyte, Erythrocyte, Monocyte and Megakaryocyte
CFU-GM: Colony Forming Unit-Granulocyte and Monocyte
CK-II: Casein Kinase-II
CMV: Cytomegalovirus
CLP: Common Lymphoid Progenitor
CMP: Common Myeloid Progenitor
CPP: Common Progenitor
DMSO: Dimethyl Sulfoxide
DNA: Deoxyribonucleic acid
EC50: Half maximal effective concentration
ECM: Extracellular Matrix
EGF: Epidermal Growth Factor
EGFR: Epidermal Growth Factor Receptor
ELC: Essential Light Chains
Epo: Erythropoietin
ESC: Embryonic Stem Cell
FcγR: fragment, crystallizable gamma Receptor
FITC: Fluorescein
G-CSF: Granulocyte Colony-Stimulating Factor
GFP: Green Fluorescent Protein
GMP: Granulocyte-Monocyte Progenitor
hCD47: human CD47
Hr: Hour
HSC/P: Hematopoietic Stem Cell/Progenitors
IC50: Half maximal inhibitory concentration

IgG: Immunoglobulin-G
IL3: Interleukin-3
ITAM: immunoreceptor tyrosine-based activating motifs
ITIM: immunoreceptotor tyrosine-based inhibitory motifs
KD or k.d.: Knockdown
Ki: Inhibition constant
kPa: Kilo-Pascal
M: Molar
mCD47: mouse CD47
MDM: Marrow derived macrophage
MEP: Megakaryocyte-Erythroid Progenitor
Min: Minutes
MK-poiesis: Megakaryopoiesis
MK: Megakaryocytes
hSIRPα: human SIRPα
μl: Microliter
μm: Micrometer
μM: Micromolar
mg: Milligram
ml: Millimeter
mM: Millimolar
MΦ: macrophage or monocyte
MHC: major histocompatibility complex
MLCK: Myosin Light Chain Kinase
Mpl: Thrombopoietin Receptor
MPP: Multi-Potent Progenitor
MPS: mononuclear phagocyte system
MSC: Mesenchymal Stem Cell
MuSC: Muscle stem cell
mSIRPα: mouse SIRPα
NK cells: Natural Killer Cells
NMM-IIA, B, C: Non-muscle myosin-II isoform A, B, C
NP-40: Nonidet P-40
NSC: Neural Stem Cell
NSG: NOD/SCID/IL-2R$\gamma^{-/-}$
OA3: ovarian cancer antigen (CD47)
OB: Osteoblast
Pa: Pascal
PAGE: Polyacrylamide Gel Electrophoresis
PEG: polyethylene glycol
PDGF: Platelet-Derived Growth Factor

PKC: Protein Kinase C
Plt: platelet
pS1943: Phosphorylation of Serine 1943 residue in NMM-IIA
RA, RAR: retinoic acid, retinoic acid receptor
RBC: Red Blood Cell
RLC: Regulatory Light Chains
ROCK: Rho-associated Protein Kinase
SD: Standard Deviation
SDF-1: Stromal Derived Factor-1
Sec: Seconds
SEM: Standard Error Mean
SHP1: Src homology region 2 domain-containing phosphatase-1
shRNA: short-hairpin ribonucleic acid
siRNA: small interfering ribonucleic acid
SIRPα: signal-regulatory protein alpha
TAM: tumor associated macrophages
TGF-beta: Transforming Growth Factor-beta
Tpo: Thrombopoietin
Vs: Versus
WT: Wild-Type

Note: The text adheres to nomenclature standards but might sometimes add a species designator. For example, hCD47 and *CD47* symbolize human protein and gene, whereas mCD47 and *Cd47* symbolize mouse protein and gene.

Chapter 1: Introduction

1.1 SIGNIFICANCE

It was once thought that failure of a macrophage to engulf a cancer cell reflects the absence of an activation signal by surface opsonization from IgG molecules. However, it is now understood that 'eat me' signals are balanced by the presence of 'don't eat me' signals or 'self' markers (Oldenborg *et al.*, 2000). Within the last few decades, numerous 'self' markers have been discovered that inhibit immune cell destruction of healthy cells. The 'self' markers, PD-L1 and CD47, have been of interest to researchers because of their inhibitory effects on T-cells and macrophages, respectively, and how these markers relate to cancer progression (Strickland *et al.*, 2016). Macrophages are particularly exciting as they are abundant and motile in solid tumors (Chaturvedi *et al.*, 2014; Condeelis & Pollard, 2006; Lu-emerson *et al.*, 2013) compared to T-cells which minimally infiltrate (Fousek & Ahmed, 2015; Joyce & Fearon, 2015; Salmon *et al.*, 2012). These observations help explain the poor clinical trial outcomes for T-cell therapy of solid tumors (Kakarla & Gottschalk, 2014; Nicol *et al.*, 2011). Unfortunately, macrophage-based therapy has its own challenges. It is well-established that the density of the 'tumor associated macrophage' (TAM) has been linked to promoting tumor growth, angiogenesis, and inhibiting other immune effector cells (Colegio *et al.*, 2014; Fujiwara *et al.*, 2011; Lan *et al.*, 2012; Lu-emerson *et al.*, 2013; Y. Zhang *et al.*, 2013). Clinical data supports these observations as high TAM density is correlated with poor prognosis (Leek *et al.*, 1996). The term 'tumor-associated macrophage' is perhaps a misnomer in the strict sense that a macrophage should 'phagos' or eat foreign or diseased (cancerous) cells. However, these cells seem to have lost most or all of their ability to destroy cancerous cells.

How any cell, including a cancer cell, avoids being engulfed by an activated macrophage could partially involve signaling by "marker of self" CD47 to the phagocyte's receptor SIRPα (Bruce *et al.*, 2002; P. Oldenborg *et al.*, 2000; Tsai & Discher, 2008). It is now well established that cancer cells overexpress 'self' markers such as PD-L1 and CD47 (Majeti *et al.*, 2009; Posey *et al.*, 2016; Sockolosky *et al.*, 2016; Willingham *et al.*, 2012). Recent studies suggest that common oncogenes, such as MYC, are selected for based on their transcriptional control over 'self' markers (Casey *et al.*, 2016). *In vivo* knockdown of mCD47 in tumors can slow tumor growth with an implication for macrophages as the primary effector cell as systemic poisoning of macrophages eliminates the growth suppression (Wang *et al.*, 2013). Human tumors in mice also shrink after systemic injection of anti-hCD47 in combination with a distinct Ab that opsonizes the human cancer cells (e.g. (Chao *et al.*, 2010)).

Based on these preclinical studies, human clinical trials using CD47 blockade for cancer therapy have been rapidly emerging. These trials rely on TAMs and perhaps infiltrating monocytes that are partially or fully inhibited from recognizing tumors as self (Chao *et al.*, 2010; Willingham *et al.*, 2012). Most preclinical models show CD47 disruption alone is insufficient (Chao *et al.*, 2010; Weiskopf *et al.*, 2013), requiring an additional pro-phagocytic signal (like a foot on the gas pedal) to drive phagocytosis of cancer cells by TAMs. Anti-CD47 antibodies had once been thought sufficient to inhibit CD47 and activate phagocytosis through Fc engagement, but results are mixed, at best, even when combined with tumor pro-phagocytic signals such as calreticulin and phosphatidylserine (Chao *et al.*, 2010; Feng *et al.*, 2015; Lundqvist *et al.*, 2008; Rettig *et al.*, 1999). One recent study (Horrigan *et al.*, 2017; Willingham *et al.*, 2012) failed to

replicate any efficacy with anti-mCD47 inhibition alone and questioned the statistical significance of past data (Horrigan *et al.*, 2017; Willingham *et al.*, 2012). Direct measurements of cancer cell engulfment by macrophages in tumors could help address these conflicting reports, but these measurements are severely lacking. In addition to concerns of efficacy, safety is also an issue as CD47 is expressed on all cells, and so species-matched anti-CD47 injections (e.g. anti-mCD47 into mouse) cause rapid and reproducible depletion of blood cells (Willingham *et al.*, 2012). Initial clinical trials of anti-hCD47 safety likewise motivate a concentrated and thorough study of the basic biology and coupling of macrophage trafficking, phagocytosis with 'self'-inhibition, and differentiation in tumors.

1.2 THESIS OUTLINE

Given the concerns surrounding TAMs as possible effector cells in anti-CD47 therapy, chapter 2 focuses on the progress made using adoptive transfer of macrophages to treat cancer and whether it could be a novel approach when combined with inhibition of CD47-SIRPα. Upon investigation of adoptive macrophage literature, it was clear that over the past four to five decades adoptive macrophages have been found to be safe, albeit ineffective, in anti-cancer therapy (Andreesen, Hennemann, & Krause, 1998; Chokri *et al.*, 1992; Lacerna, Stevenson, & Stevenson, 1988). However, a majority of these studies were conducted prior to the discovery of 'marker of self' CD47 (Oldenborg *et al.*, 2000), which inhibits phagocytosis by turning off cytoskeletal myosin-II (Tsai & Discher, 2008). One recent study reported that knockdown of SIRPα in macrophages accelerates tumor growth and alters macrophage phenotype (Pan *et al.*, 2013), but it is unclear whether

antibody blockade of SIRPα along with tumor opsonization would produce the same effect. Furthermore, little is known about the effect of the tumor microenvironment on the differentiation of newly resident tumor macrophages that are engineered to eat cancer cells. Considerable progress over the past decade has been made toward understanding the broad plasticity of macrophages and their responses to microenvironments such as the tumor (Adlerz *et al.*, 2016). Our initial analyses of at least one mechanosensitive nuclear protein in macrophages suggested that microenvironment stiffness could regulate macrophage differentiation.

With an understanding of anti-CD47 therapy and adoptive transfer of macrophages, we started our initial phagocytosis assays by inhibiting only SIRPα on macrophages. Quickly, it became evident that blockade of SIRPα only was insufficient to stimulate engulfment of cancer cells by macrophages. Therefore, we needed an opsonization antibody that had high specificity toward cancer cell lines as safety concerns were already an issue with CD47 inhibition. Chapter 3 focuses on our investigation of possible neoantigen targets and how they arise in cancer cells. A meta-analysis of recently published sequencing data revealed that somatic mutation rate increased with normal tissue stiffness across cancer types. Among various hypotheses that seek to explain this scaling relationship, the one that we considered most promising holds that stiffer tissues have smaller extracellular matrix pores. This can increase DNA damage in invading cancer cells, perhaps leading to genomic variation and neoantigens. We went on to study different methods used to target these neoantigens, focusing on those using immune cells that infiltrate solid tumors. Since healthy cells lack these neoantigens, it seems plausible to target plasma membrane neoantigens with antibodies to drive Fc-dependent

phagocytosis of cancer cells without causing clearance of healthy cells. This is important in the case of treating mouse cancers in mice (chapter 5) rather than human cancers in mice (Chapter 4), as antibodies are often species-specific and, therefore, targeting human antigens in mice have substantially fewer off-target effects.

Chapter 4 contains our study of the biophysically intensive processes of phagocytosis, migration, and differentiation. We simplified *in vivo* studies by using human-derived tumor models in NSG mice (non-obese diabetic/severe combined IL-2Rγ mice (Pearson *et al.*, 2008)) that lacked T-cells, B-cells (and Ab's), as well as NK-cells while maintaining functional monocytes, macrophages, and neutrophils (McIntosh *et al.*, 2015; Quintana *et al.*, 2012). We systemically injected highly phagocytic marrow macrophages that were SIRPα inhibited and had their Fc-Receptors pre-loaded with cancer-targeting Ab's (A'PB MΦ) into mice with established tdTomato A549 tumors. We found that engineering macrophages in this way increased phagocytosis of tdTomato A549 cells in culture (Okazawa *et al.*, 2005; Oldenborg *et al.*, 2000) and, within days of A'PB MΦ injection, tdTomato expressing A549 tumors regressed. During these studies, we found TAMs to be minimally phagocytic, even toward CD47-knockdown tumors. Past studies have opsonized tumors *in situ* with antibody and/or relied on mouse TAMs (Weiskopf *et al.*, 2013; Willingham *et al.*, 2012), but have not injected SIRPα-inhibited cells. Unlike past injections of anti-CD47, blood parameters remained normal with A'PB MΦ treatment. Interestingly, we observed that A'PB MΦ would accumulate in tumors rather than other tissues and seems to be dependent on phagocytic activity. Unfortunately, after 1-2 weeks of tumor residency, donor macrophages quickly differentiated toward non-phagocytic, SIRPα-high TAMs.

Although we found A'PB MΦ alone to be sufficient to shrink solid tumors in immune incompetent mice, we hypothesized that a greater tumor response could be achieved in a fully immune competent model. Previous studies had shown TAMs to be poor activators of acquired immunity (Liu *et al.*, 2015), but the ability of marrow-derived macrophages to initiate an acquired immune response in tumors was unknown. Therefore, in chapter 5 we studied whether marrow-derived macrophages (MDMs) accumulate in syngeneic orthotopic melanoma tumors, engorge on cancer cells, and activate T-cells. Engineered macrophages had sustained tumor shrinkage for 7 days despite T-cell depletion, but tumors eventually regrew. However, 60% of tumors treated in mice with intact T-cells had complete tumor regression. These 'cured' mice were re-challenged with melanoma 100 days after treatment and had significantly delayed tumor growth, whereas untreated mice grew tumors within days of being challenged. This suggested that MDMs can initiate long-term acquired immunity against melanoma tumors.

Chapter 2: Engineering macrophages to eat cancer: from 'Marker of Self' CD47 and phagocytosis to differentiation

This chapter presents work featured in the review article:
Alvey, C.M. and Discher, D.E. (2017) *Journal of Leukocyte Biology*. 102: 1-10.

ABSTRACT

The ability of a macrophage to engulf and break down invading cells and other targets provides a first line of immune defense in nearly all tissues. This defining ability to 'phagos' or devour can subsequently activate the entire immune system against foreign and diseased cells, and progress is now being made on a decades old idea of directing macrophages to phagocytose specific targets such as cancer cells. Engineered T-cells provide precedence with recent clinical successes against liquid tumors, but solid tumors remain a challenge and a handful of clinical trials seek to instead exploit the abundance of tumor associated macrophages (TAMs). Although macrophage differentiation into such phenotypes with deficiencies in phagocytic ability can raise challenges, newly recognized features of cancer cells that might be manipulated to increase the phagocytosis of these cells include at least one membrane protein, CD47, which broadly inhibits phagocytosis and is abundantly expressed on all normal cells. Physical properties of the target also influence phagocytosis and again relate – via cytoskeleton forces – to differentiation pathways in solid tumors. Such pathways extend to mechanosensing by the nuclear lamina, which is known to influence signaling by soluble factors that regulate macrophage SIRPα, the CD47 receptor. Here we highlight some of these past, present, and rapidly emerging efforts to understand and control macrophages for cancer therapy.

2.1. INTRODUCTION

Phagocytosis is an ancient, cytoskeleton-intensive process of cell-level eating that is used by amoeba and that has continually evolved in higher organisms. In humans, it is the defining process of the mononuclear phagocyte system (MPS). The two principal cell types of the MPS are macrophages, which reside in every tissue, and monocytes, which differentiate to macrophages when exiting circulation to enter tissues (Gosselin *et al.*, 2014; Lavin *et al.*, 2014). MPS cells, along with highly phagocytic neutrophils, must – for the health of the organism – selectively devour 'foreign' targets such as microbes rather than phagocytose the human 'self' cells or extracellular matrix that typically surround our phagocytes. Macrophages have a uniquely efficient capacity to phagocytose multiple targets, digest them, and search for more – including some types of diseased cells amongst healthy cells (Fidler & Kleinerman, 1984). However, macrophages fail to perceive and attack tumors as foreign (Condeelis & Pollard, 2006; Lu-emerson *et al.*, 2013).

Macrophages are abundant and motile in solid tumors (Chaturvedi *et al.*, 2014; Condeelis & Pollard, 2006; Lu-emerson *et al.*, 2013) compared to T-cells that minimally infiltrate (Fousek & Ahmed, 2015; Johanna A. Joyce & Fearon, 2015; Salmon *et al.*, 2012). The latter observations might help explain the poor clinical trial outcomes for T-cell therapy of solid tumors (Kakarla & Gottschalk, 2014; Nicol *et al.*, 2011). On the other hand, macrophages are not only 'plastic' in the sense that they exhibit a broad capacity to differentiate in different microenvironments, but the density of the 'tumor associated macrophage' (TAM) phenotype has been linked to promoting tumor growth, inducing angiogenesis, and inhibiting other immune effector cells (Colegio *et al.*, 2014; Fujiwara *et al.*, 2011; Lan *et al.*, 2012; Lu-emerson *et al.*, 2013; Y. Zhang *et al.*, 2013). Clinical

data shows high TAM density is indeed correlated with poor prognosis (Leek *et al.*, 1996). The 'tumor associated macrophage' is perhaps a misnomer in the strict sense of the macrophage as a giant eating cell because these cells seem to have lost most or all of their ability to phagocytose, and their low MHC-II expression likely hinders their activation of the adaptive immune system against tumor neoantigens (Lavin *et al.*, 2014; Lu-emerson *et al.*, 2013; D. Rodriguez *et al.*, 2013). In efforts to address some of the above challenges, engineering of macrophages *ex vivo* for 'adoptive transfer' back into cancer patients had been pursued for many years (Andreesen *et al.*, 1998; Lacerna *et al.*, 1988), but some new insights into macrophage interactions and plasticity might prove useful in re-invigorating such approaches (**Fig. 2.1A**).

Figure 2.1. Anti-cancer macrophages and CD47

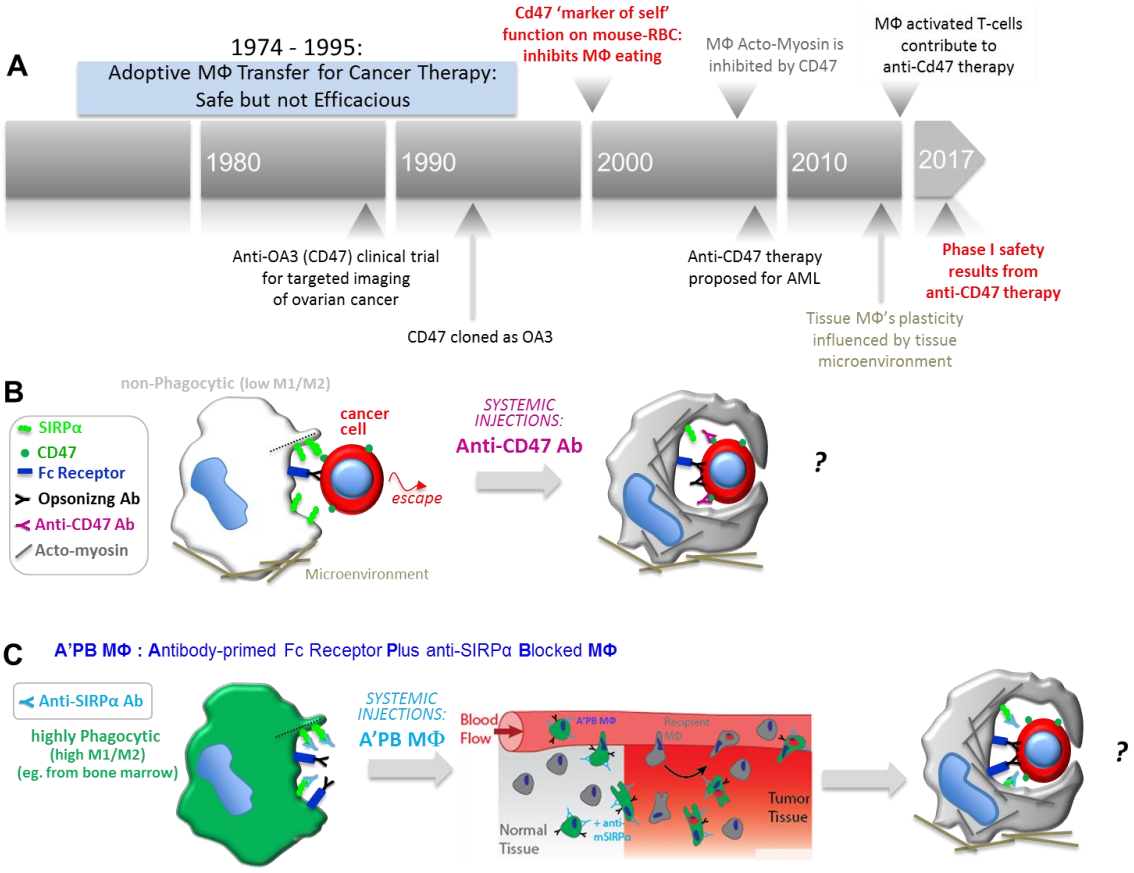

Figure 2.1. Anti-cancer macrophages and CD47. (A) Timeline of adoptive macrophage transfer and CD47 studies converging on anti-CD47 focused macrophage therapies. **(B)** Inhibition of cancer cell engulfment because of recognition of CD47 by a non-phagocytic phenotype despite the presence of a pro-phagocytic antibody. Addition of anti-CD47 blocking antibody and a more phagocytic phenotype can drive engulfment. The Acto-Myosin cytoskeleton has a key role in phagocytosis and linking the microenvironment to influence phenotype. **(C)** Antibody modification (blocking SIRPα and loading Fc receptor with targeting antibody) of marrow macrophages followed by systemic injection could be an effective method for adoptive macrophage cancer therapy. In circulation, A'PB macrophages could in principle migrate into tumors, phagocytose cancer cells, and then either exit the tumor or continue to destroy tumor cells.

2.2. Adopting macrophages as a cell therapy

Adoptive macrophage transfer was first pursued decades ago in some of the earliest cell therapy efforts against cancer. Monocytes isolated from peripheral blood were: (1) cultured in conventional dishes for most preclinical studies and in Teflon bags for clinical trials, and then (2) 'engineered' by differentiation into some form of adherent macrophage with interferon-γ and lipopolysaccharide, before (3) ultimately being injected back into patients. Safety was established with injections of up to 1.5 x 10^9 cells (Andreesen *et al.*, 1998). For comparison, roughly 10^5 white blood cells egress from human marrow every second, and only ~5% are monocytes (with ~10^6 red blood cells), so that the cited injections are equivalent to what would be normally produced over a few days as naïve cells. However, efficacy assessments in these early clinical trials showed little to no benefit of these *in vitro* engineered macrophages (Andreesen *et al.*, 1990; Faradji *et al.*, 1991; Hennemann *et al.*, 1997; Lacerna *et al.*, 1988).

It was understood decades ago that for macrophages to destroy cancer cells they needed to be activated, and numerous soluble and/or surface bound factors could act as molecular cues to stimulate MPS destruction of foreign targets. Immunoglobulin-G (IgG) antibodies are among the most modular (and now designable), as they signal via the macrophage membrane receptor FcγR (for specific isoforms of FcγR and IgG). IgG's produced by B cells perfuse and diffuse throughout the body and bind to a target surface so that when a macrophage contacts the target, the constant fragment (Fc) of the IgG binds the FcγR to signal phosphorylation of immunoreceptor tyrosine-based activating motifs (ITAMs), which then propagates a phosphorylation cascade that regulates adhesion and cytoskeletal remodeling (Cox & Greenberg, 2001). Phosphopaxillin, F-actin, and myosin-

II are just a few among many such proteins that subsequently accumulate within minutes at this dynamic phagocytic synapse (Aderem & Underhill, 1999; Greenberg, Chang, & Silverstein, 1994; Tsai & Discher, 2008). Antibody dependent cell-mediated cytotoxicity (ADCC) and antibody dependent cellular phagocytosis by macrophages have indeed been reported to be crucial to anticancer mechanisms *in vitro* and *in vivo* (Pallasch *et al.*, 2014). Studies often prove this by depletion of TAMs after systemic injection of clodronate particles, but the approach has shortcomings as highlighted below. Nonetheless, these pro-phagocytic signals are also balanced by inhibitory signals. Engagement of FcγRIIB (CD32B) causes activation of immunoreceptor tyrosine-based inhibitory motifs (ITIMs) which promote internalization of pro-phagocytic IgGs preventing activation of ITAMs. Blocking FcγRIIB can prevent internalization of therapeutic antibodies such as rituximab increasing cell surface accessibility of such antibodies by macrophages (Dahal *et al.*, 2015; Roghanian *et al.*, 2015).

Early studies of adoptive macrophage transfer explored *ex vivo* incubation of engineered antibodies that targeted the Fcγ receptors on macrophages and specific antigen on tumor cells (Boyer *et al.*, 1999; Chokri *et al.*, 1992; Ely *et al.*, 1996; Michon *et al.*, 1995). The approach failed to control tumor growth (Andreesen *et al.*, 1998) and might be explained by minimal activation of the macrophage Fcγ receptor, since the downstream response from IgGs varies greatly with engagement, antibody isotypes, and species (Overdijk *et al.*, 2012). Unfortunately, the inability to strongly activate and control phagocytosis dampened interest in adoptive transfer approaches to treat cancer.

2.3. CD47 signals “don’t eat me”

In watching a movie of phagocytosis, it is easy to assume that failure of an otherwise activated macrophage to engulf a target reflects a lack of surface 'opsonization' by molecules such as IgG. However, it is now clear that in addition to 'foreign' signals there are also signals for specific recognition of 'self'. If opsonization is analogous to putting your foot on the gas, then self-signaling is the brake that overrides the phagocytosis process. Indeed, a dominating and passivating interaction occurs between the ubiquitous 'marker of self' CD47 membrane protein on a candidate target cell (or particle) and the macrophage membrane receptor signal-regulatory protein alpha (SIRPα) (Brown & Frazier, 2001; Mawby *et al.*, 1994; Oldenborg *et al.*, 2000). Phagocytosis of cancer cells that are targeted by opsonizing IgG might thus benefit by blockade of CD47, even given the limited phagocytic capacity of TAMs (**Fig. 2.1B**). Alternatively, bone marrow derived macrophages are highly phagocytic when SIRPα has been blocked in *in vitro* studies (Oldenborg *et al.*, 2000). However, it remains untested whether systemic injections of such "Antibody-primed Fc Receptor Plus anti-SIRPα Blocked (A'PB) MΦ" can find their way *in vivo* to a tumor and subsequently phagocytose opsonized cancer cells (**Fig. 2.1C**).

Within a macrophage that is phospho-activated through engagement of a target via an IgG-FcγR interaction, simultaneous engagement of CD47-SIRPα activates the tyrosine phosphatase SHP1, *via* SIRPα's ITIMs, which de-activates the myosin-II contractile cytoskeleton among other structural targets to greatly impede phagocytosis (Rodriguez *et al.*, 2013; Tsai & Discher, 2008). F-actin polymerization is uninhibited and filipodial protrusions tend to push a 'self' recognized target away from being engulfed (Sosale *et al.*, 2015). More such structure-function signaling studies are certainly needed, as

understanding the balance of 'eat me' cues (e.g. IgG-FcγR interaction) and 'don't eat me' signals (CD47-SIRPα) has become an active area of research, especially regarding therapeutic applications. Translation to the clinic is already focused on anti-cancer therapy (Lockhart *et al.*, 2007), and pre-clinical studies demonstrating CD47 utility to reduce macrophage uptake of 'foreign' nanoparticles and lentiviral vectors for drug and gene delivery (Rodriguez *et al.*, 2013; Sosale *et al.*, 2016).

Prior to the cloning and formal naming of 'CD47' in the mid-1990's (Lindberg *et al.*, 1994; Mawby *et al.*, 1994), this ubiquitous membrane protein was already referred to as OA3 antigen due to abundant binding of a monoclonal IgG (OVTL3) to ovarian cancers. Even earlier, bivalent $F(ab')_2$ fragments of this monoclonal antibody against the single, extracellular, immunoglobulin-like domain of CD47/OA3 had already been used for targeted radio-imaging. Despite ubiquitous expression, imaging results were described as showing 80% specificity in 31 patients (Massuger *et al.*, 1990). While any inhibition of 'self' recognition is unlikely to have impacted the growth of the tumors in these studies decades ago (see below), retrospective analyses of the anti-CD47 injection protocols and outcomes can inform current concerns of the safety (or not) of anti-CD47 injections in cancer patients.

Numerous human cancers and patients have since been reported to display CD47 at levels >3-fold higher than expression on healthy tissue (Willingham *et al.*, 2012; Zhang *et al.*, 2015). High levels of CD47 seems to correlate with poor clinical outcomes (Chao *et al.*, 2010; Majeti *et al.*, 2009; Willingham *et al.*, 2012). CD47 and another immune inhibitor, PD-L1, are either strongly turned on or are simply selected for during early cancer development, and both are transcriptionally controlled by MYC as a common

oncogene (Casey *et al.*, 2016; Kaur *et al.*, 2013). Low levels of CD47 on various cancerous and non-cancerous cells are typical of apoptosis and combine with various opsonizing factors to favor clearance by macrophages (Gardai *et al.*, 2005; Gregory & Brown, 2005; Roos & Kaina, 2013). Despite this background knowledge, the processes that occur within the macrophage during phagocytosis continue to require study, particularly because most studies of macrophage involvement in tumor shrinkage have relied on systemic injection of clodronate particles to poison macrophages even though this approach can cause variability in tumor growth (Wang *et al.*, 2013; Yanagita *et al.*, 2017) **(Fig. 2.2A)** and assumes uptake is efficient in its effects on the desired cells (TAMs) but has no broader effect on other cells (eg. other macrophages, cancer cells). Isolation of macrophages from tumors followed by direct assessments of phagocytosis will be more compelling.

Figure 2.2. Tool kit for studying the effect of CD47 inhibition on tumor growth

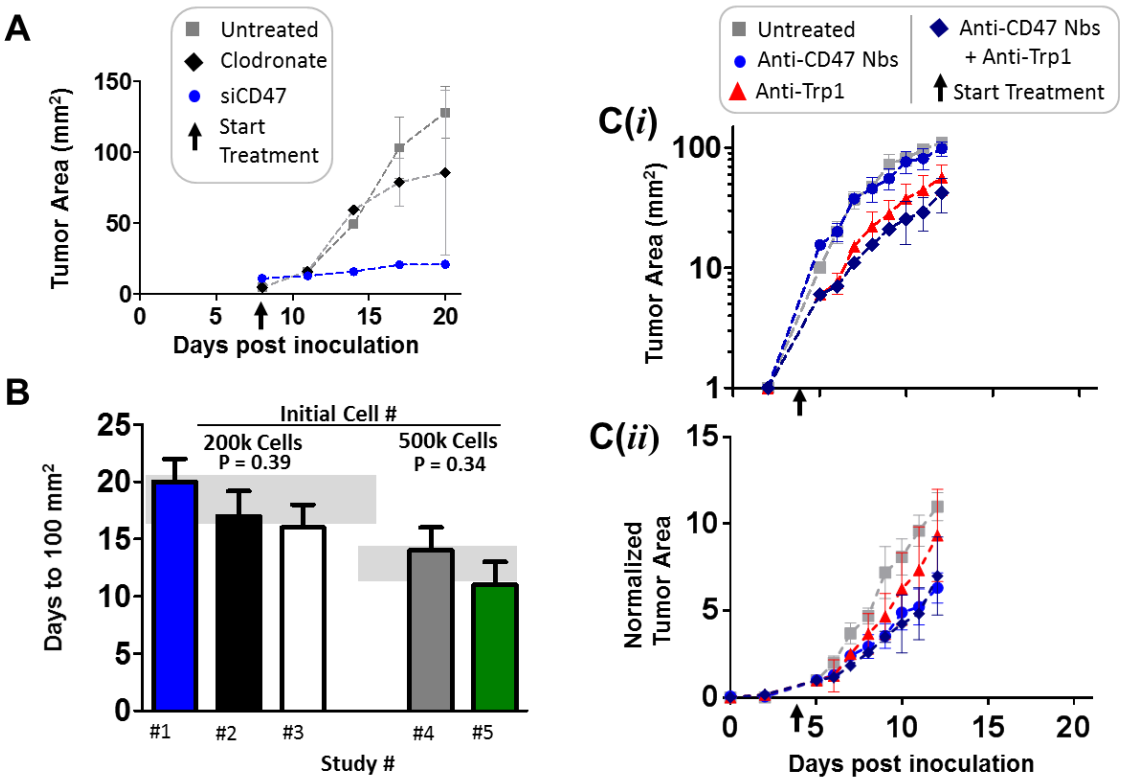

Figure 2.2. Tool kit for studying the effect of CD47 inhibition on tumor growth. (A) Growth curve of syngeneic, orthotopic B16F10 tumors in C57 mice show the effects that si-mCD47 liposomes and clodronate liposomes have on tumor growth. Data adapted from (Wang *et al.*, 2013). **(B)** Analysis of how long untreated orthotopic B16F10 tumors in C57 mice take to reach 100 mm^2 when challenged with either 200k or 500k. Data is adapted from: 1 Alvey and studies 2 (Wang *et al.*, 2013), 3 (Bencherif *et al.*, 2015), 4 (Ali *et al.*, 2009), and 5 (Sockolosky *et al.*, 2016); (*) indicates $p \leq 0.05$. **(C)** Growth curves of orthotopic B16F10 tumors in C57 mice treated with a combination of anti-CD47 nanobodies and an antibody that binds tyrosinase-related protein 1 (Trp1). Data adapted from (Sockolosky *et al.*, 2016). ***(i)*** Log-scale growth highlights differences in tumor sizes between treatment conditions near the start of treatment. ***(ii)*** Normalizing growth data to day 5 gives a different interpretation from the reported conclusions (*i*): anti-Trp1 has only a small effect, but combination with anti-CD47 nanobody can significantly reduce tumor growth.

2.4. Status of anti-CD47 therapy and safety assessments

Clinical trials of CD47 blockade for therapy are rapidly emerging with anti-human-CD47 antibodies (**Table 2.1**). These trials rely on TAMs and perhaps infiltrating monocytes that are partially or fully inhibited from recognizing tumors as self (Chao *et al.*, 2010; Willingham *et al.*, 2012). A few preclinical models with syngeneic tumors have shown complete inhibition of tumor growth when using either anti-mCD47 or siRNA knockdown of *Cd47* with nanoparticles (Wang *et al.*, 2013; Weiskopf *et al.*, 2013). Success against human-derived xenografts has extended to human cancer stem cells in mice (Cioffi *et al.*, 2015). However, most preclinical models show CD47 disruption alone is insufficient (Chao *et al.*, 2010; Sockolosky *et al.*, 2016; Weiskopf *et al.*, 2013). Strongly pro-phagocytic signals (like a foot on the gas pedal) and effective inhibition of CD47 (to eliminate any braking) seem necessary in combination to drive phagocytosis of cancer cells by TAMs (Chao *et al.*, 2010; Sockolosky *et al.*, 2016; Weiskopf *et al.*, 2013) (**Fig. 2.1B**). Anti-CD47 antibodies had been thought sufficient to inhibit CD47 and activate phagocytosis through Fc engagement, but results are mixed at best even when combined with tumor pro-phagocytic signals such as calreticulin and phosphatidylserine (Chao *et al.*, 2010; Feng *et al.*, 2015; Lundqvist *et al.*, 2008; Rettig *et al.*, 1999).

One recent study (Horrigan *et al.*, 2017; Willingham *et al.*, 2012) failed to replicate any efficacy with anti-mCD47 inhibition and questioned the statistical significance of past data (Horrigan *et al.*, 2017; Willingham *et al.*, 2012). An additional concern arose with the syngeneic orthotopic breast tumor model used in both studies in that the tumors were reported to spontaneously regress during the replication studies (Horrigan *et al.*, 2017; Willingham *et al.*, 2012). An alternative syngeneic orthotopic tumor model with well-

documented robustness in terms of reproducibility is the melanoma model B16F10 derived from and engrafted in C57 mice. This model shows consistent tumor growth rates between different labs and over time, which suggests it to be a very predictable and useful model (Bencherif *et al.*, 2015; Wang *et al.*, 2013) (**Fig. 2.2B**). Even with a reliable tumor model, another cause of uncertainty in the field seems to arise from the numerous ways tumor growth data is reported: publications commonly show either tumor volume (often assuming shape or height), tumor cross-sectional area (measured or estimated from shape), or normalized tumor area, but each can yield a different conclusion. In one recent study of B16F10 tumors, the authors reported that injection of an antibody against tyrosinase-related protein 1 (Trp1) was sufficient to significantly reduce tumor growth in mice (Sockolosky *et al.*, 2016). However, anti-Trp1 treated tumors were 2-3-fold smaller than control tumors within 1 day after treatment started (**Fig. 2.2C(i)**). When the data is normalized to that day 5-time point, anti-Trp1 shows no effect, whereas the combination of anti-Trp1 with anti-CD47 nanobody does seem to have inhibited tumor growth when normalized (**Fig. 2.2C(ii)**). Such re-analyzed findings again suggest that shrinkage of tumors with anti-CD47 requires at least a combination with another tumor opsonizing antibody, such as rituximab or trastuzumab in other studies (Chao *et al.*, 2010; Weiskopf *et al.*, 2013).

Safety of anti-CD47 antibody injections remains a concern. Injections of anti-mCD47 in mice and anti-hCD47 monkeys lead to a 30% decrease in RBC count within days following a single injection (Tseng *et al.*, 2013; Weiskopf *et al.*, 2013). Antibodies and other serum proteins bind both specifically and non-specifically to red blood cells (RBCs) (Franco *et al.*, 2013; Turrini *et al.*, 1991), to viruses (Wilflingseder *et al.*, 2007),

and even particles coated with PEG (polyethylene glycol) (Discher *et al.* 2014), and so 'eat me' signals are always present. Perhaps related, one strain of CD47 knockout mouse survives for only 6 months and has detectable IgG against mouse RBCs as well as anemia and organ failure (Oldenborg *et al.*, 2002). Inhibiting the receptor for CD47 on macrophages, SIRPα, also enhances phagocytosis *in vitro* (Ho *et al.*, 2015; Oldenborg *et al.*, 2000) and *in vivo* (Rodriguez *et al.*, 2013), and the latter studies show that systemic injection of anti-SIRPα antibodies leads to rapid clearance of circulating components (Rodriguez *et al.*, 2013). Despite the caution required from this data, a growing number of clinical trials are using anti-CD47 antibodies in patients with diverse liquid and solid tumors that range from leukemia to colorectal cancer (Archambeaud *et al.*, 2016; Burgess *et al.*, 2015; Chao *et al.*, 2016; Kang, *et al.*, 2011; Sievers *et al.*, 2016; Takimoto *et al.*, 2014) (**Table 2.1**).

Blood analyses will likely provide the first evidence of safety in human trials with therapeutically relevant doses of anti-CD47 injected systemically. Based on animal studies, a short term mild anemia is expected, and anemia might even be already evident in a retrospective analysis of patient data from the early radio-imaging trial that used anti-CD47 targeting of ovarian cancer (Massuger *et al.*, 1990). Leukocytes as well as platelets in human circulation are all likely to be affected by systemic anti-CD47 because CD47 is displayed on all cells and is known for most cell types to prevent their phagocytosis. The abundance of RBCs makes them easiest to quantify, and the youngest blood cells are routinely quantified only for RBCs (i.e. reticulocytes) in providing the clearest measure of an ongoing perturbation. One can anticipate that RBC-clearing macrophages in the human spleen will initially phagocytose older RBCs that are the most IgG opsonized and

the stiffest (Sosale *et al.*, 2015), but a new steady state for RBC lifespan is difficult to predict given that CD47 nulls exist only in mice and not in humans.

In the normal steady state, every second ~1-million reticulocytes emerge from marrow to mature in about 1 day to discocyte-RBCs which replace old, opsonized, stiff RBCs that are cleared at ~100 days (reticulocytes are thus ~1% of RBCs). Within days of injecting anti-CD47 systemically, the oldest RBCs should decrease in age to about 70 days – based on noted mouse and primate studies (~30% loss in RBCs) (Tseng *et al.*, 2013; Weiskopf *et al.*, 2013). This will likely saturate engorgement of splenic macrophages (splenomegaly when chronic) which may limit clearance of even younger, CD47-blocked RBCs. Enhanced production of reticulocytes (perhaps increasing to ~10%) will compensate for the rapid loss of RBCs. This degree of compensation is also observed in humans who, secondarily to other genetic defects, lack ~90% of CD47 on their RBCs (Bruce *et al.*, 2002; Dahl *et al.*, 2004). Within weeks of continued anti-CD47 injections, the anemia is likely to become better compensated and reticulocyte production should gradually decrease with the oldest RBC age remaining low at ~90+ days. An over-abundance of CD47 on RBCs allows for a half-max effectiveness at just ~10% of normal levels (i.e. 10% of ~250 molecules per sq. micron on RBC (Rodriguez *et al.*, 2013)) that can still signal 'self' to macrophages. It will be important to therefore determine whether systemic anti-CD47 binds and blocks up to ~90% of CD47 and thereby mimics tolerable human deficiencies of CD47 or greatly exceeds such states. These projected estimations illustrate the careful consideration of CD47 quantities on various cells; determining how much anti-CD47 binds and blocks can thus make sense of past studies and new clinical results with humanized anti-CD47 IgG isotypes.

Table 2.1. CD47-SIRPα clinical trial data

Compound	Company	Target	Treated Disease	Start Date	Estimated Completion Date	Phase
Hu5F9-G4	Forty Seven, Inc.	CD47	Colorectal neoplasms/solid tumors	November 1, 2016	March 1, 2023	Phase I/Phase II (Cetuximab)
Hu5F9-G4	Forty Seven, Inc.	CD47	Non-hodgkin/large B-cell lymphoma	November 1, 2016	January 1, 2023	Phase I/Phase II (Rituximab)
TTI-621	Trillium Therapeutic Inc.	CD47	Melanoma/breast carcinoma/solid tumors	September 1, 2016	December 1, 2019	Phase I
CC-90002	Celgene	CD47	Acute myeloid leukemia	July 27, 2016	July 1, 2019	Phase I
SIRPα antibody	Nantes University Hospital	SIRPα	Hepatocellular carcinoma	June 16, 2016	May 1, 2019	Investigation
Hu5F9-G4	Forty Seven, Inc.	CD47	Acute myeloid leukemia	January 27, 2016	January 1, 2018	Phase I
TTI-621	Trillium Therapeutic Inc.	CD47	Hematologic malignancies	January 19, 2016	June 1, 2019	Phase I
CC-90002	Celgene	CD47	Hematologic cancers/solid tumors	February 13, 2015	January 1, 2018	Phase I
Hu5F9-G4	Forty Seven, Inc.	CD47	Solid tumors	August 12, 2014	August 1, 2017	Phase I
None	Medical University of South Carolina	CD47	Multiple myeloma	July 13, 2011	July 1, 2014	Prognostic Potential for Chemotherapy

Table 2.1. CD47-SIRPα clinical trial data. Chronological order of anti-CD47 antibody clinical trials on a variety of human cancers. Most of these trials were started in 2016 and include Phase II studies in combination with an additional opsonizing antibody.

2.5. Macrophage: a bridge to acquired immunity

Although macrophage engulfment of cancer cells can contribute to tumor reduction, phagocytic cells can also present neoantigens to T-cells. Early hints of this have included (i) the noted presence of IgG against RBCs in some strains of *Cd47* knockout mice, and also (ii) differences in the effects of mCD47 blockade between syngeneic and immune deficient tumor models (Oldenborg *et al.*, 2002; Sockolosky *et al.*, 2016; Wang *et al.*, 2013; Zhang *et al.*, 2015). Absent any targeting of mCD47, vaccination studies have certainly documented T-cell activation by macrophages and phagocytic dendritic cells in cancer therapies: for example, implanted scaffolds that contain tumor lysates and cytokines lead to acquired immunity – probably after being phagocytosed – in syngeneic models (Bencherif *et al.*, 2015; Ly *et al.*, 2013). With mCD47 blockade, T-cells are recruited to tumors by phagocytic macrophages even though tumor clearance seems dominated by macrophages (Sockolosky *et al.*, 2016; Tseng *et al.*, 2013). Surprisingly, even though PDL1 on cancer cells is primarily considered to inhibit T-cell interactions and thereby enhance T-cell responses, anti-PDL1 IgG can also engage macrophage Fc receptor and indeed has a major role in driving phagocytosis (Sockolosky *et al.*, 2016; Tseng *et al.*, 2013). With a standard melanoma model (in which initial treatments were begun before tumors became palpable), blockade of PDL1 also required blockade of mCD47 for long term mouse survival and re-challenge with cancer cells (Sockolosky *et al.*, 2016; Tseng *et al.*, 2013).

Other syngeneic tumor models using mCD47 blockade have relied on endogenous opsonization (eg. calreticulin (Chao *et al.*, 2010; Lundqvist *et al.*, 2008; Rettig *et al.*, 1999)) and showed shrinkage in days, but injection of anti-CD8 – which should deplete T-cells –

removes any therapeutic effect (Liu *et al.*, 2015). This suggested to the authors that the primary effector cell is the T-cell. Alternatively, T-cells displaying an intact anti-CD8 IgG (typically IgG1 that strongly engages Fc receptor) could be the most opsonized cell in or near a tumor (assuming T-cell infiltration), and thus mCD47-blocked TAMs phagocytosing such T-cells would distract from phagocytosis of weakly opsonized tumor cells. Understanding the dominating imbalance is sometimes unclear, but such findings nonetheless question whether TAMs are always effective phagocytic cells and antigen presenters. TAMs certainly promote tumor growth and are weakly phagocytic, at least when compared to peritoneal macrophages (Fujiwara *et al.*, 2011; Lan *et al.*, 2012; Rodriguez *et al.*, 2013; Zhang *et al.*, 2013). TAMs also have low MHC-II, which is required for activation of T-cells (Franklin *et al.*, 2014; Gosselin *et al.*, 2014; Lavin *et al.*, 2014). Regardless of the extent to which T-cells contribute, the ability of macrophages to activate T-cells should be considered when evaluating efficacy as well as safety. The ubiquitous and abundant expression of CD47 on all cells has already given cause for concern over anti-CD47 therapy, first in terms of the massive amount of antibody that needs to be injected, but more important is the possibility of a chronic autoimmune response against healthy cells, such as the rapidly cleared RBCs.

Concerns over TAMs could perhaps be addressed by adoptive macrophage therapy in combination with CD47-SIRPα blockade (**Fig 2.1C**). Macrophages and dendritic cells are isolated and/or differentiated as done in early adoptive transfer studies, but they are first engineered with antibodies and/or SIRPα knockdown or CRISPR knockout (Liu *et al.*, 2016; Pan *et al.*, 2013). When SIRPα depletion is combined with transfection of macrophages with presentable cancer antigens, implantation of both the macrophages and

melanoma cells are found to prevent tumor growth (Liu *et al.*, 2016). Safety becomes a major concern, however, because SIRPα knockdown in macrophages, followed by systemic injection, enhances growth of liver cancers (Pan *et al.*, 2013). SIRPα activates the Tyr-phosphatase SHP1, which has a multitude of targets and is therefore likely involved in multiple signaling pathways that affect phenotype (Tsai & Discher, 2008).

2.6. Macrophage plasticity and mechanosensing

Phenotypes of macrophages have classically been divided into two or three states: a pro-inflammatory state (M1), an immune inhibitory, angiogenetic state (M2) (Jablonski *et al.*, 2015; Mantovani *et al.*,1992; Mantovani *et al.*, 2002; Murdoch *et al.*, 2008; Ramachandra *et al.*, 1999), and a more passive M0 state. Macrophages are instead far more diverse and plastic: macrophages from different tissues indeed exhibit distinct expression profiles (Lavin *et al.*, 2014). Studies of macrophage diversity use a variety of surface markers that should be factored into the interpretation of any study in human or mouse (Bencherif *et al.*, 2015; Casey *et al.*, 2016; Colegio *et al.*, 2014; Dorward *et al.*, 2013; Jablonski *et al.*, 2015; Lavin *et al.*, 2014; Majeti *et al.*, 2009; Hanna *et al.*, 2015; Sockolosky *et al.*, 2016; Swamydas *et al.*, 2015) (**Table 2.2**). In mice, the most common macrophage antigen is F4/80, and the CD11b-positive subset is only sometimes used, which might explain some differences in phenotype. Importantly, macrophages taken from a donor tissue and transplanted into a different tissue partially convert over days or weeks to be increasingly like macrophages in the new host tissue (Lavin *et al.*, 2014). Macrophage phenotype is thus plastic and controlled by the local microenvironment, with potential effects of both biochemical and biophysical cues. Any adoptive macrophage

approach used to treat solid tumors will therefore contend with their differentiation to TAMs. Broadly understanding and controlling such differentiation is thus key to macrophage-based therapies.

Differentiation of cultured macrophages into the classic M1 phenotype was done biochemically in early trials of adoptive macrophage therapy prior to transfer into the host (Andreesen *et al.*, 1998; Murdoch *et al.*, 2008). Plastic culture dishes are rigid and are now known to affect differentiation, with stem cell phenotypes in culture affected by the softness of the underlying matrix in a mechanosensing process that depends on Myosin-II contractions of the substrate (Engler *et al.*, 2006) (**Fig. 2.1B**). Macrophages plated on soft gels exhibit a high M1/M2 ratio whereas stiff gels lead to a low M1/M2 ratio (Adlerz *et al.*, 2016). Stiffening of tissues such as breast and liver is often associated with cancer (Boyd *et al.*, 2007; Levental *et al.*, 2009; Singh *et al.*, 2013), and might even contribute to genomic heterogeneity of cancer (Irianto *et al.*, 2017), which complicates therapies with a single molecular target. For macrophages, pre-malignant stiffening of tissue could favor conversion to a non-phagocytic phenotype with a reduced capacity to clear damaged cells, which again favors cancer.

Mechanistically, transcriptional control is provided by the nuclear envelope protein, lamin-A, which regulates the nuclear localization of Retinoic Acid Receptor (RAR) transcription factors; the latter is interesting because epigenetic analyses have implicated RA in microenvironment regulation of macrophage phenotype (Lavin *et al.*, 2014). Different cell types exhibit different expression changes in response to tissue stiffness, but at least one common factor – *lamin-A* – appears mechanosensitive in most (perhaps all) cell types in tissues (Swift *et al.*, 2013). Stiff tissues tend to be under high

mechanical stress, and that stress is transmitted from the cell surface through the actin-myosin cytoskeleton and to the nuclear envelope, with *lamin-A* adjusting its level to sustain the stress (Buxboim *et al.*, 2014) and ultimately protect chromatin from damage (Irianto *et al.*, 2017). Average levels of *lamin-A* protein and transcript increase systematically from soft marrow and soft brain to stiffer muscle and rigid bone whereas the levels of *lamin-B* isoforms remain nearly constant. Macrophages can of course be isolated from any tissue or disease site and provide an *in vivo* test of the broader nuclear mechanosensing hypothesis. Meta-analysis of RNA-seq results for monocytes or macrophages isolated from different tissues show *lamin-A* increasing with tissue stiffness and *lamin-B* remaining nearly constant (**Fig. 2.3A**).

Solid tumors are typically high in collagen, which generally determines tissue stiffness and has already been shown for numerous human cancer types xenografted into mice (Swift *et al.*, 2013). TAMs that are isolated from such tumors using standard markers (F4/80, CD11b) have recently been subject to RNA-seq analysis, which shows that the ratio of *lamin-A* reads to *lamin-B* reads is similar in TAMs to the same ratio in stiff, normal tissues (**Fig. 2.3B**). Such results are thus consistent with mechanosensing of matrix microenvironments by macrophages, and such physical effects on the expression of other genes requires careful study. SIRPα is especially interesting because it was recently shown to be strongly regulated by RA (Zhu *et al.*, 2013), which is mechanosensitive in its downstream effects according to the studies above. If the sensing of microenvironment and the affected gene circuits do drive an increase in SIRPα on TAMs within stiff solid tumors, then TAMs could recognize 'self' cancer cells more readily and thus be passivated. Knockdown of SIRPα would seem logical to counter such pro-tumorigenic effects, but

systemic injections of such engineered macrophages are found to enhance the growth of liver tumors in the absence of added tumor opsonization (Pan *et al.*, 2013).

Table 2.2. Commonly used markers to identify mouse phagocytes

Notes: Lavin et al's study of macrophages in multiple tissues used the indicated markers and sometimes supplemented with additional markers.

		Surface Markers									
Cell Type	**Tissue**	**F4/80**	**CD11b**	**CD11c**	**CD45**	**CD86**	**Ly6G**	**CD45**	**MHC II**	**CCR7**	**CD206**	**Reference**
Phagocyte	Tumor	+										Majeti et al. 2009
Macrophage	Tumor	+										Casey et al. 2016
Macrophage	Pan tissue	+	+									Lavin et al 2014
Macrophage	Cultured	+										Sockolosky et al. 2016
Dendritic	Cryogel implant			+		+						Bencherif et al. 2015
Monocyte	Blood, lung Tumor		+	+	+							Hann et al. 2015
Neutrophil	Bone marrow		+				+					Dorward et al. 2013
Neutrophil	Bone marrow		+				+	+				Swamydas et al. 2015
MO	Cultured	-	+									Jablonski et al. 2015
M1	Cultured	+							+	+	-	Jablonski et al. 2015
M2	Tumor	+							-		+	Colegio et al. 2014

Table 2.2. Commonly used markers to identify mouse phagocytes. Frequently used markers to identify phagocytic cells (macrophages, neutrophils, monocytes) and different macrophage polarizations organized by publication.

Figure 2.3. Stiff matrix regulation of Lamin-A

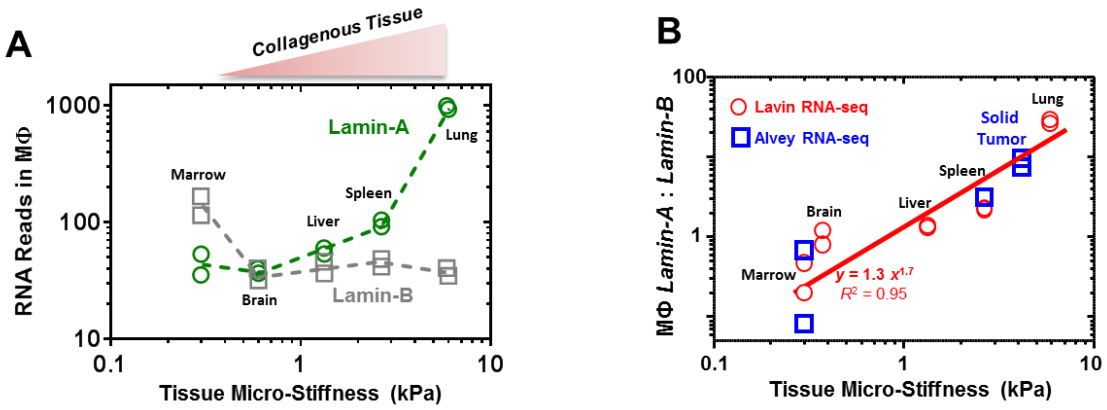

Figure 2.3. Stiff matrix regulation of Lamin-A. (A) RNA-seq reads per Million for *lamin-A* and *lamin-B* in tissue macrophages from (Lavin *et al.*, 2014) plotted as a function of tissue stiffness measurements in (Swift *et al.*, 2013). (**B**) Ratio of RNA reads for *lamin-A : lamin-B* in macrophages including tumor associated macrophages isolated from human tumor xenografts per (Lavin *et al.*, 2014; Swift *et al.*, 2013). Subcutaneous A549 tumors were engrafted in NSG mice and allowed to grow to 80 mm^2 before tumor stiffness was measured and macrophages were profiled.

2.7. Target cell rigidity and shape can override 'self' signaling

Macrophages not only respond to physical cues such as the stiffness of their microenvironments, but also to the targets that they engulf. With spherical microparticles made of hydrogels and opsonized by IgG, engulfment is proportional to stiffness, which was also shown to drive focal adhesion protein assembly at the phagocytic synapse (Beningo & Wang, 2002). Stiffness changes occur with cancer cells and with chemotherapy (Cross *et al.*, 2007; Lam *et al.*, 2009); soft cancer cells might thus escape anticancer efforts aimed at inhibiting CD47-SIRPα interactions (Weiskopf *et al.*, 2013). To test the relevance of cell stiffness and any modulation by CD47 signaling of 'self,' human RBCs were controllably stiffened with a dialdehyde crosslinker and both IgG opsonization and CD47 blockade were separately controlled (Sosale *et al.*, 2015). Phagocytosis of rigidified, discocyte-shaped human RBCs exceeded that of flexible RBCs and proved almost independent of CD47 (**Fig. 2.4A-C**). Myosin-II contractile forces are again key in responding to target rigidity.

Rigid, spherical CD47-beads signal self and thereby impede engulfment both *in vitro* and *in vivo* (Rodriguez *et al.*, 2013), and sphered RBCs also recovered some 'self' signaling probably because the discocyte's rigid concavities could not contact and signal 'self' (Sosale *et al.*, 2015). Target shape is therefore an additional factor in phagocytosis. Indeed, polystyrene microbeads melted and distorted into diverse shapes, for example, are engulfed by macrophages more readily as spheres than as non-spheres when IgG opsonized (Champion & Mitragotri, 2006). Such findings seem relevant to the diverse shapes of bacteria and fungi, which invariably have rigid cell walls. With cancer cells that are soft but CD47-blocked and IgG-opsonized for targeted engulfment by macrophages,

phagocytosis could distort and elongate the cells – as seen for RBCs (Sosale *et al.*, 2015), and this would also tend to weakly oppose successful phagocytosis. Understanding the details of the various physical and chemical cues to macrophages therefore remains an important endeavor.

Figure 2.4. Target physical properties and molecular interactions at the cell surface determine the efficiency of human RBC engulfment by human macrophages

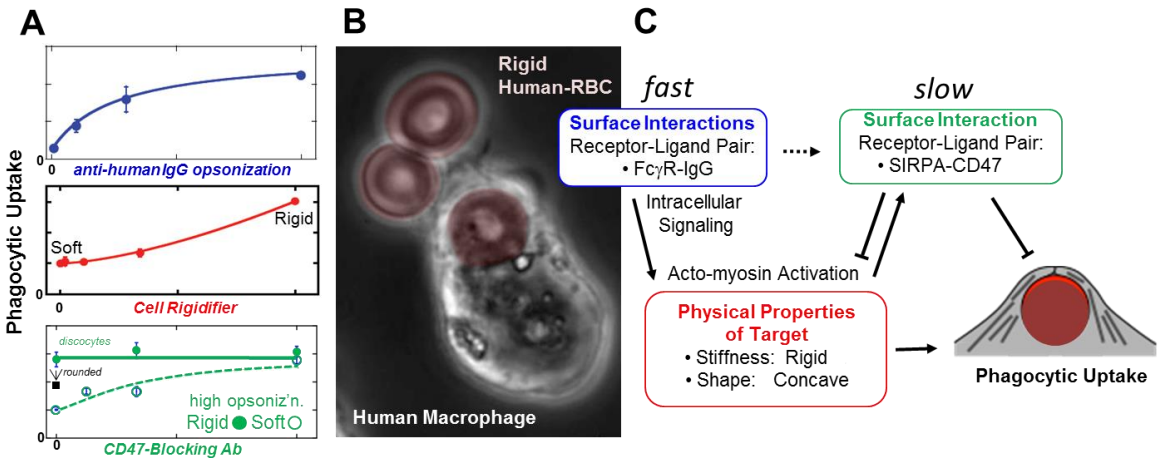

Figure 2.4. Target physical properties and molecular interactions at the cell surface determine the efficiency of human RBC engulfment by human macrophages (adapted from (Sosale *et al.*, 2015))**. (A)** Phagocytosis increases with IgG opsonization and with crosslinker-based rigidification of hRBCs. Phagocytosis of rigid, opsonized RBCs is independent of hCD47 inhibition in contrast to 'Soft' native RBCs whose uptake is enhanced by a hCD47-blocking antibody. A 'sphering' treatment that gives a rounded and rigid hRBC shows reduced uptake relative to discocytes. **(B)** Time-lapse images of rigidified hRBC discocytes shows rapid engulfment and lack of deformation by the macrophage. **(C)** Surface interactions combine kinetically with physical properties of a candidate target in the calculus that determines phagocytic uptake.

2.8. CONCLUDING REMARKS

Over the past four to five decades, macrophages have been found safe albeit ineffective in anti-cancer therapy, but the general approach is perhaps re-emerging based on the discovery of 'marker of self' CD47 signaling to macrophages. This signaling ultimately turns off cytoskeletal myosin-II, which otherwise makes the very active process of engulfing a foreign cell or particle efficient, and so inhibiting this signaling at various upstream or downstream points in the CD47-SIRPα pathway can likewise make engulfment of 'self' cells more efficient. Considerable progress over the past decade has separately been made toward understanding the broad plasticity of macrophages and their responses to microenvironments. Initial analyses of at least one mechanosensitive nuclear protein suggests that such responsiveness includes the stiffness of the microenvironment. Phagocytosis is also favored by the stiffness of a cell or particle, and myosin-II has again been shown to be key. Myosin-II thus has a vital role in multiple, cytoskeletal-intensive activities of macrophages.

Complementary to these basic insights into pathways is a current focus on blockade of CD47-SIRPα to engineer macrophages *in situ* for therapy against cancer. The various clinical trials are likely to encounter some challenges in safety and efficacy, but injection of anti-hCD47 in cancer patients was conducted for decades for imaging purposes. Regardless of success in macrophage engineering *in situ* or *ex vivo* for specific applications, the ability of these fascinating and ubiquitous cells to migrate, engulf, digest, and perhaps activate the broader immune system against foreign and diseased cells merits the renewed interest in understanding their basic functions.

Chapter 3: Genome variation across cancers scales with tissue stiffness – implications for immune cell infiltration

This chapter presents work featured in the review article:
Pfeifer, C.R., Alvey, C.M, Irianto, J., and Discher, D.E. (2017) *Current Opinion in Systems Biology*. 2:102-113.

Pfeifer, C.R. -meta analysis of somatic mutations in published exome sequencing (Figure. 3.1 and 3.2)

ABSTRACT

Many different types of soft and solid tumors have now been sequenced, and meta-analyses suggest that genomic variation across tumors scales with the stiffness of the tumors' tissues of origin. The opinion expressed here is based on a review of current genomics data, and it considers multiple 'mechanogenomics' mechanisms to potentially explain this scaling of mutation rate with tissue stiffness. Since stiff solid tissues have higher density of fibrous collagen matrix, which should decrease tissue porosity, invasion of cancer cells into stiff tissues could squeeze the nucleus sufficiently to enhance DNA damage. Diversification of a cancer genome after constricted migration is now clear. Understanding genome changes that give rise to neoantigens is important to selection as well as to the development of immunotherapies, and we discuss engineered monocytes/macrophages as particularly relevant to understanding infiltration into solid tumors.

3.1. INTRODUCTION

Tumors are often palpably stiffer than nearby normal tissue (Levental *et al.*, 2010), with stiffness of breast and liver, among other organs, correlating with cancer risk (Boyd *et al.*, 2007; Singh *et al.*, 2014). Tissue stiffness likely contributes in normal cells to motility (Pelham & Wang, 1997) and differentiation (Engler *et al.*, 2006), and in cancer cells to invasion (Przybyla, Muncie, & Weaver, 2016) and various epigenetic mechanisms (Spencer, Xu, & Bissell, 2007), including stiffness-dependent nuclear localization of oncogenic factors (e.g. YAP) (Dupont *et al.*, 2011). It is unclear, however, if a physical attribute of the microenvironment such as stiffness could contribute—in a 'mechanogenomics' type of process—to any of the many genetic changes that typically occur in cancer.

Meta-analyses of recently published cancer mutation data begin to suggest that—beyond some initial driver mutation(s)—the large genomic variation across diverse cancers scales with tissue stiffness. Stiffness-dependent cell biological mechanisms for genome variation are needed to substantiate any such correlation, and some molecular mechanisms are now emerging. One possible mechanism is based on the fact that stiffer tissues, including tumors, are enriched in collagen (Swift *et al.*, 2013), and many studies of collagen gels show that denser collagen has smaller matrix pores (Yang, Leone, & Kaufman, 2009). Thus, as cancer cells invasively migrate into stiff, small-pore surroundings, the nucleus is damaged, which might ultimately contribute to genomic diversity.

Invasion is a defining task of a cancer cell; the equal but opposite challenge of an immune cell—therapeutic or otherwise—is to confront stiffness barriers and infiltrate a

wound or disease site to attack ‘non-self’. In the cancer context, genome variation can produce novel protein sequences that might be perceived by the immune system as ‘neoantigens’. Such sequences are by definition absent from normal cells, and so can be used to identify and eliminate cancerous cells if the neoantigen signals are sufficiently potent, accessible, and foreign to overwhelm ‘self’ recognition (Schumacher & Schreiber, 2015). A moonshot-scale effort now seeks to employ neoantigens in various immunotherapy approaches. Some therapies use engineered T-cells to target neoantigens on the cancer cell membrane (Ramos, Savoldo, & Dotti, 2015), while other therapies exploit the major histocompatibility complex (MHC)—class I and class II—to target nuclear and cytoplasmic neoantigens (Hodi *et al.*, 2010; Liu *et al.*, 2016; Ly *et al.*, 2013). Monocytes and macrophages are the focus here and are particularly interesting for targeting to neoantigens because these phagocytic cells exhibit a robust ability to infiltrate solid tissues, including tumors. The microenvironment-dependent plasticity of such cells, which is now being mapped by modern systems biology methods, could also be triggered, in part, by the stiffness or solidity of the tissue.

3.2. Genomic variation scales with tissue stiffness

Advances in genome sequencing have enabled cataloguing of the genomic variations that occur in cancers of many different types (Martin *et al.*, 2015; Matsushita *et al.*, 2016; Schumacher & Schreiber, 2015), and although oxidation artifacts can complicate such methods (Costello *et al.*, 2013), somatic mutation rates are being collected in databases such as The Cancer Genome Atlas (TCGA) run by the National Cancer Institute (NCI). For the healthy tissues of origin of 36 types of cancer, tissue

microelasticity data were culled from numerous recent papers (Alexandrov *et al.*, 2013; Chen *et al.*, 2014; Cross *et al.* 2011; Fuhrmann *et al.*, 2011; Guz *et al.*, 2014; Hoyt *et al.*, 2008; Kawano *et al.*, 2015; Lawrence *et al.*, 2013; Lekka, Gil, *et al.*, 2012; Lekka, Pogoda, *et al.*, 2012; Lim *et al.*, 2009; Lopez *et al.* 2011; Martincorena *et al.*, 2015; Martincorena & Campbell, 2015; Mathur *et al.*, 2001; Petrie *et al.*, 2012; Prabhune *et al.*, 2012; Schumacher & Schreiber, 2015; Shain *et al.*, 2015; Shin *et al.*, 2014; Xu *et al.*, 2012) that used a variety of physical methods, including atomic force microscopy (AFM), micro-indentation probes, micropipette aspiration, and imaging-based elastography (**Table 3.1**). Whereas AFM pushes on cells and tissues at the ~100-nanometer to multi-micron length scales in order to provide a measure of a microenvironment's stiffness, the larger length scale imaging-based elastography methods that perturb and monitor by magnetic resonance imaging, for example, typically probe on a millimeter length scale that encompasses many cells and the matrix between them; in principle, all of these types of measurements should be made on fresh tissue, since the former add up to the latter. However, measurements on cultured cells are likely to have little relevance to the tumor, because culture conditions such as gel stiffness influence cell mechanics (Pelham & Wang, 1997). Importantly, based on current tissue measurements, meta-analyses of genomics indicate that cancers arising in stiff tissues, such as lung and skin, exhibit 30-fold higher somatic mutation rates (as median per sequenced megabase) than cancers arising in soft tissues, such as marrow and brain (**Fig. 3.1A**). Importantly, the stiffness of a typical brain tumor or marrow tumor never increases to that of a typical bone tumor microenvironment even though tumors often stiffen — or, less frequently, soften — in tumorigenesis (Levental *et al.*, 2010). The hierarchy of normal tissue stiffness is therefore likely to

prevail in cancer: that is, brain is softer than liver, which is softer then bone, etc. — regardless of cancer or not.

Childhood muscle and bone cancers have only slightly elevated somatic mutation rates as compared to childhood marrow and brain cancers, but they have >10-fold more chromosome copy number changes and structural variants (Chen *et al.*, 2014) (**Fig. 3.1B**). This disparity suggests that large-scale, chromosome-level amplifications and deletions — more so than somatic mutations — are signatures of some mutational processes that associate with tissue stiffness. In adult melanoma, fibrotic skin tends to be stiffer and exhibit more chromosome copy number changes than softer, less fibrotic skin (Diridollou *et al.*, 2001; Shain *et al.*, 2015) (**Fig. 3.1C-*i***). Moreover, these copy number changes increase even faster with stiffness than do somatic mutation rates, and all mutations are most abundant in invasive melanoma (Shain *et al.*, 2015) (**Fig. 3.1C-*ii***). The relationship between chromosome-level mutations and stiffness thus holds even within a given tissue type, suggesting—in our opinion—a correlation between mutations and stiffness that cannot be entirely explained away by exposure to carcinogens.

Table 3.1. Cancer types and the microelasticities of the healthy tissues in which they arise

Cancer type		Normal tissue stiffness (kPa)
Pilocytic astrocytoma		0.4 [9]
Acute myeloid leukemia (AML)		0.3
Acute lymphoblastic leukemia (ALL)		0.3
Chronic lymphocytic leukemia (CLL)		0.3
Medulloblastoma (MB)		0.4
Carcinoid		0.4
Neuroblastoma		0.4
Thyroid		2.2
Glioma low grade		0.4
Glioblastoma		0.4
Breast		0.4 - 1. 7]
Lymphoma B cell		0.3 [2
Multiple myeloma		0.3
Kidney chromophobe		2.6
Prostate		3.0 - 3.8 29]
Ovary		2.5
Kidney papillary cell		2.6
Kidney clear cell		2.6
Pancreas		2.7
Liver		1.3
Endometrium		1.3
Head and neck		
Uterus		1.3 [28]
Cervix		1.6
Colorectum		0.9
Esophagus		4.7
Lung small cell		5.9
Stomach		1.3
Bladder		3.2
Lung adenocarcinoma		5.9
Lung squamous		5.9
Melanoma		3.8 - 6.4 7]
Squamous cell carcinoma		3.8 - 6.4
Basal cell carcinoma		3.8 - 6.4
Childhood cancers	ALL	0.3 [2
	MB	0.4
	Rhabdomyosarcoma	11.9 - 25 8]
	Osteosarcoma	34.3 [9

Figure 3.1. Genomic variation increases versus tissue stiffness across cancers and with melanoma progression

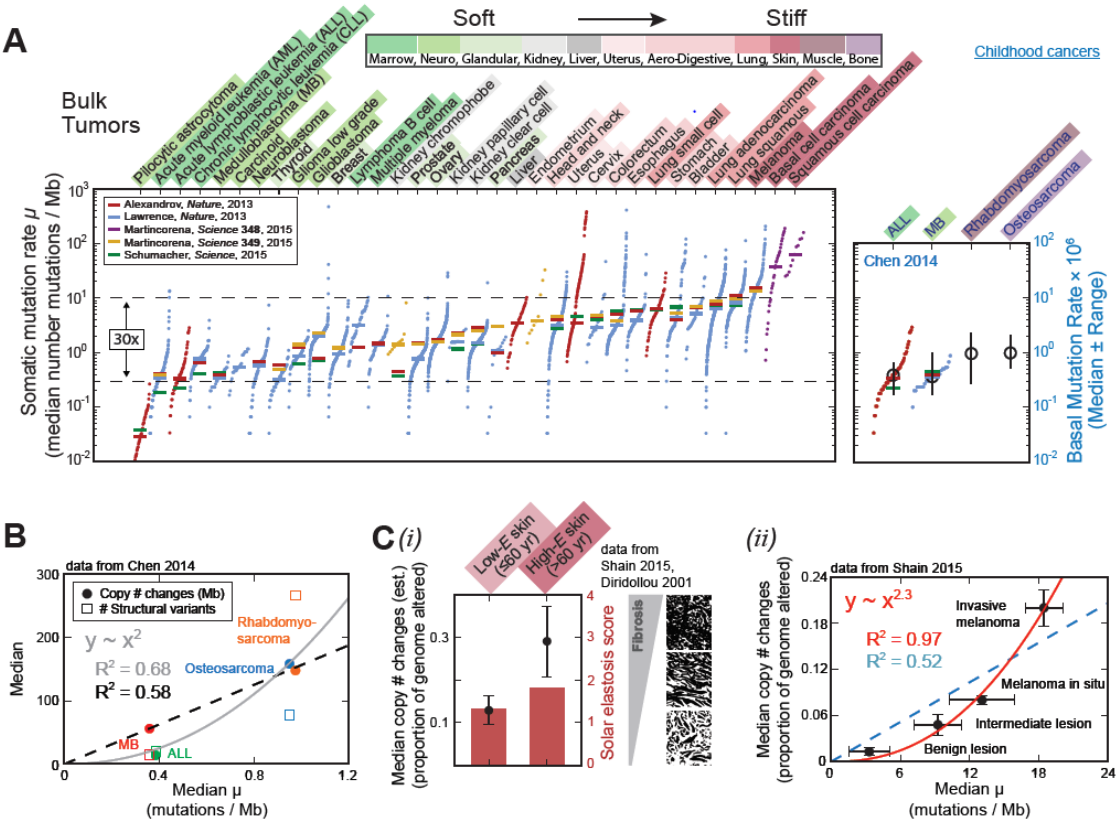

Figure 3.1. Genomic variation increases versus tissue stiffness across cancers and with melanoma progression. (A) Across different cancer types, somatic mutation rate—the median number of somatic substitutions and small insertions/deletions per megabase—increases with normal tissue stiffness. The same trend persists, albeit more weakly, among childhood cancers. The stiffness scale varies >10-fold from softer tissues (green), such as marrow and brain, to stiffer tissues (red), including lung, skin, muscle, and bone. **(B)** Large-scale, chromosome-level mutations likewise increase with stiffness: childhood cancers in stiffer tissues have 10-to-20-fold more chromosome copy number changes and structural variants than do cancers in softer tissues, while somatic mutation rates differ much less. **(C)** (*i*) Melanomas from patients of ≤60 years have fewer copy number changes than melanomas from patients over 60. The younger patients also have softer, less fibrotic skin, as inferred from their lower average solar elastosis score; solar elastosis is the thickening of skin due to prolonged sun exposure. (*ii*) In skin cancer genomes, chromosome copy number changes increase strongly with somatic mutation rate and lesion stiffness, with all highest in "invasive melanoma."

3.3. Mechanical causes of mutation in the correlation of genomic variation with tissue stiffness

Scaling of genomic variation with tissue stiffness could result from at least three possible mechanical sources of mutations. First, stiff matrix enhances cell proliferation, as has been shown by an increase in BrdU incorporation with substrate stiffness in 2D cultures of normal human smooth muscle and breast epithelial cells as well as mouse embryonic fibroblasts (Klein *et al.*, 2009). DNA replication in each cell division cycle carries with it some risk of spontaneous mutation (Lawrence *et al.*, 2013; Seshadri *et al.*, 1987), accounting for about 67% of mutations in human cancers (Tomasetti, Li, & Vogelstein, 2017). Since these mutations accumulate over successive generations, more proliferation should mean more changes to the genome. Nowak and Waclaw (Nowak & Waclaw, 2017) recently pointed out for the case of one-hit, oncogenic initiation that cancer risk scales (in log-log plots) with the division rate of the resident tissue stem cells with a power law of 0.53, which is lower than linear scaling as expected for a simple stem cell contribution (Tomasetti *et al.*, 2017). Tissue geometry was speculated to suppress the 'effective number of stem cell divisions' (Nowak & Waclaw, 2017). More study is needed, especially in 3D, because a 3D stiff surrounding could, physically impact the fidelity of replication and chromosome segregation during mitosis.

A second conceivable explanation for the scaling relationship is that stiffness increases the frequency of nuclear envelope rupture (Tamiello *et al.*, 2013). Such rupture causes transient leakage into the nucleus of cytoplasmic factors, including perhaps nucleases, that might damage DNA and contribute to genome instability (Maciejowski *et al.*, 2015). However, the increase of rupture frequency with substrate stiffness has been

observed only in cells with defects in lamin-A, which is one of the three intermediate filament proteins that confer strength and stability to the nucleus. Yet, cancer types vary widely in their lamin-A expression levels: it is downregulated in leukemia as well as in breast and lung cancers, whereas it is upregulated in colorectal and skin cancers (for review: (Irianto *et al.,* 2016)). Lamin-A is highly mutated in multiple laminopathies, but cancer risk is not reported to be elevated. The inconsistency in lamin-A levels across cancer types argues against a simple stiffness-induced nuclear rupture hypothesis.

A third explanation that we find more promising is based on invasion of cells through stiff tissues, given that invasion is a 'hallmark' of cancer. Tissue stiffness increases with fibrous protein (e.g. collagen) concentration (Swift *et al.*, 2013), which, in turn, anti-correlates with extracellular matrix pore size (Yang *et al.*, 2009) (**Fig. 3.2A**). Hence, cancer cells invading normal tissue, as during tumor growth (Liotta, Steeg, & Stetler-Stevenson, 1991), encounter higher collagen matrix levels and smaller pores in stiffer tissues than in softer ones (Irianto *et al.,* 2016). Squeezing through small pores—but not larger ones—greatly deforms the nuclei of invading cancer cells (Harada *et al.*, 2014) and has several consequences. For one, constricted migration segregates mobile nuclear factors away from DNA (Irianto *et al.,* 2016). Among cells in static culture, hetero/eu-chromatin occupies roughly 50-70% of the nuclear volume per previous estimates from molecular mobility (Bancaud *et al.*, 2009), and we have shown for various cancer cell lines that the chromatin volume fraction can increase locally to 100% as the nucleus enters a small constriction. Conversely, *all* mobile proteins in the nucleus, including those that function as key DNA repair proteins, are always seen to deplete within the constriction (Irianto *et al.*, 2016). Such unavoidable 'squeeze-out' of mobile nuclear

factors away from the constriction, where DNA concentration is highest, has important implications for the repair of DNA damage that might occur during replication, for example. Inactivating mutations in repair factors such as BRCA1 and BRCA2 are well-established risk factors for cancer and are sufficient cause for prophylactic mastectomy (i.e. preventative surgery), and so transient partial depletion of such factors could increase mutational probabilities.

In addition to inevitable squeeze-out of mobile repair factors, constriction can also cause rupture of the nuclear lamina (Harada *et al.*, 2014). Further studies with various cancer cell lines, immortalized epithelial cells, and primary dendritic cells, showed that migration through narrow channels can rupture the nuclear envelope and thereby permit cytoplasmic accumulation of GFP-tagged nuclear localization signal (NLS) constructs (Denais *et al.*, 2016; Raab *et al.*, 2016). Rupture—and the ensuing nucleo-cytoplasmic exchange—occurs more frequently after knockdown of lamin-A and is followed by focal enrichment of an overexpressed DNA damage factor, which the authors interpreted as evidence of DNA damage and speculated on the entry of cytoplasmic nucleases (Denais *et al.*, 2016; Raab *et al.*, 2016). If nuclease entry were responsible for constriction-induced DNA damage, then we would expect to see enrichment of damage foci near the site of nuclear envelope rupture. However, recent pore migration studies of an osteosarcoma line (U2OS), a lung carcinoma line (A549), and primary human mesenchymal stem cells have all shown by multiple measures of DNA damage (especially foci of γH2AX and phospho-ATM) that constricted migration produces a pan-nucleoplasmic distribution of DNA damage foci. This distribution suggests a global—rather than rupture site-specific—DNA damage mechanism; the distribution is consistent with transient knockdown of DNA

repair proteins (Irianto *et al.*, 2017; Irianto *et al.*, 2016). Similar depletion on the hours-long timescale of migration could likewise delay repair of replication errors, leading to the observed accumulation of DNA damage in migrated cells.

Importantly, the recent studies of DNA damage incurred during constricted migration also provided the first evidence of propagatable mutations. The genomes of serially migrated clones were analyzed by comparative genome hybridization arrays (aCGH), single-nucleotide polymorphism arrays (SNPa), and whole-exome sequencing (as well as RNA sequencing). Compared to unmigrated control clones, the migrated cells exhibited elevated chromosome copy number changes (Irianto *et al.*, 2017), suggesting that such chromosome-level abnormalities are characteristic of constricted migration. Recall that our meta-analysis showed that copy number changes and structural variants scale with normal tissue stiffness, perhaps more so than somatic mutations (**Fig. 3.1B, C**). Hence, constricted migration and stiffness seem to share a mutational signature, namely large-scale genome instability. This signature also resembles that of osteosarcomas and breast and ovarian cancers with BRCA deficiencies (Kovac *et al.*, 2015), although more such analysis is needed. Taken altogether, these genomic analyses hint at a connection between stiffness, constricted migration, and repair factor depletion (**Fig. 3.2C**). Thus, these studies tentatively support the hypothesis that loss of DNA repair during migration of cancer cells through small pores in fibrous matrix could underlie the scaling relation between mutation rate and tissue stiffness (**Fig. 3.1**).

Figure 3.2. Tissue stiffness increases with matrix density, which anti-correlates with interstitial pore size

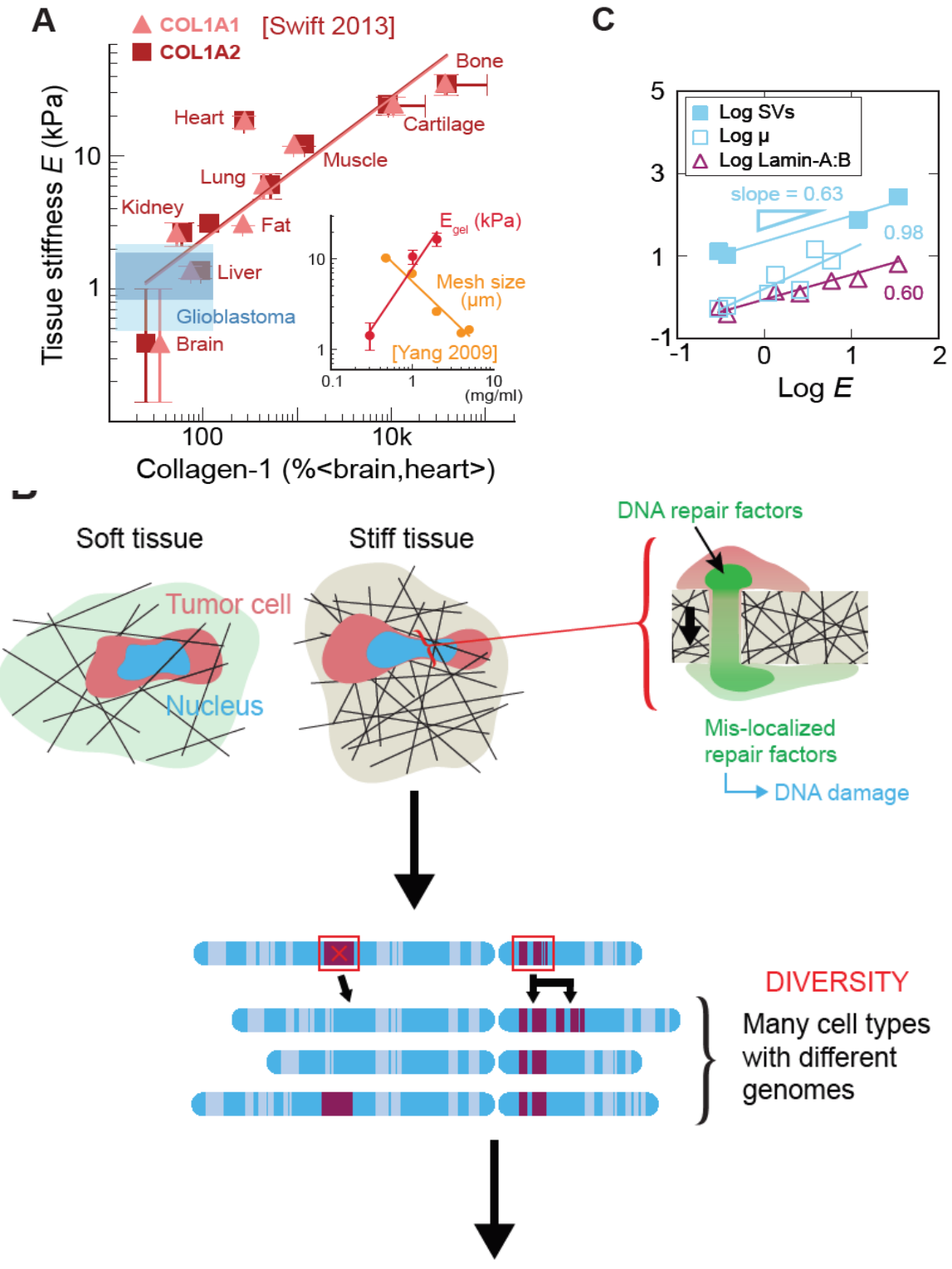

Figure 3.2. Tissue stiffness increases with matrix density, which anti-correlates with interstitial pore size. (A) Normal tissue microelasticity scales with collagen concentration. Blue shading indicates the range of stiffness values for 22 glioblastoma tumors, measured using multifrequency magnetic resonance elastography. Evidently, brain tumors remain soft *in vivo* despite intratumor heterogeneity. **(inset plot)** At the collagen concentration at which pure collagen-1 gels exhibit a high tissue-like stiffness, they have a mesh size of a few microns or less. **(B)** Cancer cells sustain severe nuclear stress during tumorigenic invasion into small holes in stiff, fibrous tissues. This stress causes global loss of DNA repair factors via both 'squeeze-out' and nuclear envelope rupture. Perhaps due to repair loss, migrated cells exhibit elevated DNA damage, which ultimately leads to genome instability. **(C)** Somatic mutation rate (μ), structural variant (SV) number, and lamin-A expression all correlate with tissue stiffness.

3.4. Genomic variation gives rise to targetable neoantigens

Genome changes, including those induced by a stiffness-related mechanism, can affect gene expression and lead to protein changes, which can contribute to a cancerous phenotype or merely be recognizable passenger mutations (Martin *et al.*, 2015; Matsushita *et al.*, 2016; Schumacher & Schreiber, 2015). For example, in our studies of genome variation caused by constricted migration, one clone acquired after migration a spindle shape and migrated through pores much faster than other clones. Further experiments attributed this distinct phenotype to upregulation of the transcription factor GATA4 (Irianto *et al.*, 2017), which influences a program for microtubule organization. Microtubules are well known to be the most rigid polymers in cells and help direct cell migration.

Stiffness can also directly affect the expression of genes, so in a cancer like melanoma where tissue stiffness increases with invasiveness (**Fig. 3.1C**), some genes are expected to be upregulated. If these genes are also mutated — by a 'mechanogenomics' process or otherwise, then they could present neoantigens to the immune system. Neoantigens, or altered proteins, are 'foreign' in being distinct from anything in healthy cells and can thus be used therapeutically to target diseased cells. As an example, tissue stiffness causes systematic upregulation of lamin-A over a 20-to-30-fold range (Swift *et al.*, 2013) (**Fig. 3.2B**). Mutations in lamin-A have been reported in The Cancer Genome Atlas (TCGA): one case study showed about 4% of 287 melanoma patients exhibited either amplifications (2%) or mis-sense passenger mutations (2%) in lamin-A's coding sequence, with no statistically significant impact on patient survival (http://bit.ly/2oUMGyL). Lamin-A is nonetheless one conceivable source of neoantigen

that – when mutated – associates with tissue stiffness. Future studies of such upregulated, mutated genes should yield other candidates.

Efforts to therapeutically target neoantigens, including those that arise in a stiffness-dependent way, are complicated by intratumor heterogeneity: different cells from a single tumor have been found to vary widely in their somatic mutations (Gerlinger *et al.*, 2012; Lawrence *et al.*, 2013). This heterogeneity reduces the probability of finding a ubiquitous, targetable mutation present in all a patient's cancer cells. Promising candidates—mutations that are relatively common among tumor cells—are those that occur early in cancer development (Bruin *et al.*, 2013), as tumor heterogeneity increases with cancer progression (Gerlinger *et al.*, 2012). Conceivably, heterogeneity rises because cancer cells sustain additional mutations as they invade small pores in surrounding tissue during tumor growth. Of course, therapies designed against even the most widely expressed neoantigen will likely produce negative selection, leading to the survival of cancer cells that are largely or wholly deficient in that neoantigen. The ideal therapy must therefore target several different neoantigens, which requires cancer cells to have a high mutation burden since not all neoantigens are targetable (Martin *et al.*, 2016). Indeed, in non-small cell lung cancer, high mutation load is associated with improved clinical response to immunotherapy (Rizvi *et al.*, 2015).

Though next-generation sequencing offers a means to identify neoantigens, more development is needed before this technology can be implemented clinically, as neoantigens vary within individual tumors as well as between patients (Heemskerk, Kvistborg, & Schumacher, 2013; Rajasagi *et al.*, 2014; Robbins *et al.*, 2013). Cancers of a given type often share mutated driver genes (McGranahan *et al.*, 2015), which yield

similar abnormal protein phenotypes, but changes can vary between patients. Hence, therapies for different patients must target different peptide sequences (Jo *et al.*, 2016; Schumacher & Schreiber, 2015; Segal *et al.*, 2008). This variability makes it necessary to isolate and sequence every individual tumor to identify its unique neoantigen profile, which remains a resource-intensive challenge for current sequencing (Li *et al.*, 2015). If the technology continues to advance, it is exciting to consider that personalized neoantigen-based therapy could enter clinical practice (LeBlanc & Marra, 2015; Schwaederle *et al.*, 2014).

3.5. Diverse neoantigen-based immunotherapies are currently under development

Neoantigen-based therapies can take various approaches. Some therapies target proteins expressed on the plasma membrane, relying on surface protein expression level to distinguish cancerous cells from healthy ones. In one of the most-used such therapies, chimeric antigen receptor (CAR) T cells target the B-lymphocyte antigen CD19 (Ramos *et al.*, 2015). While CD19 is expressed on over 95% of B-cell malignancies, it is also expressed on healthy B cells, making the latter susceptible to off-target effects (Turtle *et al.*, 2016). However, the ongoing discovery of surface neoantigens, such as mucin-1 (MUC1, which is also in the extracellular matrix and leaks into serum), that have irregular glycosylation patterns in cancer cells makes it possible to engineer CARs to target these unique glycosylations, thus minimizing deleterious side effects (Posey *et al.*, 2016; Sabbatini *et al.*, 2007). Most neoantigens are not expressed on the plasma membrane, but rather in the nucleus or cytoplasm of the cell (Kandoth *et al.*, 2013), so chemotherapeutics, which readily penetrate the cell membrane, can be effective against them. However,

chemotherapeutic agents are difficult to modify against different peptide sequences since any change in their structural chemistry can radically alter pharmacokinetics. Although the chemotherapy drug Vemurafenib effectively targets the *BRAF V600* mutation, it is ineffective against other *BRAF* mutations (Klein *et al.*, 2013; McArthur *et al.*, 2014), which reinforces the need to identify each patient's unique mutation profile.

Other approaches use nuclear and cytoplasmic neoantigens to develop vaccines and checkpoint inhibitors (Hodi *et al.*, 2010). These approaches take advantage of the major histocompatibility complex class I (MHC I), which presents peptide fragments—8-10 amino acids long—that are continuously screened by the immune system for foreign peptide sequences (Schumacher *et al.*, 2014). Unfortunately, mutated peptide sequences in cancerous cells often go undetected because they either have poor MHC I affinity, differ little from their wild-type counterparts, or are abetted by high levels of the cancer cell-derived immune inhibitory ligand PD-L1 (Assarsson *et al.*, 2007; Matsushita *et al.*, 2016; Paul *et al.*, 2013; Strickland *et al.*, 2016; Verdegaal *et al.*, 2016; Wick *et al.*, 2014). PD-L1 inhibitors can counteract this tumor-induced immune suppression (Pardoll, 2016). Sequencing is now being used to identify cancerous mutations in oncogenic drivers like KRAS and p53 that might also have high MHC I affinity as needed for vaccination therapy (Carbone *et al.*, 2005; Rahma *et al.*, 2014).

An alternative vaccination approach exploits MHC class II molecules expressed by macrophages (Liu *et al.*, 2016; Ly *et al.*, 2013). Like MHC I, MHC II presents peptide fragments at the cell surface. But whereas detection of a foreign sequence triggers cell destruction by the immune system in the MHC I case, it triggers activation of the adaptive immune system—against other cells weakly presenting that same foreign sequence—in

the MHC II case. Macrophages use MHC II to present peptide sequences from foreign organisms or viruses that they have phagocytosed. Unfortunately, macrophages do not eat cancerous cells in part because the latter overexpress CD47 (Willingham *et al.*, 2012), which is a 'marker of self' that inhibits phagocytosis (Tsai & Discher, 2008). The immune system is therefore not activated by MHC II presentation of neoantigens (Liu *et al.*, 2015). However, macrophages have long been engineered *ex vivo* for anti-cancer purposes and can be made to express patient-specific cancer neoantigen peptide sequences loaded into MHC II (Liu *et al.*, 2016). Upon injection back into the patient, these engineered macrophages activate the immune system against cancer cells that display the special peptide sequence. Numerous clinical trials conducted over the past two decades demonstrate that adoptive transfer of macrophages into humans shows little to no toxicity at doses of 1.5 billion cells (Andreesen *et al.*, 1998; Faradji *et al.*, 1991; Hennemann *et al.*, 1998). Strategic engineering of 'self' markers like CD47 should further reduce autoimmune toxicity by eliminating the need for systemic inhibition of CD47, which leads to rapid loss of red blood cells (RBCs) and in some mice to autoimmune responses, including production of anti-RBC antibodies (Oldenborg *et al.*, 2000; Willingham *et al.*, 2012).

One new macrophage-based therapy aims to exploit neoantigens without the need for extensive sequencing or artificial targeting vectors (e.g. CARs). Tumor associated macrophages (TAMs) can, through inhibition of CD47, phagocytose cancer cells (Weiskopf *et al.*, 2013), and then present neoantigens from those cells to activate the adaptive immune system (Liu *et al.*, 2015). However, TAMs promote tumor growth, are weakly phagocytic even with CD47 disruption, and have low MHC II expression, which

hinders their ability to activate an adaptive immune response (Liu *et al.*, 2016; Lu-Emerson *et al.*, 2013; Rodríguez *et al.*, 2013). A cell therapy approach using marrow-derived monocytes and macrophages could be an alternative, as these cells have low SIRPα (i.e. the inhibitory receptor that interacts with CD47) and high MHC II expression (Lavin *et al.*, 2014). In addition, marrow-derived monocytes and macrophages are highly migratory and can traffic into solid tumors (Pan *et al.*, 2013) **(Fig. 3.3A)**. However, like cancer cells invading nearby tissue, these 'invading' immune cells might also suffer DNA damage, with consequences yet unknown. The absence of oncogenic driver mutations probably limits the cancerous potential of infiltrating monocytes and macrophages; any DNA damage in these cells might instead contribute to senescence (Zglinicki *et al.*, 2005).

Lastly, while novel cell therapy approaches with infiltrating immune cells seems an encouraging but challenging future direction for the field of neoantigen-based immunotherapy, the microenvironment-dependent plasticity of such cells is also emerging from modern systems biology methods (**Fig. 3.3B**) and must be factored into cell function. Interestingly, for monocytes and macrophages, at least some genes in published profiles (e.g. lamin-A) increase with tissue stiffness, consistent with mechanically regulated epi-genetic processes in normal cells (Swift *et al.*, 2013) and likely also in cancer cells (Dupont *et al.*, 2011; Spencer *et al.*, 2007). Further RNA profiling of tissue macrophages, including TAMs, needs to be done using identical markers across different tissues, as macrophage transcriptomics would be expected to change when sorted on different markers (**Fig. 3.3B**).

Figure 3.3. Monocyte/macrophage-based immunotherapies target neoantigens while exploiting the ability of phagocytic cells to infiltrate solid tumor tissues

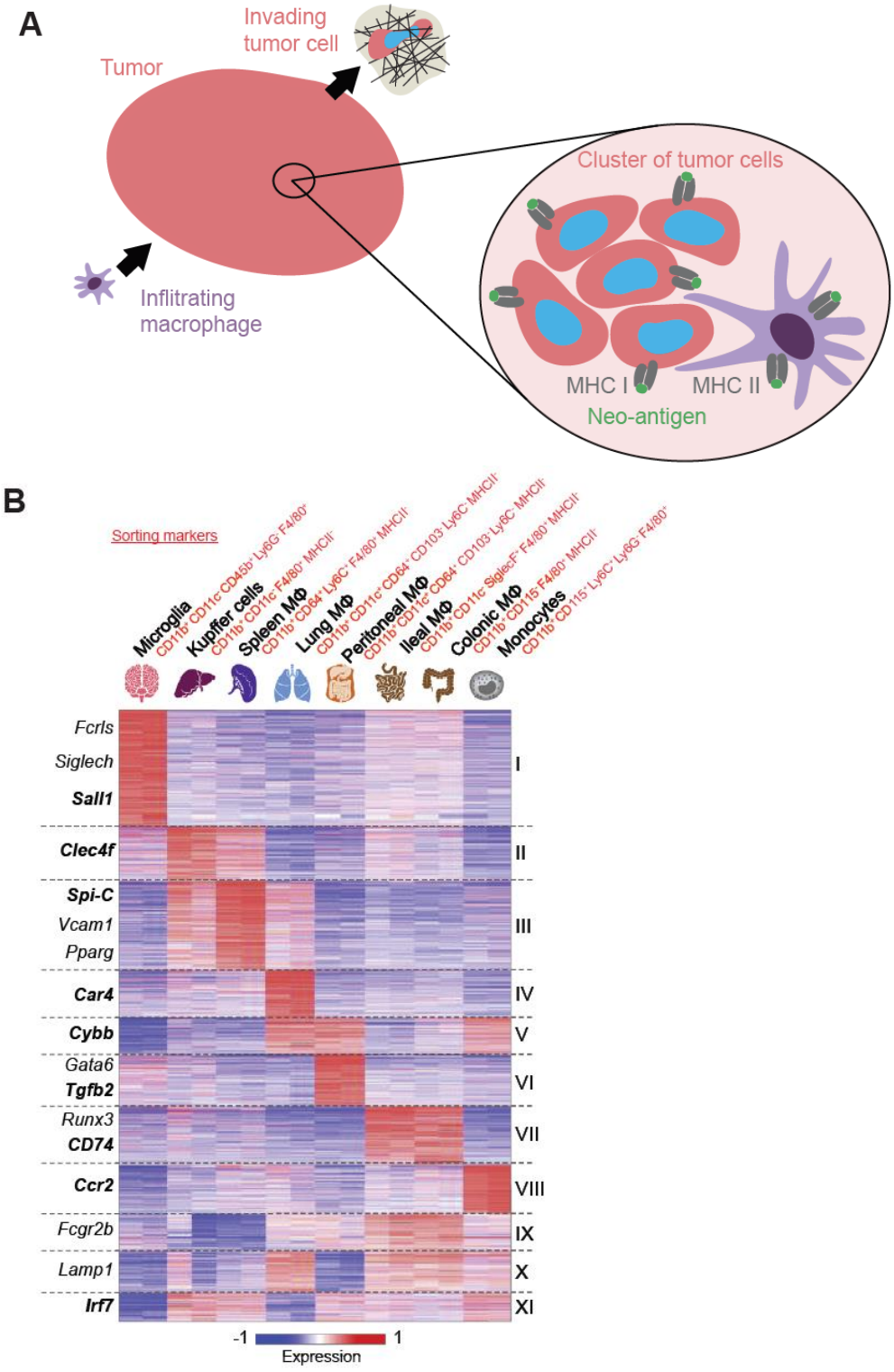

Figure 3.3. Monocyte/macrophage-based immunotherapies target neoantigens while exploiting the ability of phagocytic cells to infiltrate solid tumor tissues. (A) Immune cells must first migrate into tumors to attack 'non-self' cancer cells. Then, macrophages use MHC II to present neoantigens from cancer cells that they have phagocytosed. **(B)** Systems biology approaches are beginning to illuminate the microenvironment-dependent plasticity of monocytes and macrophages. Adapted from (Lavin *et al.*, 2014).

3.6. CONCLUSION

The meta-analysis here of recently published sequencing data reveals that somatic mutation rate increases with normal tissue stiffness across cancer types, while the rate of larger-scale, chromosome-level mutations increases even faster. Among various hypotheses that seek to explain this scaling relationship, the one that we consider most promising holds that stiffer tissues have smaller extracellular matrix pores, which can increase DNA damage in invading cancer cells, leading perhaps to genomic variation. In the case of immune cells that might infiltrate solid tumors—and go on to recognize neoantigens—similar damage has not yet been observed. Since such healthy cells lack driver mutations, they are unlikely to become oncogenic, but they can be expected to differentiate, perhaps even in relation to tissue stiffness.

Chapter 4: SIRPα-inhibited, marrow-derived macrophages engorge, accumulate, and differentiate in antibody-targeted regression of solid tumors

This chapter presents work featured in the research article:
Alvey, C.M., Spinler, K.R., Irianto, I., Pfeifer, C.R., Hayes, B., Xia, Y., Cho, S., Dingal, D., Hsu, J., Smith, L., Tewari, M., and Discher, D.E. (2017) *Current Biology*, online June 29.

Spinler, K. R. – CD47 KD A549 studies (Figure. 4.3)

Irianto, I. – mRNA analysis, confocal imaging, and FRAP experiments (Fig. 4.4, Fig. 4.1, and 4.S1)

Pfeifer, C.R. – Transwell experiments (Fig. 4.2 and Fig. 4.S4)

ABSTRACT

Marrow-derived macrophages are highly phagocytic, but whether they can also traffic into solid tumors and engulf cancer cells is questionable, given the well-known limitations of tumor-associated macrophages (TAMs). Here, SIRPα on macrophages from mouse and human marrow was inhibited to block recognition of its CD47 ligand, a 'marker of self' on all other cells. These macrophages were then systemically injected into mice with fluorescent human tumors that had been antibody targeted. Within days, the tumors regressed, and fluorescence analyses showed that the more the SIRPα-inhibited macrophages engulfed, the more they accumulated within regressing tumors. Human marrow-derived macrophages engorged on the human tumors, while TAMs were minimally phagocytic, even toward CD47-knockdown tumors. Past studies have opsonized tumors *in situ* with antibody and/or relied on mouse TAMs but have not injected SIRPα-inhibited cells; also, unlike past injections of anti-CD47, blood parameters remained normal here. Consistent with tumor-selective engorge-and-accumulate processes *in vivo*, phagocytosis *in vitro* inhibited macrophage migration through micropores that mimic features of dense 3D tissue. Accumulation of SIRPα-inhibited macrophages in tumors favored tumor regression for 1-2 weeks, but donor macrophages quickly differentiated toward non-phagocytic, high-SIRPα TAMs. Analyses of macrophages on soft (like marrow) or stiff (like solid tumors) collagenous gels demonstrated a stiffness-driven, retinoic acid-modulated upregulation of SIRPα and a mechanosensitive nuclear marker, lamin-A. Mechanosensitive differentiation was also evident *in vivo* and likely limited the anti-tumor effects, as confirmed by re-initiation of tumor regression by fresh injections of SIRPα-inhibited macrophages.

4.1 INTRODUCTION

Macrophages and monocytes engorge and accumulate within solid tissues in various inflammatory diseases (Bogdanik *et al.*, 2016; Moore, Sheedy, & Fisher, 2013), but general mechanisms are obscure and any relevance of 'engorge and accumulate' to solid tumors is unclear. Tumor associated macrophages (TAMs) are highly motile even within highly collagenous solid tumors (Condeelis & Pollard, 2006), but TAMs are differentiated and less phagocytic than macrophages in other tissues (Rodriguez *et al.*, 2013), with a high density of TAMs correlating with poor clinical prognosis (Fujiwara *et al.*, 2011; Lan *et al.*, 2012; Lu-emerson *et al.*, 2013; Zhang *et al.*, 2013). Recent studies show blood-borne 'patrolling monocytes' pinch off tumor material within hours of cancer cells lodging in the lung after intravenous injection of the tumor cells (Hanna *et al.*, 2015), but it is unclear whether such bone marrow derived phagocytes can be made to migrate into a well-established solid tumor, completely engulf a cancer cell, and maintain phagocytic phenotype. Injections into humans of ~10^9 macrophages (or ~10^6 for mouse) together with tumor-targeting antibodies can be safe, but have little impact on tumors (Andreesen *et al.*, 1998; Chokri *et al.*, 1992; Hennemann *et al.*, 1997; Lacerna *et al.*, 1988).

How any cell avoids being engulfed by a macrophage could partially involve signaling by "marker of self" CD47 to the phagocyte's receptor SIRPα (Oldenborg *et al.*, 2000; Willingham *et al.*, 2012). SIRPα signaling at a phagocytic synapse ultimately inhibits myosin-II that otherwise makes engulfment highly efficient (Tsai & Discher, 2008). Systemic injection of anti-mSIRPα binds to splenic macrophages and indeed causes rapid clearance of circulating components (Rodriguez *et al.*, 2013). However, SIRPα contributes to other processes (Alenghat *et al.*, 2012), and the viability of *Cd47*

knockout mice shows "marker of self" signaling is non-essential (Oldenborg *et al.*, 2000; Willingham *et al.*, 2012). Nonetheless, *in situ* knockdown of mCD47 starting ~1 wk after tumor engraftment (Wang *et al.*, 2013) can slow tumor growth for ~2 wks even without added TAM-activating factors (eg. tumor-opsonizing Ab); and systemic poisoning of macrophages also ameliorates this tumor suppression. Additionally, in *mice* with *human* tumor xenografts, systemic injection of anti-*h*CD47 plus a distinct Ab that opsonizes human cancer cells can shrink tumors (Chao *et al.*, 2010; Weiskopf *et al.*, 2013). In such studies, however, direct measurements are lacking for cancer cell engulfment by macrophages in tumors. Also, CD47 is expressed on all cells, and so species-matched anti-CD47 injections understandably cause rapid and reproducible (Horrigan *et al.*, 2017) depletion of blood cells in primates (Weiskopf *et al.*, 2013) and mice (Willingham *et al.*, 2012). Such side effects and complexity in phagocytic synapse interactions have been reviewed in our recent summary of nascent clinical trials (Alvey & Discher, 2017) and all together motivate deeper study of the basic biology of macrophage trafficking, phagocytosis, and differentiation in tumors.

Here we study these biophysically intensive processes by systemically injecting highly phagocytic marrow macrophages after inhibiting their SIRPα and pre-loading their Fc-Receptors with cancer-targeting Ab's. Such preparations increase phagocytosis in culture (Okazawa *et al.*, 2005; Oldenborg *et al.*, 2000), but systemic trafficking and 3D microenvironments add considerable complexity. Some simplicity is gained here with human-derived tumor models in NSG mice (non-obese diabetic/severe combined IL-2Rγ mice) that lack T-cells, B-cells (and Ab's), as well as NK-cells while maintaining

functional monocytes, macrophages, and neutrophils (McIntosh *et al.*, 2015; Quintana *et al.*, 2012).

4.2 MATERIALS AND METHODS

Antibodies: Receptor inhibition was done with anti-hSIRPα antibody (SIRP-A1, SE7C2, Santa Cruz, sc-23863) and with anti-mSIRPα antibody (rat anti-mouse CD172a, P84, BD Pharmingen). Opsonization of human cells was done with anti-human antibody (anti-hum, rabbit polyclonal IgG made against human RBCs, Rockland, 109-4139). Anti-hum antibody has been found to bind to the following human cell types: A549 (Fig. S2), RBC (Fig. S2), Huh7, and HepG2. However, it does not bind to any mouse cell type tested: RBC (Fig. S2), EC4 (Fig.S2), and C2C12. Furthermore, mouse blood cells do not deplete following repeated systemic injection of 600 μg of anti-hum (Fig. 6D, S8). Primary antibodies used for flow cytometry and imaging included anti-human CD41-FITC (Biolegend), CD47-APC (B6H12, Biolegend), CD47-Alexa Fluor 647 (B6H12, BD Pharmingen), CD235a-PE (Biolegend), and CD11b-APC (Biolegend) as well as anti-mouse F4/80-APC/Cy7 (Biolegend) and CD11b-PE/Cy7 (Biolegend). Secondary antibodies included donkey anti-rabbit Alexa Fluor 488 (Invitrogen) and donkey anti-rabbit Alexa Fluor 647 (Invitrogen). When required, nuclei were stained by either 7-Amino-actinomycin D (7-AAD, Sigma) or Hoechst 33342 (Invitrogen).

Human Specimens: Fresh human bone marrow was purchased from AllCells (Cat#: ABM001-1) in 3 mL quantities from healthy donors. AllCells received IRB approval from Alpha (Protocol #7000-SOP-046) which includes donor consent. In total, there were 4 different donors. Donors were all anonymous to the authors of this study, and experiments were all conducted at the University of Pennsylvania with IRB approval (Protocol #

808191) from review board IRB#7. Subject 1: Female age 30, subject 2: Female age 31, subject 3: Male age 31, subject 4: Male age 22 with additional details provided by AllCells per (**Fig. 4.7A**). Marrow was pooled and divided among the different experimental conditions in **Fig. 4.7**.

Murine Specimens: Male and female NSG mice that >6 weeks old were purchased from either The Jackson Laboratory or the Stem Cell and Xenograft Core at the University of Pennsylvania under IACUC approved protocols (#805977 and #804455) which adhere to all regulatory standards. Blood, lung, liver, spleen, and marrow were obtained from these mice following the same IACUC approved protocols. The health of the mice was assessed prior to the start of each experiment by veterinary technician and was not used if unhealthy. Mice were never used for more than one experiment. Mice are housed in dedicated BSL-2 animal barrier space equipped for all necessary procedures.

Cell Lines: ATCC (American Type Culture Collection, Manassas, VA, USA) is a biological materials resource and standards organization with external accreditation from the International Organization for Standardization (ISO), and ATCC provides cell line authentication test recommendations per Tech Bulletin number 8 (TB-0111-00-02; yr. 2010). This bulletin recommends five types of tests (underlined) for the authentication of cell lines. Cell morphology check by microscopy, growth curve analysis, and mycoplasma detection by DNA staining (for filaments or extracellular particulates) were conducted on all cell lines used in these studies, and all cell lines maintained the expected morphology and standard growth rates with no mycoplasma detected. Two additional, ATCC-

recommended authentication tests were conducted on the A549 cell line as the A549 cells were used in all of the main and supplemental figures. Species verification of A549 cells as human by RNA sequencing detection of uniquely human sequence (Figure 4), by mass spectrometry detection of uniquely human sequence (Figure S1), and by antibody targeting with anti-human Abs (Figures 1-4,5-6; Figures S1-S6). Identity verification from DNA of A549 was confirmed using SNP arrays (SNPa). DNA was isolated by using the Blood and Cell Culture DNA Mini Kit (QIAGEN) per the manufacturer's instructions, and DNA samples were sent to The Center for Applied Genomics Core in The Children's Hospital of Philadelphia for the SNPa HumanOmniExpress-24 Bead Chip Kit (Illumina), with >700,000 probes along the entire human genome. For each sample, the Genomics Core provided the data in the form of GenomeStudio files (Illumina). Chromosome copy number was analyzed in GenomeStudio with the cnvPartition plugin (Illumina). SNP array experiments also provide genotype data, which was used to give SNV data. Genotyping in this Illumina system relies on the correlation between total intensity and intensity ratio of the two probes, one for CG and another for AT. These correlations were mapped to a standard clustering file (Illumina) to give the SNP calls. Consistent with ATCC 's karyotype analysis, SNPa show the A549 cells have a hypotriploid chromosome copy number of 66 with 2 copies of X and Y chromosome and 4 copies of chromosome 17. Further consistent with ATCC's descriptions of this cell line as Caucasian in origin, SNPa analyses also show that the cells have mostly European ancestry (~90%) (Dodecad2.1 an ancestry lineage algorithm based mostly on Illumina SNPa data).

Experimental Design: All experiments were replicated. Measurements and analysis, when applicable, were conducted blindly with stratified sampling. In the case of tumor growth and regression studies, mice were not stratified, but separated by tumor size to ensure all groups had the same average tumor size at the start of treatment. No data was excluded from any data set.

F(ab')2 Production: Anti-hum F(ab')2 were produced using a Thermo Scientific Pierce^{TM} F(ab')2 Preparation Kit. Briefly, immobilized pepsin was used to cleave full-length anti-hum antibody. After a 3-hour incubation, the pepsin was removed by centrifugation at 5000 g for 1 minute. A SDS-PAGE was then used to assess complete digestion. Following successful cleavage, Fc fragments were removed via an Amicon Ultra centrifugal filter device with a 50,000-molecular weight cut-off. F(ab'2) product from above was centrifuged in a filter at 5000 g for 30 minutes. After centrifugation, F(ab')2 was collected, and the filter membrane was washed with PBS. To verify that Fc fragments had been removed, the recovered F(ab')2 was run on a SDS-PAGE along with the filtrate.

Mass spectrometry to determine anti-human antigens: Mass spectrometry (MS) samples were prepared using the same procedures outlined in (Swift *et al.*, 2013). Briefly, ~1 mm^3 gel sections were excised from SDS–PAGE gels and were washed in 50% 0.2 M ammonium bicarbonate (AB), 50% acetonitrile (ACN) solution for 30 minutes at 37°C. The washed slices were lyophilized, incubated with a reducing agent [20 mM TCEP in 25 mM AB solution], and alkylated [40 mM iodoacetamide (IAM) in 25 mM AB solution].

The gel sections were lyophilized again before in-gel trypsinization [20 mg/mL sequencing grade modified trypsin, Promega] for 18 hours at 37°C with gentle shaking. The resulting tryptic peptides were extracted by adding 50% digest dilution buffer (60 mM AB solution with 3% formic acid) and injected into a high-pressure liquid chromatography system coupled to a hybrid LTQ-Orbitrap XL mass spectrometer (Thermo Fisher Scientific) via a nano-electrospray ion source**.**

Raw data from each MS sample was processed using MaxQuant (version 1.5.3.8, Max Planck Institute of Biochemistry). MaxQuant's built-in Label-Free Quantification (LFQ) algorithm was employed with full tryptic digestion and up to 2 missed cleavage sites. Peptides were searched against a FASTA database compiled from UniRef100 (June 2011) human, plus mouse and contaminants. The software's decoy search mode was set as 'revert' and a MS/MS tolerance limit of 20 ppm was used, along with a false discovery rate (FDR) of 1%. The minimum number of amino acid residues per tryptic peptide was set to 7, and MaxQuant's 'match between runs' feature was used for transfer of peak identifications across samples. All other parameters were run under default settings. The MaxQuant output tables were then fed into its custom bioinformatics suite, Perseus (version 1.5.2.4), for protein annotation and sorting.

Development of THP-1 SIRPα-KD Cell Lines: Stable SIRPα-KD cell lines were established using a standard transduction protocol, as described above. Briefly, human SIRPα shRNA lentiviral transduction plasmids were purchased from Santa Cruz (sc-44106-SH). Plasmid was transfected into bacteria, allowed to replicate, and then harvested using a maxi plasmid isolation kit. Plasmid was sent to Wistar Institute to produce active

lentiviral particles. THP-1 cells were transduced with viral particles, and stable clones were generated by puromycin selection. The SIRPα knockdown efficiency was determined by antibody staining and flow cytometry.

Phagocytosis Assay: THP-1s were incubated in RPMI medium with 100 ng/mL phorbol myristate acetate (PMA) for 2 days. Where anti-hSIRPα antibody was used, macrophages were pre-incubated at 5.32 nM at 37°C for 1 hour prior to the addition of A549 cells. All conditions were supplemented with non-specific IgG (~30ug/mL) from FBS. A549s were prepared as follows: the cells were first removed using cell dissociation buffer Hanks (Invitrogen), and then incubated with anti-hum and B6H12 antibodies at 1 μM and 83 nM, respectively. The A549s were then combined with the THP-1s at a ratio of 5 to 1; this mixture was incubated for 75 minutes at 37°C, and then rinsed with PBS. Three-minute trypsin incubation was used to remove non-ingested A549s. The remaining cells were scraped off the plate and stained with CD11b (label THP-1s) and anti-rabbit-AF488 antibody (to distinguish non-ingested A549s). The cells were washed two times with PBS and resuspended in 5% FBS/PBS before being analyzed by a BD LSRII cytometer. Phagocytosis of human red blood cells followed the same protocol as described in (Sosale *et al.*, 2015). Briefly, RBC were opsonized with anti-hum and CD47 blocked with 0 to 270 nM anti-CD47 (B6H12). After shaking (Argos RotoFlex, 45 minutes, room temperature), RBCs were pelleted and labeled with PKH26 dye (room temperature, 30 minutes). RBCs were added to THP-1 and incubated for 30 mins. After, RBCs were lysed and THP-1 were removed with Trypsin followed by staining (10 minutes with Hoechst 33342).

Immunofluorescence: A549 cells were seeded on 18 mm circular microscope cover slips in a 6-well plate and allowed to adhere overnight. Cells were fixed with 4% paraformaldehyde for 15 minutes at room temperature (RT), and then washed three times with PBS. Next, cells were blocked for 30 minutes using 3% BSA + 0.05% Tween-20, followed by a 2-hour RT primary antibody incubation in blocking buffer. These primary antibodies were used at a 1:100 concentration. After incubation, cells were again washed three times with PBS. A 1:400 PBS dilution of donkey secondary antibodies (Alexa Fluor 488 and 647) was added for 1 hour at RT. Hoechst 33342—at a concentration of 1 μg/mL—was used to stain DNA for 15 minutes at RT. Cover slips were washed a final three times with PBS before being mounted on slides with ProLong Gold Antifade Reagent (Life Technologies), cured for 24 hours, and sealed with nail polish prior to imaging. Images were acquired by an Olympus IX71 inverted microscope with a 300W Xenon lamp illumination using 40×, 60×, or 150× objectives with or without 1.6× magnification. Image analysis was done in ImageJ (NIH).

Flow Cytometry of *In Vitro* Cultured Cells: A549 cells were dissociated using 10 mM trypsin in PBS, washed, and re-suspended in 2% FBS in PBS. Antibody incubation was done at RT for 1 hour, followed by washing and resuspension in 2% FBS. Samples were run on a BD LSRII.

Confocal Imaging: For confocal imaging and fluorescence recovery after photobleaching (FRAP) experiments, an inverted laser scanning confocal microscope (SP8, Leica) was

used, with a 63×/1.4NA oil immersion objective (Leica). FRAP time-lapse imaging was acquired at 37°C with 5% CO_2 in a humidified chamber for up to 10 minutes after photobleaching. Meanwhile, samples were cultured in phenol-red free complete DMEM medium. Image sequences were analyzed using ImageJ.

Establishment of A549 Tumors *In Vivo:* CD47 knockdown and wild-type A549s were dissociated from tissue culture flasks using 10 mM trypsin in PBS. For each injection, 10^6 or $2x10^6$ cells were suspended in 100 μL ice-cold PBS and 25% Matrigel (BD) and injected subcutaneously into the flank or intraperitoneal of non-obese diabetic/severe combined immunodeficient (NOD/SCID) mice with null expression of interleukin-2 receptor gamma chain (NSG mice). Treatment groups were a mix of male and female mice. Mice were obtained from the University of Pennsylvania Stem Cell and Xenograft Core or Jackson Laboratory. All animal experiments were planned and performed according to IACUC protocols.

***In Vivo* Tumor Imaging:** Mice were anesthetized via inhalation of isoflurane at 3 L/min and maintained at 1.5 L/min. Images were acquired using a Perkin Elmer IVIS Spectrum with excitation and emission filters set at 535 nm and 580 nm, respectively, optimized for tdTom imaging. Images of each face of the sagittal plane were taken to capture both left and right flanks. Mouse fur was soaked with ethanol to reduce auto fluorescence prior to imaging. Three fluorescent standards were used to subtract background fluorescence and calibrate IVIS Images were analyzed in ImageJ, where the length and width of the tdTom tumor was measured. Analysis of tdTom intensity was done using Living Image (Perkin

Elmer), which involved spectral unmixing of 10-13 images to sufficiently remove any tdTom auto-fluorescence from the mice.

Adoptive Transfer of NSG Bone Marrow: Femurs and tibias of donor NSG were removed, and bone marrow was flushed with 5% FBS/PBS. Red cells were lysed by incubation with RBC lysis buffer (Sigma) in 4% FBS/PBS for 12 minutes at RT. Cells were washed twice and resuspended in warm 5% FBS/PBS. Following the addition of 1:1000 CFDA-SE (Invitrogen), cells were incubated for 15 minutes at 37°C, and then centrifuged again, resuspended in warm complete DMEM medium, and incubated for an additional 30-40 minutes at 37°C. When applicable, anti-mSIRPα antibody was added during this incubation period. Cells were then washed, resuspended in 5% FBS/PBS, counted, and volume adjusted to allow injection of 10^6 cells. Remaining cells were analyzed by flow cytometry to establish initial composition.

Antibody Treatment: Mice were warmed under a heat lamp prior to tail vein injection. Opsonization of human cells was done with anti-human antibody (anti-hum, rabbit polyclonal IgG made against human RBCs, Rockland, 109-4139). Anti-hum antibody has been found to bind to the following human cell types: A549 (Fig.4.S1), RBC (Fig.4.S1), Huh7, and HepG2. However, it does not bind to any mouse cell type tested: RBC (Fig. 4.S1), EC4 (Fig. 4.S1), and C2C12. Furthermore, mouse blood cells do not deplete following repeated systemic injection of 600 µg of anti-hum (Fig.4.6D, 4.S6). Anti-hum Ab and serum purified rabbit IgG (Sigma, pre-immune) were reconstituted per manufacturer's direction and further diluted using sterile PBS. Mice were injected with

anti-hum 600 µg per animal (~20 mg/kg) twice a week. Mouse anti-human Mucin 1 (MA5-15131, ThermoFisher) and cetuximab (InVivogen) were administered twice a week at 10 µg each per mouse.

Engineered Human Marrow: Fresh human bone marrow (ABM001-1, AllCells) was incubated with 3 mL of red blood cell lysing buffer hybrid-Max (R7757, Sigma) for 12 minutes in a 15mL conical tube. Cells were then centrifuged at 2,000 rpm for 2.5 minutes, the lysate was removed, and the remaining cells were suspended in 3 mL of red blood cell lysis buffer for a second 12-minute lysis phase. After another 2,000 rpm, 2.5-minute centrifugation, cells were resuspended in 500 µL of PBS with 1 µL of 10 mM CFDA SE solution (prepared per kit instructions). Cells were incubated for 40 minutes at 37^{o}C and inverted 2-3 times every 5 minutes. After this incubation period, SIRPα-inhibiting and Fc-priming anti-human antibodies (109-4139, Rockland) were added to cells at 4 µg/mL and 100 µg/mL concentrations, respectively. Then, cells were twice centrifuged at 2,000 rpm for 2.5 minutes: the first time, they were resuspended in 1 mL of 5% FBS/PBS, and the second time, in 100 µL of 5% FBS/PBS. A cell count was performed using a hemocytometer, and cells were diluted to 40,000 cells per µL (8×10^6 cells total per mouse) for intravenous tail vein injection in tumor bearing mice. Mice that were treated with unprimed cells were injected intravenously with 600 µg (6 µg/µL) of human red blood cell antibody (Rockland) 4-6 hours prior to injection of engineered marrow cells.

***Ex Vivo* Tumor Flow Cytometry Analysis:** On the day of analysis, mice in the treatment cohort were injected with the standard antibody dose, as described above. Mice were

euthanized by cervical dislocation 1.5-2 hours after injection. Tumors and spleens were removed and placed in 20% FBS, and tumor core and periphery tissue were segregated. Tumor tissue was cut into 1-3 mm pieces, transferred to 15 mL centrifuge tubes, and centrifuged to remove media. Tissue was then resuspended in 3 mL warm Dispase (STEMCELL Technologies) supplemented with 3 mg/mL Collagenase (Sigma) and 200 µL of 1 mg/mL DNase I (Roche). Samples were mixed by pipetting for 1-3 minutes until cloudy but not stringy. Dissociation was quenched by addition of 10 mL room temperature PBS, and then the suspension was filtered through a 70 µm cell strainer. The filtrate was centrifuged, the supernatant discarded, and the pellet resuspended in 2% FBS for antibody incubation. Spleens were prepared by mechanical dissociation, filtration, and red blood cell lysis using Red Cell Lysing Buffer (Sigma). Lysed samples were washed and resuspended in 2% FBS for antibody incubation. Prior to antibody incubation, samples were blocked with 1:500 Fc Block (BD Pharmingen) for at least 5 minutes at RT. CD47-AF647 (1:25), donkey anti-rabbit AF488 or AF700 (1:400), donkey anti-rat AF647 (1:400), F4/80 APC-Cy7 (3:50), CD11b PE-Cy7 (1:25), Gr-1 APC (1:25), hCD47 AF647 (1.5:50), and Hoescht 33342 (1:1250) were incubated at RT for 1 hour. Following incubation, cells were washed and resuspended in 2% FBS.

Analysis of Mouse Blood Profiles: 100 µL of blood was isolated from anesthetized mice by retro-orbital bleeds. Blood was collected in Eppendorf tubes containing EDTA. Blood was kept at room temperature and immediately analyzed using a Drew Scientific Hemovet (HV950).

Graft vs Host Disease: Mice were monitored 3 times a week by researchers and veterinarian technicians at the University of Pennsylvania Perelman School of Medicine mouse facilities for general health and for development of GvHD. Classic signs of GvHD include weight loss (>15%), ruffled fur, loss of fur on the head and rear of the mouse, hunch posture, and reduced activity (Ali *et al.*, 2012; King *et al.*, 2009). Development of GvHD is a common occurrence at these facilities as numerous users study CAR T-cell therapies, which frequently cause GvHD (Jacoby *et al.*, 2016).

Sorting of Marrow Cells: In some experiments, marrow phagocytes were sorted from non-phagocytes and dendritic cells. FACS Aria (Biosciences (Helft *et al.*, 2015)) was used to sort 60 million marrow cells using anti-CD135-BV421 (Biosciences,) and anti-SIRPα – FITC (P84, Biosciences) into 15 mL conical tubes containing 1mL FBS. This sorting process generated 20 tubes, which were subsequently centrifuged for 10 minutes at 4,000 rpm. After the supernatant was aspirated, cells were resuspended in 5% FBS/PBS, incubated with targeting antibody for 1 hour, and centrifuged again. Finally, cells were resuspended in 200 µL of 5% FBS/PBS per 10×10^6 cells and put on ice for tail-vein injection.

3D Migration Assay: Migration assays were performed using 24-well inserts with 3 µm-, 5 µm-, and 8 µm-pore filters with 2×10^6, 4×10^5, and 1×10^5 pores per cm^2, respectively. Either tdTom A549s or 900 nm, 2.1 µm, or 6.7 µm beads (Thermofisher, streptavidin coated) were mixed with engineered marrow cells in a 10:1 ratio; 3×10^5 total cells were seeded on top of the pore filters. Beads were opsonized with anti-streptavidin antibody

(S6390, Sigma). The same 1:1 mixture of DMEM and F-12, supplemented with 15% FBS and 1% penicillin-streptomycin, was added to both the top and bottom of each 24-well insert such that there was no nutrient gradient across the pore filter. After incubating for approximately 24 hours at 37°C and 5% CO_2, cells were harvested from the tops of the filters using Trypsin and from the bottoms using both Trypsin and scraping. In some experiments, beads were pre-incubated with anti-SIRPα macrophages for 150 minutes prior to being plated on tops of transwells.

RNA Isolation and Sequencing: For RNA isolation, an RNeasy plus Mini Kit (Qiagen) was used. For RNA-seq analyses, RNA samples were sent to the Next-Generation Sequencing Core at the Perelman School of Medicine, University of Pennsylvania, PA. Libraries for RNA-seq were made using the TruSeq Stranded mRNA Library Prep kit (Illumina) per manufacturer instructions, followed by 100 bp paired-end sequencing with HiSeq 2500 (Illumina). Ten cDNA libraries were pooled together, resulting in ~16,000,000 reads for each sample.

Synthesis of soft and stiff polyacrylamide gels: Round glass coverslips (18 mm, Fisher Scientific) were cleaned in boiling ethanol and RCA solution (H_2O:H_2O_2:NH_4OH = 2:1:1 in volume) for 10 minutes each, and then functionalized in ATCS solution (chloroform with 0.1% allytrichlorosilane (Sigma) and 0.1% trimethylamine (Sigma)) for an hour. Fresh precursor solution for 0.3 kPa soft gels (3% acrylamide + 0.07% bis-arylamide in DI water) and 40 kPa stiff gels (10% acrylamide + 0.3% bis-acrylamide in DI water) were prepared. Afterwards, 0.1% N,N,N’,N’-tetramethylethylenediamine (Sigma) and 1%

ammonium persulphate (Sigma) were added to each precursor solution, and 20 µL of the resulting mixture were added to each coverslip to allow gel polymerization. To achieve collagen-I coating, crosslinker sulpho-sanpah (50 µg/ml in 50mM HEPES, G-Biosciences) was applied over the whole gel surface and photoactivated under 365nm UV light for 7 minutes. Excess sulpho-sanpah was washed away following UV activation, and then collagen-I solution (100 µg/ml in 50mM HEPES) was applied overnight at RT with gentle shaking.

Quantification and Statistical Analysis: All statistical analyses were performed using GraphPad Prism 4. Unless otherwise noted, all statistical comparisons were made by unpaired two-tailed Student *t* test and were considered significant if $p < 0.05$. Unless mentioned, all plots show mean ± SEM. "n" indicates the number of tumors, cells, or wells quantified in each experiment and is ≥3 in all experiments, except for RNA sequencing data which is for ≥ 2 samples per condition. Figure legends specify the exact meaning of "n" for each figure.

4.3 RESULTS

Engorge and accumulate: Donor MΦ in tumors are more phagocytic than TAMs

Two key issues to address first were (*i*) whether tail-vein injected marrow monocytes and macrophages (MΦ) traffic into a human solid tumor, and (*ii*) whether such cells can efficiently phagocytose human tumor cells. NSG mouse marrow cells were fluorescently labeled with the green dye (CFDA) and incubated with anti-SIRPα plus priming of Fc receptors with targeting Ab (**Fig. 4.1A – left**). Anti-mSIRPα clone P84 is well-known to promote phagocytosis of targets opsonized with other IgG's (Okazawa *et al.*, 2005; Oldenborg *et al.*, 2000; Rodriguez *et al.*, 2013; Yanagita *et al.*, 2017) even though P84 does not directly inhibit mCD47 binding to mSIRPα (Motegi *et al.*, 2008). P84 instead inhibits SIRPα diffusion, focal accumulation, and signaling at phagocytic synapses (**Fig. 4.S1**), which disrupts the normal 'self' signaling by CD47 (Tsai & Discher, 2008). Our opsonizing Ab's are simpler in function and are all human specific (**Fig. 4.S2**): monoclonal Ab's against MUC1 and EGFR (Cetuximab) have been clinically tested against lung cancers (Kufe, 2009; Pirker, 2013), and a polyclonal anti-human IgG (anti-hum) binds multiple antigens and can minimize selection of cancer cells that lose some antigens. Ten million freshly made "**A**ntibody-primed **P**lus anti-SIRPα **B**ound macrophages", denoted as **A'PB** MΦ were tail vein injected into NSG mice bearing large solid tumors of human lung carcinoma A549 cells expressing tdTomato (tdTom) (**Fig. 4.1A - middle**); studies with engineered T-cells likewise inject ~10^7 cells (Garcia-Hernandez *et al.*, 2010; Sample *et al.*, 2008; Zoon *et al.*, 2015). Mice were sacrificed 3 days after MΦ injections and systemic injections of targeting Ab's (**Table 4.S1** lists the standard amounts). Tumors and other tissues were quickly isolated, disaggregated, and

analyzed with a focus on immune cells that were tdTom+ using the surface markers F4/80 and (when possible) CD11b for tissue MΦ (Lavin *et al.*, 2014) (**Fig. 4.S3**).

Confocal imaging (**Fig. 4.1B**) of such a dispersed tumor from mice treated with A'PB MΦ's reveals adhesive interactions with cancer cells and cancer cell internalization into phagosomes. Complete engulfment is evident from an absence of secondary stain for opsonizing Ab which is otherwise abundant on tdTom+ A549 cells (**Fig. 4.S3**). The result indicates the MΦ are internalizing Ab together with Fc receptor, and the images of adherent aggregates are consistent with flow cytometry showing high Forward and Side Scatter for tdTom+ MΦ compared to tdTom- MΦ (**Fig. 4.S3**). All tdTom+ MΦ showed a similar average tdTom intensity equivalent to ~one A549 cell (**Fig. 4.1C**), with the most phagocytic cells (SIRPα inhibition; with green CFDA dye) showing higher intensity at a single cell level in flow cytometry than the least phagocytic cells (TAMs engulfing WT tumors). The distribution of tdTom intensities in MΦ is much broader and skewed to lower signal than the tight distribution for cancer cells (**Fig. 4.1C, histogram**); this suggests cancer cell degradation after engulfment. Human nuclei are also particularly prominent in imaging, and DNA-Hoechst stain intensities show recipient and donor tdTom+ MΦ have more DNA by about one cancer cell nucleus compared to tdTom negative MΦ (**Fig. 4.1C**).

TdTom+ donor MΦ were detected in tumors but not in marrow, spleen, or liver (**Fig. 4.1D**). This begins to suggest that donor MΦ traffic into tumors and once they phagocytose a cancer cell(s) they do not traffic elsewhere. Maximum phagocytic activity was found for the A'PB MΦ and for the 'unprimed' APB MΦ, with 90% of these donor MΦ in the tumors phagocytosing tdTom+ cancer (respectively: **Fig. 4.1D - inset left panel**). No difference in phagocytic activity of donor MΦ subpopulations was detected as

nearly all $CD11b^+$, $F4/80^+$, and $CFDA^+$ cells were tdTom+. Donor MΦ without SIRPα inhibition, but with systemic anti-hum Ab were less phagocytic, with 30% of such donor cells in tumors showing phagocytosed tdTom+ cells. Donor MΦ with SIRPα inhibition combined with pre-immune Ab primed on the Fc receptors were minimally phagocytic, with only 10% of MΦ in the tumors phagocytosing cancer cells despite systemic injections of the pre-immune Ab. TAMs were the least phagocytic of these WT tumors, with <5% of recipient MΦ in the tumors showing phagocytosis of cancer cells (**Fig. 4.1E - inset right panel**). This decreased by more than half in the absence of tail-vein injections of opsonizing Ab, but TAMs were clearly phagocytic toward CD47 knockdown tumors, with 12% in these KD tumors phagocytosing cancer cells after Ab injections (**Fig. 4.1F**). In the same KD mice, donor MΦ (without SIRPα inhibition) were 40% phagocytic upon tail-vein injection plus opsonizing Ab. Compared to TAMs, donor MΦ are more phagocytic.

TdTom+ MΦ were only detected in tumors and not in marrow, spleen, or liver, despite these tissues harboring some donor MΦ in addition to the expected recipient MΦ (**Fig. 4.1G**). Bone marrow has 35-50k monocyte or MΦ per 10^5 cells, which makes this a reasonable source of donor MΦ (**Fig. 4.S3**). The spleen and liver are known to filter out injected cells and particles, and bone marrow homing of at least some marrow-derived MΦ seems sensible. Nonetheless, donor MΦ injected shortly after systemic anti-hum Ab accumulate more so in tumors (per 10^5 cells) than the other tissues (**Fig. 4.1G**). Injections of 7.5M and 3.8M cells gave similar ~1.5k donor macrophages per 100k tumor cells. Our flow cytometry measurements of tumors are conducted on 2M total cells that constitute ~0.5-5% of total tumor volume, which equates to ~600k-6M donor macrophages infiltrating the tumors, so that any excess macrophages disperse to other tissues and/or die.

Importantly, A'PB macrophage distribute relatively evenly between tumor periphery and core whereas TAMs are more abundant in the core (**Table 4.S2**). Donor neutrophils accumulate in tumors 30-fold less than donor MΦ and are weakly phagocytic, and therefore, neutrophils likely contribute little to tumor shrinkage (**Fig. 4.S3**). Importantly, tumor accumulation increases linearly by almost 10-fold as donor MΦ are made more phagocytic (i.e. SIRPα-inhibited plus anti-hum Ab) (**Fig. 4.1G, upper inset plot**). Engorge and accumulate trends proved similar in intraperitoneal (IP) tumors (**Fig. 4.S3**). Highest in donor abundance are the APB and A'PB MΦ that achieve tumor numbers similar to resident TAMs. TAM abundance is nearly unaffected by tumor opsonization, consistent with minimal phagocytosis by TAMs.

To assess whether MΦ could impact tumor growth on their own, these cells were sorted from bulk marrow's non-phagocytic cells (eg. stem and progenitor cells) plus mature dendritic cells (DCs). Addition of SIRPα-inhibition plus anti-hum Ab to each fraction was followed by tail-vein injections into NSG mice bearing both subcutaneous and intraperitoneal (IP) tumors. The latter tumors model the distal invasiveness of lung cancer in previous studies with A549 cells (Riihimaki *et al.*, 2014). The non-phagocytes plus DCs failed to inhibit tumor growth, whereas the A'PB MΦ fraction shrunk all tumors within 3 days (**Fig. 4.1H**). Decreases in tdTom intensities *in vivo* by day-13 with anti-hum Ab match flow cytometry results for decreased cancer cell numbers (per 10^5 total cells) (**Fig. 4.S2**). Pre-immune Ab on A'PB MΦ had no effect on tumor growth (**Fig. 4.S3**).

Figure 4.1. ***In vivo*** **tumor phagocytosis and accumulation of engineered donor MΦ's can shrink tumors**

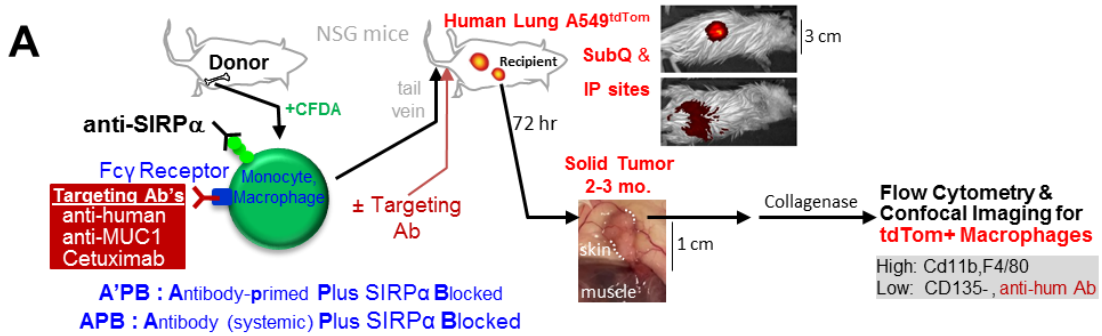

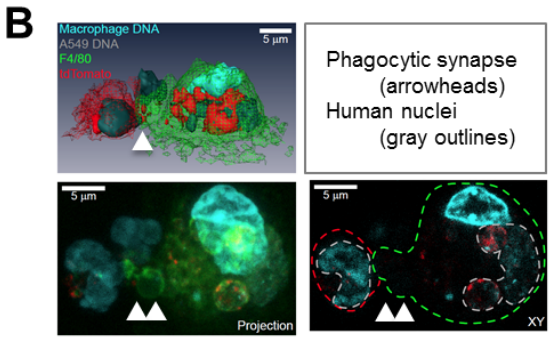

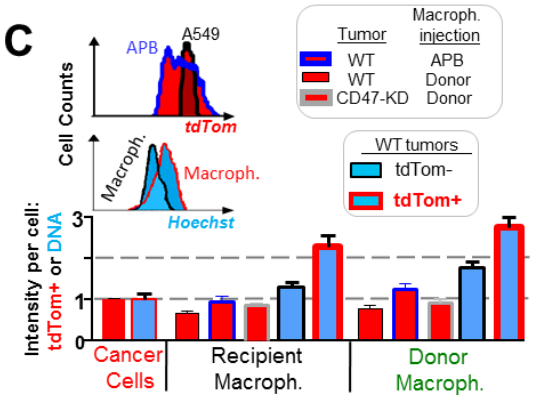

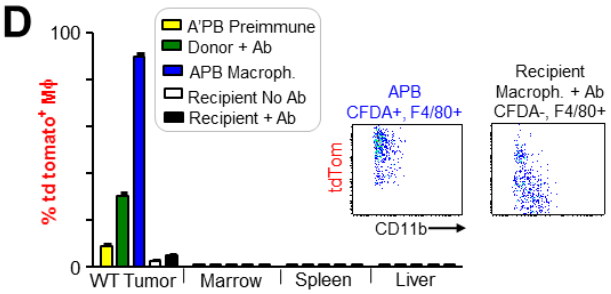

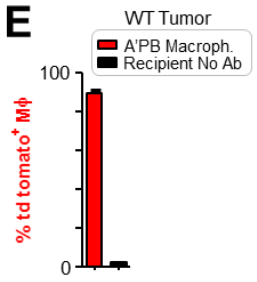

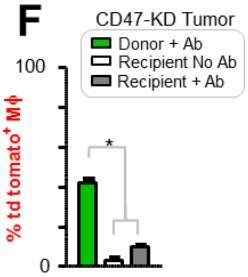

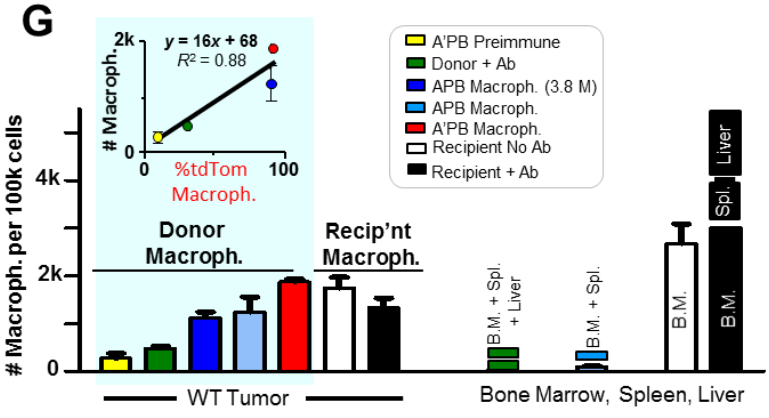

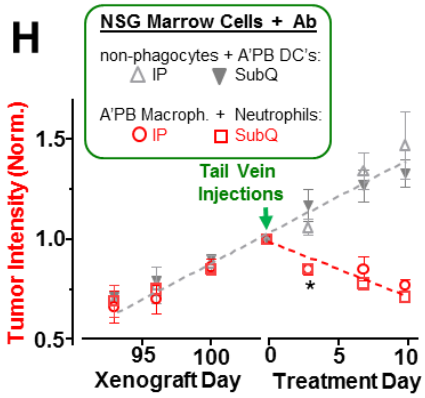

Figure 4.1. *In vivo* tumor phagocytosis and accumulation of engineered donor MΦ's can shrink tumors. (**A**) Schematic of NSG bone marrow harvest, labeling, and transfusion. Bone marrow cells taken from the femur and tibia were labeled with CFDA, their SIRPα receptor inhibited with anti-mSIRPα, Fc receptor loaded with a targeting antibody then tail-vein injected into tumor-bearing NSG mice. In some experiments, instead of preloading Fc receptor, targeting Ab was systemically injected. Recipient mice were given an Ab injection on day-3 and subsequently sacrificed ~3 hour later. Bone marrow, peripheral blood, spleen, liver and tumor tissue were harvested after and analyzed for macrophage eating by flow cytometry. (**B**) 3D reconstruction of a confocal image of a phagocytic macrophage, isolated directly from the tumor. One tdTom A549 tumor cell was completely engulfed inside the macrophage, while two additional A549s remained adherent to the macrophage. (**C**) Quantification of tdTom and Hoechst intensity in $CD11b^+$ $F4/80^+$ macrophages normalized to A549 tumor cells. Ratios not significant from 1 indicate ~1-2 tumor cells per macrophage. ($n \geq 4$ mice per group). (**C, inset**) Representative histograms of tdTom (red shade) and Hoechst (blue shade) intensity distribution. For upper histogram: tdTom positive macrophages (blue outline) and tdTom A549 tumor cells (black outline). Lower histogram: tdTom positive macrophages (red outline) and tdTom negative macrophages (black outline). (**D**) The level of phagocytosis as represented by the percentage of tissue-isolated macrophages with tdTom proteins of A549 tumor cells (n = 4–10 tumors per group). (**D, inset**) Representative flow-cytometry plots of macrophages that are tdTom positive, comparing APB MΦ eating to recipient MΦ eating. (**E**) Measuring A'PB MΦ eating of tumor cells by determining the number of A'PB MΦ that are tdTom positive and comparing it to recipient macrophages. (n = 4-8

mice per group). (**F**) Phagocytosis of CD47 KD^{++} tumor cells with donor cells and recipient TAMs (n = 6; *P<0.05). (**G**) Population count of macrophages per 10^5 cells isolated from tumors and other organs. Mice received 7.5 million monocytes and macrophages unless specified otherwise. (n ≥ 3 mice per group, n.m: not measured). (**G, inset**) Percentage of tdTom positive macrophages from panels B-D vs. number of macrophages per 10^5 cells. (**H**) *In vivo* tumor growth of tdTom A549 subcutaneous tumors treated with two sorted fractions NSG bone marrow. Tumor growth was measured by tdTom intensity. After tail-vein injection of sorted donor cells, mice were tail-vein injected 3 times per week with anti-human Ab. (n ≥ 4 mice per group).

Macrophages *in vitro* engorge and accumulate in 3D

To begin to assess an 'engorge and accumulate' mechanism in which A'PB MΦ eat more and thereby migrate less, antibody-coated beads ranging from 900 nm to 6.7 μm were added to SIRPα inhibited macrophages in culture for 150 minutes and then transferred to 5 μm transwell filters for 24 hours of three-dimensional migration (**Fig. 4.2A**). For beads that were not opsonized, no engulfment occurred, and 32% of SIRPα-inhibited macrophages squeezed through the filter independent of pre-incubation (**Fig. 4.2B**). For any bead size that was opsonized, ~22% of macrophages engulfed beads in the 150 minutes pre-incubation, and this increased ~4-fold after 24 hours of cell culture on the top of the transwell (**Fig. 4.2C**); importantly, migration was suppressed ~10-fold for the 900 nm bead and nearly 100-fold for the largest, 6.7 μm bead (**Fig 4.2B**). An inability to pull a large bead through a small hole (i.e. sterics) likely explains the latter large decrease, but since only two beads or fewer were engulfed per macrophage regardless of size, phagocytosis of even the smallest beads inhibits migration independent of sterics (**Fig. 4.2D**). Furthermore, without the 150 minutes pre-incubation, 5-10% fewer macrophages engulfed beads after the 24 hours on the transwell, and for incubations with 900 nm beads ~5% more macrophages migrated through the transwell compared to just ~1% more for 6.7 μm beads. Macrophages are thus unable to "eat and run" and rather prefer to "eat and stay". This is perhaps because phagocytosis and migration depend on an overlapping set of cytoskeletal proteins as will be discussed. Furthermore, when given the choice between migrating or phagocytosing, MΦ choose the latter when strongly activated.

Cancer cells are large, but flexible and degradable. To assess whether engulfment of such targets could likewise hinder migration of macrophages, the human lung cancer A549 cells in mouse xenografts were disaggregated and compared in *in vitro* phagocytosis to disaggregated lung from the same mouse (lacking cancer cells). Samples were incubated for 24 hours on the tops of transwells with A'PB MΦs. Flow cytometry scatterplots (**Fig. 4.S4**) show macrophages on top of a transwell have higher tdTom intensity and are much larger in size compared to macrophages on the bottom. The large size of macrophages relative to the transwell pores is confirmed by the scale bar in confocal imaging (**Fig. 4.1B**). Consistent with the above experiments using beads, A'PB MΦs mixed with disaggregated tumors resulted in complete inhibition of migration whereas 47% of A'PB MΦs mixed with disaggregated lung tissue migrated (**Fig. 4.S4**). Additional *ex vivo* studies (**Fig. 4.S4**) confirm the higher phagocytic activity of donor cells versus TAMs. The results are consistent with the hypothesis that phagocytic engorgement of cancer cells impedes 3D-migration within tumors to favor donor macrophage accumulation.

Figure 4.2. Phagocytosis inhibits 3D migration

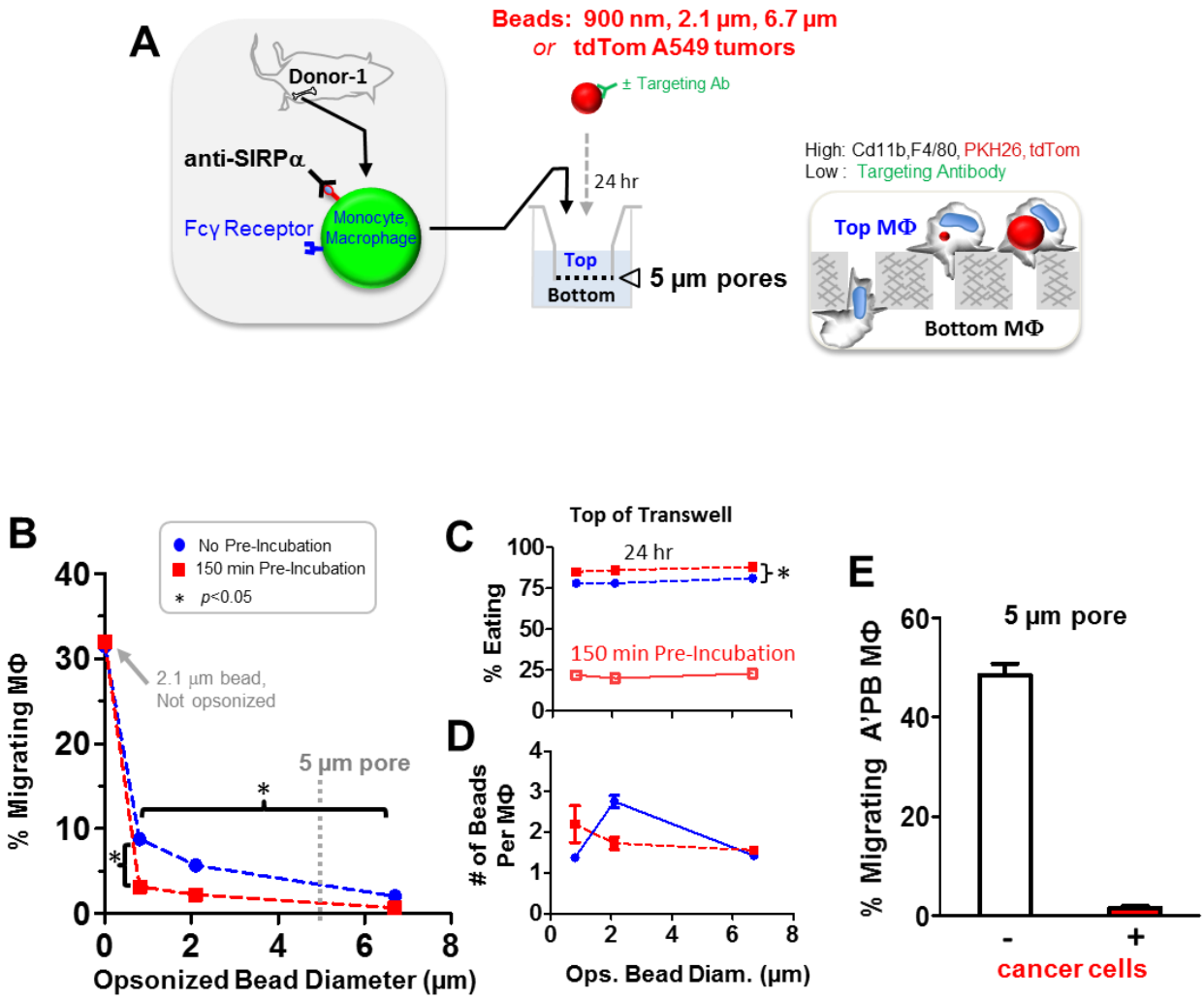

Figure 4.2. Phagocytosis inhibits 3D migration. (**A**) Bone marrow from an NSG donor was engineered and mixed either with beads of diameter 900 nm to 6.7 μm or else with disaggregated tdTom A549 tumors. The streptavidin-coated beads are targeted with anti-streptavidin except for a non-targeted control where anti-SIRPα bound macrophages were plated with 2.1 μm but no anti-streptavidin; for this control, no eating took place. These were cultured together or not in a 150 minutes pre-incubation, and then plated for 24 hours on top of 5 μm pore transwell filters. Cells collected from transwells were stained and analyzed by flow cytometry for CD11b+ F4/80+ MΦ. (**B-D**) The % migrating MΦ was determined from Top and Bottom cell counts, with the non-opsonized control indicated at '0' bead diameter. Migration for this control proves independent of pre-incubation, whereas pre-incubation with the 900 nm bead causes a ~5% decrease in migration. The % Eating indicates internalization of at least one bead in MΦ on top of transwells (or else just after the pre-incubation), and pre-incubation causes ~5-10% more eating. The final plot indicates the number of beads eaten for a given bead size. (n = 3). (**E**) For similar *in vitro* studies of engulfment of disaggregated human lung cancer derived tdTom A549 tumors, the negative control is disaggregated NSG lung. Marrow cells with A'PB MΦ anti-hum were mixed with disaggregated tumor cells or tissue cells at 10:1 ratio. Nearly all A'PB MΦ become tdTom positive and rarely migrate, whereas ~50-fold more of the same A'PB MΦ successfully migrate through the pores when incubated with lung tissue. (n = 3).

Donor MΦ with SIRPα inhibition and primed Fc receptor shrink tumors

Tumor size measurements following tail-vein injection of A'PB MΦ were made from the total tdTom signal from the cancer cells which was also used for the cross-sectional area of the tumor. For the first three days no targeting Ab was injected systemically because A'PB is loaded directly with the targeting antibody. Tumors shrank -25% with anti-hum A'PB and -15% with anti-MUC1 A'PB, but in the same time Cetuximab (anti-EGFR) A'PB and pre-immune A'PB gave similar ~10% tumor growth as untreated tumors (**Fig. 4.3A**). Anti-MUC1 is a mouse IgG that binds very strongly to Fc receptors on mouse MΦ compared to the humanized IgG Cetuximab (**Fig. 4.S2**). Tumor shrinkage is accompanied by decreases in tdTom intensity, which is consistent with phagocytosis and degradation of tdTom protein (**Fig. 4.1C**) on a timescale faster than days (**Fig. 4.S3**). Since the strongly bound targeting Ab on the A'PB is engulfed during eating (**Fig. 4.1B, 4.S3**), supplemental tail-vein injections of targeting Ab began after day-3, with twice per wk injections being typical for multi-week chemotherapy. Untreated and pre-immune treated tumors grew 15-30% larger by day 10 while treated tumors continued to shrink almost linearly, by more than -50% with anti-hum, -38% with anti-MUC1, and -15% with Cetuximab. Binding of Cetuximab to A549 cells is strong after systemic injection (**Fig. 4.S2**), which provides for successful opsonization even though the A'PB lose their weakly associated Cetuximab before or shortly after injection. Anti-MUC1 injections at >10-fold higher doses have been found completely ineffective at treating tumors (Kufe, 2009), which makes the findings here unique. Cetuximab injections at 50-fold higher doses delay growth of A549 tumors by about half (Hsu *et al.*, 2010). For

comparison, paclitaxel treatment of the same tumor model also shrinks almost linearly and to -25% by day 10 (Nair *et al.*, 2016).

To assess the effect of SIRPα inhibition, donor cells lacking SIRPα inhibition were tail-vein injected with systemic anti-hum Ab. Tumor growth was inhibited for 10 days (**Fig. 4.3B, 4.S3**). Subsequent injection of donor cells with SIRPα inhibition (APB MΦ) decreased tumor size and tdTom intensity by -50% over 10 days (**Fig. 4.3B – right half of plots, 4.S3**). Mice treated with donor cells with only a pre-immune Ab continued to grow at the untreated rate. Ab opsonization of cancer cells is thus essential for cancer cell engulfment *in vivo*, and anti-SIRPα synergizes.

Figure 4.3. SIRPα inhibition on donor macrophages enhances tumor shrinkage while tumor associated macrophages selectively clear only CD47 knockdown tumor cells in WT/CD47 KD mosaic tumors

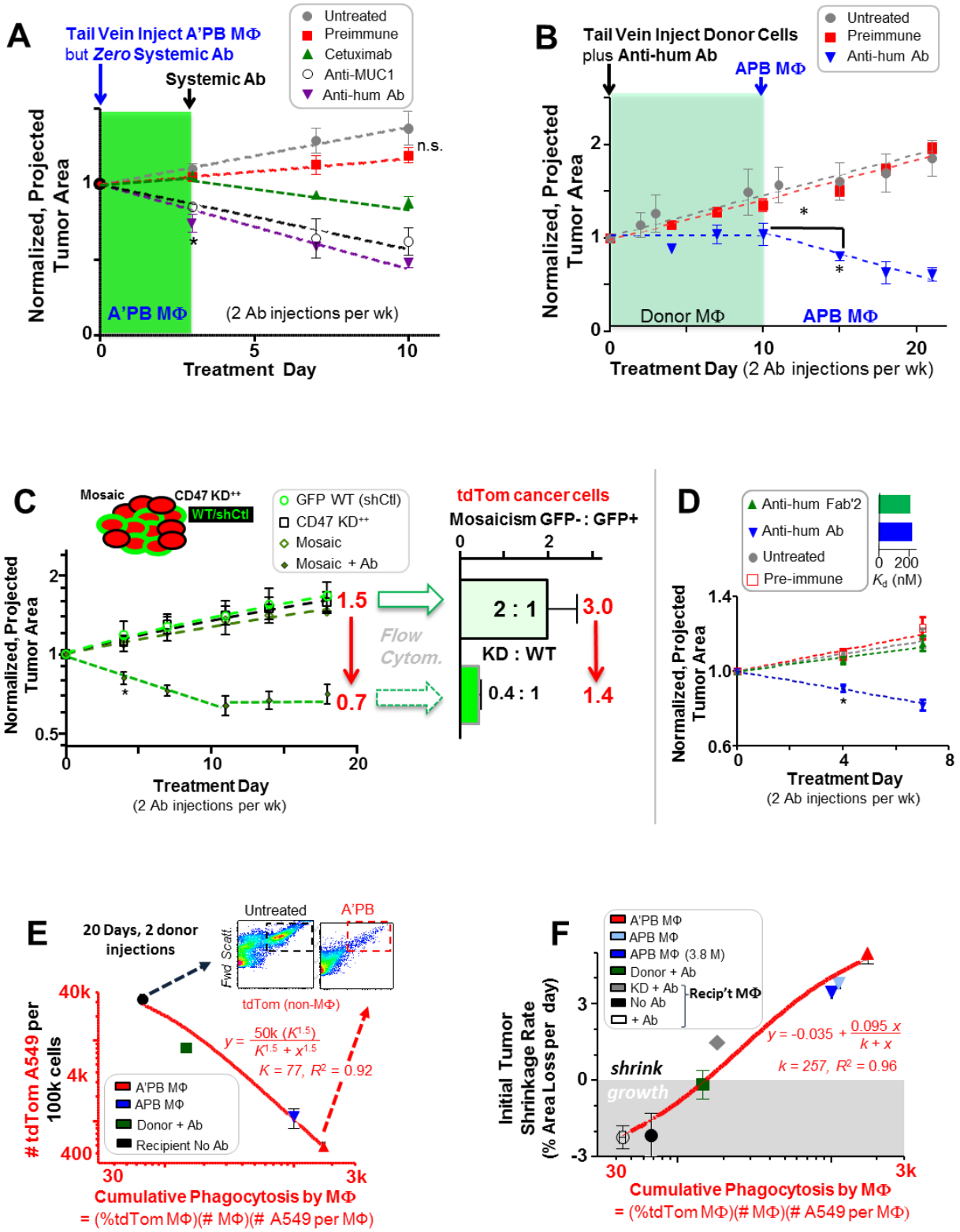

Figure 4.3. SIRPα inhibition on donor macrophages enhances tumor shrinkage while tumor associated macrophages selectively clear only CD47 knockdown tumor cells in WT/CD47 KD mosaic tumors. *In vivo* growth curve of subcutaneous tdTom A549 tumors treated with either A'PB MΦ in the absent of systemic Ab treatment (**A**) or marrow donor cells in presence of systemic Ab treatment (**B**) (n = 3-6 mice per group, **p*<0.05). Tumor growth was measured by projected tumor area (**C-left**). Treatment of mosaic tumors with a ratio of 2:1 WT:CD47 KD tumor cells, with 600 μg anti-human twice a week. Dashed lines are the corresponding linear fits with R^2>0.97. Dashed line is fit of average of final three points each of which are insignificant from day 15. (* *P*<0.05, compared to previous data point, within a treatment arm (n = 4-8). (**C-Right**) Ratio of GFP^-:GFP^+ as determined by flow cytometry following removal of tumors from sacrificed mice (n = 4-9). Day 0 was measured using cells reserved from xeno-transplantation. (**D**) *In vivo* growth curve of CD47 KD^+ "deep knockdown" measure by cross-section tumor are (n ≥ 3 mice per group). (**D, inset**) Bar graph of anti-hum and anti-hum F(ab'2) binding constant (K_d) for A549s (n = 3). (**E**) TdTom A549 depletion from tumors as a function of cumulative phagocytosis by macrophages after two treatments of donor cells (n = 4-8). (**E, inset**) Representative flow cytometry plots of tdTom A549 abundance in untreated tumors (left plot) and treated tumor (right plot). (**F**) Correlating tumor shrinkage measured by cross-sectional tumor area to cumulative phagocytosis in donor and recipient macrophages (n = 4-8 mice per group). Analysis was done on mice injected with 7.5 million monocytes and macrophages unless specified.

Tumor Associated Macrophages (TAMs) can only shrink CD47 knockdown tumors

Our *in vitro* and *in vivo* studies indicated TAMs were minimally phagocytic toward wildtype tumors (**Fig. 4.1B**) but could engulf cancer cells after CD47 knockdown (**Fig. 4.1D, 4.1E**). Mosaic tumors were therefore generated with ~2:1 control cells (sh-Control) that express GFP (**Fig. 4.S4, Table 4.S3**). No significant difference in tumor growth rate was observed between Mosaic, WT/shCtl and CD47 KD tumors for moderate knockdown (**Fig. 4.3C, 4.S4**). Deep knockdown of CD47 did, however, increase tumor growth (**Fig. 4.S4**). The result hints at re-programming (Kaur *et al.*, 2013) and the potential dangers of knockdown therapies (Wang *et al.*, 2013). Tail-vein injection of anti-hum Ab was sufficient to shrink mosaic tumors to a small, stable size with tumor sizes for (untreated / treated) = (1.5 / 0.7) = 2.1 at day-18. To determine which cancer cells were engulfed, tumors were again analyzed by flow cytometry. Untreated tumors averaged 2:1 KD : WT (as GFP:GFP^+) versus treated tumors 0.4:1 KD:WT. The change in ratio agrees with the *in vivo* imaging results: for every 3 cancer cells in untreated tumors, only 1.4 are present after treatment, i.e. (3 / 1.4) = 2.1. The results thus show KD cancer cells are selectively engulfed (5-fold more) compared to WT.

The Fc part of a targeting Ab should bind Fc receptors on macrophages (**Fig. 4.S2, 4.S3**) and thereby activate phagocytosis, even though some IgG such as P84 show very weak affinity as noted. Calreticulin opsonization of cancer cells has also been proposed as contributing to macrophage-driven tumor shrinkage upon CD47 inhibition (Chao *et al.*, 2010; Feng *et al.*, 2015; Gardai *et al.*, 2005). To directly assess the Fc-driven pathway, the Fc fragment was cleaved off anti-hum Ab to generate a F(ab')2 with similar binding affinity as the intact Ab (**Fig. 4.3D inset**). Neither F(ab')2 nor the pre-immune Ab affected

growth of CD47 knockdown tumors (**Fig. 4.3D**). The result is consistent with a key role for Fc receptor activation and indicates binding of anti-hum Ab alone has no anti-tumor effect.

Treatment of WT/shCtl tumors and KD tumors with varying doses of anti-hum Ab could provide more definitive evidence that anti-hum Ab shrinks only KD cells. WT tumors and KD tumors grow at similar rates over 10 wks (**Fig. 4.S4**), consistent with the mosaic tumors. Tail-vein injected anti-hum Ab with dose escalation showed no effect on WT tumors, but caused CD47 KD tumors to shrink 30% over three weeks (**Fig. 4.S4**). When anti-hum Ab treatment was stopped, tumors re-grew at a rate similar to pre-treatment. After 25 days of re-growth, tail-vein injection of more Ab once again caused tumor shrinkage, and at rates similar to the first round of treatment.

Engorge and Accumulate as a mechanism for tumor shrinkage

A "cumulative phagocytosis index" is obtained by multiplying the percentage of tdTom+ macrophages (**Fig. 4.1E-F**) by the number of macrophages in the tumor (**Fig. 4.1G**) and by the number of cancer cells engulfed per macrophage (**Fig. 4.1B,C**). Consistent with expectations, the number of tdTom A549 cells (per 10^5 total cells) that remain in the tumor decreases when plotted versus cumulative phagocytosis by the different macrophages (**Fig. 4.3E**). Untreated tumors consist of ~40% cancer cells (**Fig. 4.3E, left scatterplot**), whereas A'PB MΦ treatment decreases cancer cell numbers by ~100-fold (**Fig. 4.3E, right scatterplot**). Such selective clearance of the tdTom cancer cells is not only consistent with the specific engulfment in mosaic tumors with CD47 knockdown cancer cells (**Fig. 4.3C**) but also with overall shrinkage of WT tumors by

engineered donor MΦ (**Fig. 4.3A, B**). Tumor shrinkage rate also increases with cumulative phagocytosis when determined for all the different macrophage types injected into mice with WT and with CD47-KD tumors (**Fig. 4.3F**). Tumor growth equates to a negative shrinkage rate, even though tumor cells remain at 40%. Treatments that relied on TAMs are all in the lower half of this plot, even with CD47 inhibition.

To begin to clarify some of the differences between donor MΦ and recipient TAMs, tumors were isolated 3 hours after treatment and stained for the so-called M1-marker major histocompatibility complex II (Murdoch *et al.*, 2008) as a 'phagocytic phenotype' (Ramachandra *et al.*, 1999), and also the M2-marker mannose receptor (Mantovani *et al.*, 2002) (MRC1 or CD206) indicating a relatively non-phagocytic phenotype (Mantovani *et al.*, 1992). Recipient TAMs that were tdTom negative had a comparatively low M1/M2 ratio as were macrophages in spleen or liver, whereas recipient TAMs that had engulfed cancer cells (becoming tdTom) positive showed a higher M1/M2 ratio (**Table 4.1 last column**). Fresh marrow-derived MΦ as well as tumor-extracted donor and APB MΦ always showed the highest M1/M2 ratio regardless of whether an internalized cancer cell was evident. High MHCII expression by DCs (and perhaps MΦ also) increases their migration, enhancing presentation and activation of T cells and B cells (Faure-André *et al.*, 2008).

Table 4.1. M1 and M2 analysis of macrophages

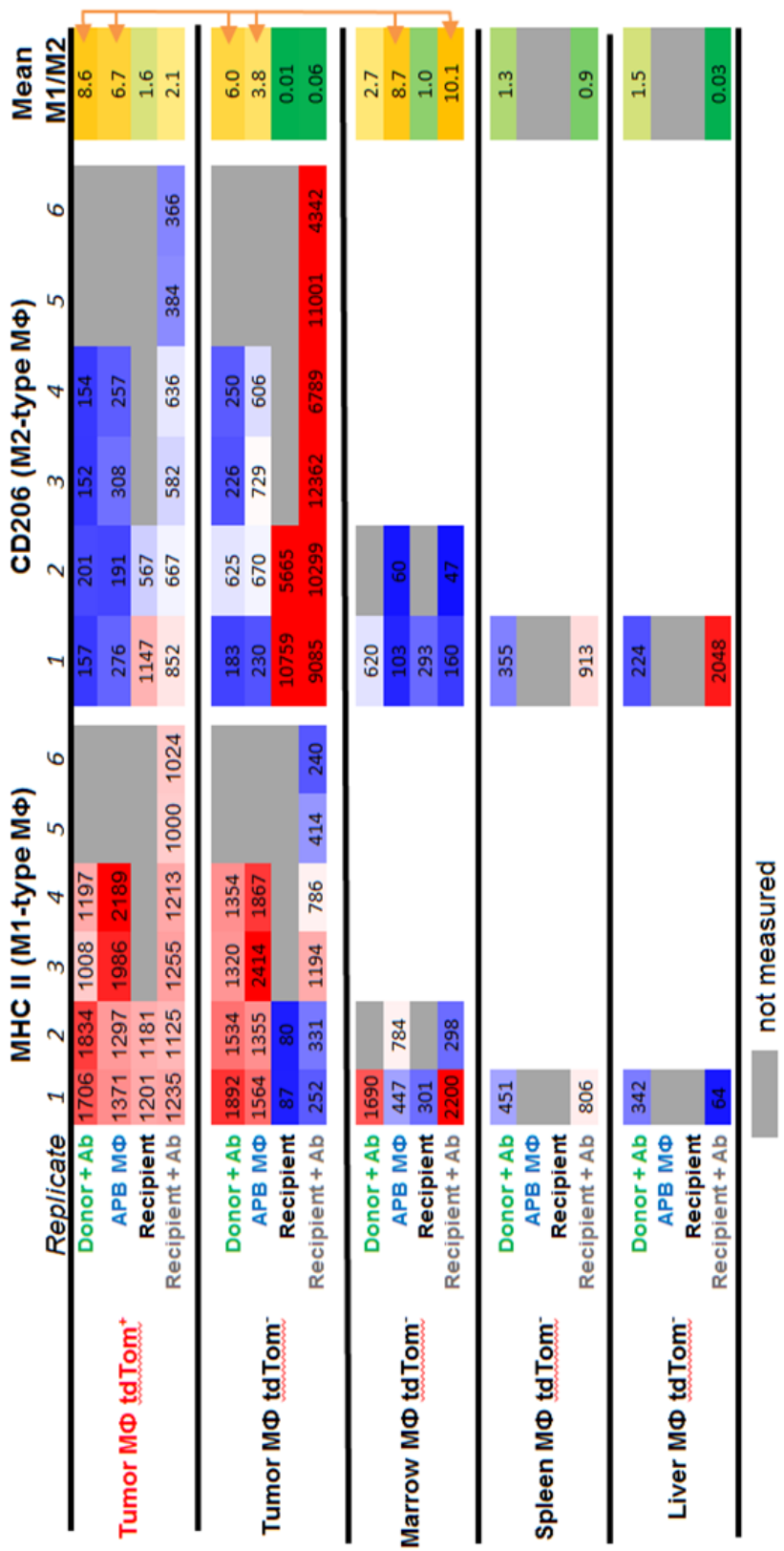

Table 4.1. M1 and M2 analysis of macrophages. Donor and recipient macrophages isolated from different tissues were stained for M1 (MHC II) and M2 (CD206) markers. Donor cells, regardless of SIRPα inhibition, had a high M1 to M2 ratio as did marrow macrophages. Recipient macrophages from the tumor were split depending if they were tdTom positive (M1) or negative (M2).

Donor MΦ in Tumors differ from Marrow MΦ and also TAMs that have highest SIRPα

Macrophage phenotype depends strongly on microenvironment and is not adequately described by a few surface markers (Lavin *et al.*, 2014) (**Fig. 4.4A**). RNA-Seq was done on marrow macrophages and tumor-extracted donor MΦ (tdTom+) as well as splenic MΦ and TAMs (tdTom+ or tdTom-). Although a small set of MΦ surface markers were used to sort cells, marrow and spleen MΦ still cluster with published profiles (**Table 4.S4**). Hierarchical clustering shows donor MΦ from day 2 cluster with all tissue macrophages and are completely distinct from marrow MΦ (**Fig. 4.4B**). At day 3, these MΦ cluster even closer to TAMs. Although recent reports have suggested CD47 blockade causes TAMs to polarize to the M1 phenotype (Zhang *et al.*, 2016), the donor MΦ begin to differentiate within days of accumulating in a new tissue, skewing toward non-phagocytic TAMs.

Among transcripts most relevant to phagocytic activity, *Sirpa* increased 8-fold with decreasing phagocytic phenotype. Fresh marrow-derived MΦ had the lowest *Sirpa*, donor MΦ in tumors had intermediate *Sirpa* similar to splenic MΦ, and TAMs had the highest *Sirpa* (**Fig. 4.4C**). *Cd47* varies little between the different MΦ. Flow cytometry for surface protein confirmed the trend for mSIRPα with Marrow < Spleen < TAMs, whereas mCD47 did not vary (**Fig. 4.4D**), with mSIRPα protein on day-3 donor MΦ increasing slightly from marrow (**Fig. 4.S5**). High mSIRPα will tend to increase the sensitivity to cells expressing even low levels of CD47 and will therefore tend to passivate MΦ, just as inhibiting SIRPα (or knocking down CD47) does the opposite in favoring phagocytosis. The increased mSIRPα on donor MΦ relative to marrow MΦ also equals

or exceeds the loss of anti-SIRPα inhibiting antibody with dissociation in the tumor (**Fig. 4.S1, 4.S5**). Unfortunately, this data doesn't establish a causal relationship between increased SIRPα and donor MΦ differentiation into TAMs as M2 markers and SIRPα increase concurrently. RNA analysis of donor MΦ at early time points is needed for such conclusions. Nonetheless, differentiation toward DCs is unlikely since DC markers *Cd135* and *Cd86* are very low in marrow MΦ (consistent with ~1 DC per 50 MΦ in marrow) and these markers remain low after accumulation in tumors (**Table 4.S4**). Consistent with an effect of MΦ differentiation and with the Hoechst staining of DNA in phagocytosis studies (**Fig. 4.1C**), marrow MΦ exhibit higher Hoechst staining than TAMs.

By aligning RNA-Seq data with the human transcriptome (rather than mouse), we find human RNA is most abundant in donor MΦ taken from tumors, which is consistent with phagocytosis of human cancer cells (**Table 4.2**). This might be the first time that engulfed-target RNA has been separated from MΦ RNA, and suggests that past profiling of MΦ [eg. (Lavin *et al.*, 2014)] has more complexity than usually assumed. For the fresh marrow and spleen MΦ, a mouse : human alignment ratio of ~8:1 is inverted to ~1:7 for donor MΦ taken from tumors. Whereas MΦ markers are dominated by mouse sequence reads in all samples, epithelial markers (E-cadherin, keratin-18) that are typical of a lung cancer line are human and detected only in tumor MΦ, both donor MΦ and TAMs. The results provide novel, additional evidence of tumor engulfment.

Microenvironments of solid tumor are highly collagenous and very different from the soft, low matrix microenvironment in marrow (Egeblad, Rasch, & Weaver, 2010). Differentiation might therefore be expected for marrow-derived MΦ that engorge on cancer cells and accumulate in solid tumors. Among the transcripts that increased the most

were those for collagen-1 (**Table 4.2**), which is a heterotrimer (of Col1a1 and Col1a2) that self-assembles into fibers that determine the solidity of tissue (Swift *et al.*, 2013). Matrix stiffness often alters cell phenotype (Engler *et al.*, 2006) and can affect phagocytosis (Patel *et al.*, 2012), with one intriguing mechanosensor being the nuclear structure protein lamin-A (Swift *et al.*, 2013a). *Lmna* is indeed highest in donor MΦ from the solid tumors here (**Table 4.2**). Combining our transcriptome results with those of others from many other tissues (Lavin *et al.*, 2014) reveals a consistent increase in *Lamin-A : Lamin-B* versus tissue or tumor solidity measured as micro-stiffness (**Fig. 4.S5**). Lamin-B isoforms are relatively constant compared to the increased collagen with tissue solidity (Swift *et al.*, 2013). Importantly, profiling shows *Sirpa : Cd47* also increases with tissue or tumor stiffness (**Fig. 4.4E**).

For human-derived THP1 macrophages adhering *in vitro* either to a gel that is soft like marrow or a gel that is much stiffer like a tumor, protein increases are evident in both lamin-A : lamin-B and in SIRPα (**Fig. 4.4F, 4.S5**). The latter has functional implications because both anti-human-SIRPα inhibition and RNAi knockdown of SIRPα increase whole-cell engulfment of opsonized A549 cancer cells *in vitro* just as effectively as CD47 inhibition on these cancer cells (**Fig. 4.S7**). Importantly, the anti-human-SIRPα Ab is distinct from the P84 clone anti-mSIRPα used on mouse-derived MΦ, and illustrates a possible generality to the approach.

Figure 4.4. Phenotype difference of phagocytic and non-phagocytic cells is attributed to SIRPα expression

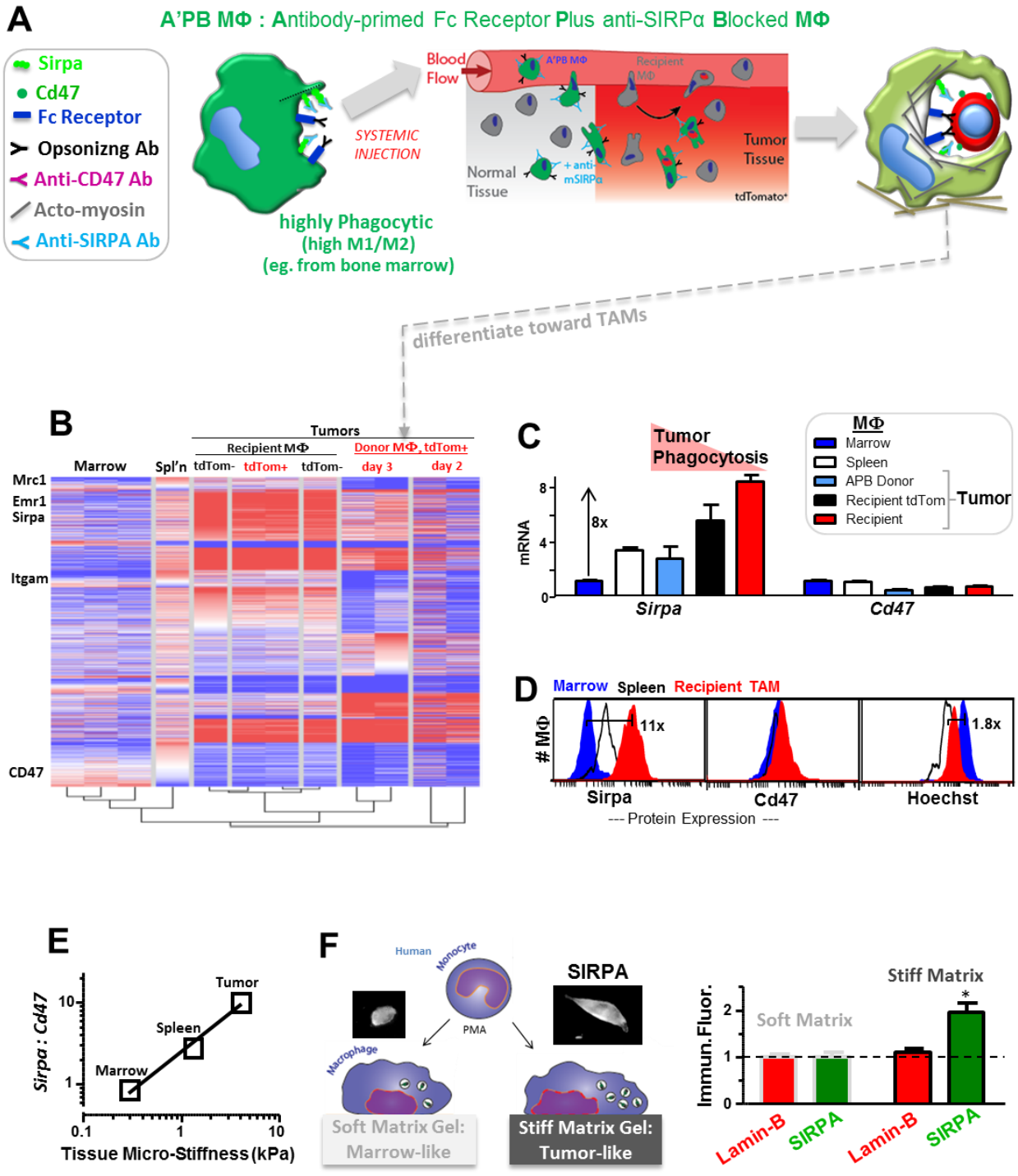

Figure 4.4. Phenotype difference of phagocytic and non-phagocytic cells is attributed to SIRPα expression. (**A**) Antibody modification (blocking SIRPα and loading Fc receptor with targeting antibody) of marrow macrophages followed by injection into circulation leads to A'PB MΦs to migrate into tumors, phagocytose cancer cells, and become immobilized. Extended expose to the tumor microenvironment could lead to differentiation of A'PB MΦs into TAMs. (**B**) Euclidian clustering analysis of RNA sequencing data generated from macrophages of different tissues. Macrophages isolated from tumors were further separated by their tdTom positivity. (isolation across 4 NSG mice, $>8\times10^6$ reads for each group). (**C**) Quantification of RNA expression of *Sirpa* and *Cd47* taken from RNA-seq data. Quantification was done by taking mRNA expression of *Sirpa* (which was the sum of 2 variants) and *Cd47* (1 variant) and normalizing to the number of total mouse reads in each macrophage sample. (**D**) Quantification of Sirpa and Cd47 protein expression in macrophages verify mRNA expression (n = 2 mice). Displayed are representative histograms of fluorescent intensities from proteins expressed in macrophages isolated from the tumor, marrow, and spleen. (**E**) *Sirpa:Cd47* ratios also increases in macrophages with increasing microenvironment stiffness. (**F**) *In vitro* experiment using PMA differentiating THP-1s on different matrix stiffness, (soft-marrow and stiff-tumor). After 7 days of culturing, THP-1s were fixed and stained for Lamin-B, and SIRPα. Fluorescent intensity for each protein was normalized to the soft condition. Lamin-B remained unchanged while SIRPα significantly increased (n = 3, *$P<0.05$).

Table 4.2. Donor macrophage mRNA contains an abundance of human RNA and expresses high levels of RNA encoding for matrix proteins

			Marrow			Spl'n	Tumor Recipient Macroph.				Tumor Donor Macroph. tdTom+					
							tdTom-			tdTom+			Day 3		Day 2	
	Alignment	Mouse	6,926,756	7,476,674	10,261,048	6,538,074	11,137,616	9,259,021	11,739,145	12,063,915	1,181,922	1,703,284	887,666	1,399,347		
		Human	868,990	976,741	1,160,386	928,823	1,708,901	2,258,749	1,868,961	3,792,741	8,745,187	9,845,916	4,002,987	15,347,188		
		Total	7,795,746	8,453,415	11,421,434	7,466,897	12,846,517	11,517,770	13,608,106	15,856,656	9,927,109	11,549,200	4,890,653	16,746,535		
Macroph. markers	*Sirpa*	Mouse	169	188	211	596	1349	1,238	1,536	1,410	272	690	301	154		
		Human	21	25	50	74	123	75	119	62	9	17	6	11		
	Cd47	Mouse	535	699	718	614	528	388	414	432	167	344	312	157		
		Human	150	125	211	172	110	52	81	80	133	41	41	82		
	Itgam	Mouse	256	279	363	113	383	207	314	303	53	65	0	68		
		Human	6	4	9	3	9	4	6	3	5	5	4	2		
	Emr1	Mouse	63	65	56	554	1326	1,112	1,420	1,229	286	302	1076	70		
		Human	12	7	4	52	94	67	96	43	9	2	3	0		
	Mrc1	Mouse	61	44	36	207	345	269	177	100	39	14	2	0		
		Human	0	0	0	0	0	0	1	0	0	0	0	0		
Epith. markers	*Ciita*	Mouse	3	12	8	120	32	25	21	37	0	1	0	19		
		Human	0	0	0	1	1	0	0	0	0	0	0	0		
	CDH1	Mouse	0	2	0	0	0	0	3	3	0	0	0	8		
		Human	0	0	0	0	16	62	7	65	35	48	93	137		
	KRT18	Mouse	0	0	3	0	4	12	3	29	536	733	742	1629		
		Human	2	1	9	0	697	1,588	399	2,469	1,972	3,386	4622	3874		
Matrix to Nucleus pathway	*Col1a1*	Mouse	6	1	0	0	5	90	103	4	1,679	3,080	1200	920		
		Human	8	1	0	0	10	102	172	7	87	150	72	21		
	Col1a2	Mouse	0	16	0	0	5	130	76	17	1,613	2,263	1092	938		
		Human	0	16	0	0	1	37	34	5	18	29	21	8		
	Acta2	Mouse	1	3	4	4	20	87	6	51	925	681	955	915		
		Human	6	16	17	15	32	86	9	38	20	18	60	12		
	Lmna	Mouse	107	102	10	46	125	98	135	119	1,180	906	1033	953		
		Human	185	145	24	71	247	180	268	313	595	487	768	344		
	Lmnb1	Mouse	45	85	89	33	14	33	11	16	9	70	0	0		
		Human	54	120	135	52	20	21	10	14	4	10	0	0		

Table 4.2. Donor macrophage mRNA contains an abundance of human RNA and expresses high levels of RNA encoding for matrix proteins. RNA isolated from Figure 4B was realigned to human sequences. **top row**: comparison of the total number of reads from each sample between mouse and human alignments; **MΦ markers**: protein markers used to identify macrophages have low human alignment and high mouse alignment; **epithelial makers**: only macrophages in the tumor have high mRNA reads for human E-cadherin and keratin with donor MΦ having the highest; **matrix to nucleus pathway**: donor MΦ have a significant amount of mRNA that aligns to mouse matrix mRNA compared to non-tumor macrophages and even TAMs.

Plateaus in shrinkage are corrected by multiple injections of mouse or human donor MΦ

A plateau in tumor shrinkage for both subcutaneous and IP tumors that had been apparent from day-9 to day-13 (**Fig. 4.S2**) suggested either donor MΦ differentiation or perhaps tumor resistance (eg. loss of epitopes). In a longer duration study, injection of anti-hum Ab plus APB MΦ caused 20% shrinkage by day 3 (**Fig. 4.5A**) but reached only 40% by day 10 with a plateau up to day 14, despite Ab injections. Untreated tumors follow linear growth in terms of both projected area and tdTom intensity, and no effect was seen with pre-immune Ab plus APB MΦ (i.e. SIRPα inhibited). On day 14, a second injection of APB MΦ produced a rapid decrease in tumor size and tdTom intensity (**Fig. 4.5A**) as did first injection into the pre-immune controls. Systemic injections of anti-hum Ab stopped at day 24, and tumors stopped shrinking until a cell treatment at day 35, at which time tumors shrank once again. Plateaus suggest a loss of function of donor MΦ.

Fresh marrow MΦ from a diverse pool of human donors (**Table 4.S5**) were engineered with a human-specific anti-hSIRPα (**Fig. 4.5B**), before tail vein injections of cells (~12M). Tumors shrunk within days after human APB and A'PB MΦ treatments, decreasing by ~40% within the first week (**Fig. 4.5B**) – similar to mouse donor results (**Fig. 4.5A**). No significant effects resulted from pre-immune injections combined with either APB MΦ or human donor MΦs lacking anti-hSIRPα (**Fig. 4.5B**). However, human donor injection with anti-hum Ab (and no SIRPα inhibition) did shrink tumors to a small extent (**Fig. 4.5B**), which is a slightly more positive effect than analogous treatments with mouse marrow which stop growth (**Fig. 4.3B**). Flow cytometry analyses of the $CD14^+$ $CD33^+$ $CD66b^-$ human MΦ isolated from tumors showed human MΦs are larger than

mouse MΦ, and each typically engulfs two to three tdTom cancer cells (**Fig. 4.S6**). This exceeds the ~1:1 result for mouse MΦ : human cancer (**Fig. 4.1B,C**) and indicates more human engorgement of more human cancer cells and more accumulation to cause greater tumor shrinkage as observed and expected (**Fig. 4.3F**).

Beyond the initial phases of tumor shrinkage following treatment, plateaus in tumor size were again evident by ~day 15 despite continuous biweekly injections of anti-hum Ab. No significant tumor growth was measured up to 55 days after donor cell injection but shrinkage could be re-initiated with additional injections of human donor cells. Sustained breaks in treatment with mouse marrow MΦ also led to periods of no regrowth. Eventually tumors re-grow at rates approximating those of untreated tumors occurred (**Fig. 4.S6**). Human marrow MΦ injections thus cause similar tumor shrinkage and have similar limits as injections of APB and A'PB mouse MΦ.

Tumors with CD47 KD were treated with hAPB MΦ or with human donor cells, both with anti-hum Ab, to assess whether hSIRPα inhibition on human donor MΦ could be as effective as inhibiting CD47. Treated tumors shrunk at the same rate, consistent with SIRPα inhibition equating to CD47 inhibition (**Fig. 4.S6**). As with treatment by engineered mouse marrow MΦ, the engineered human marrow MΦ shrink tumors significantly more effectively than TAMs, with 12% tumor shrinkage per day versus 2%, respectively.

Figure 4.5. Single and multiple injections of mouse and human A'PB or APB MΦ cause rapid shrinkage of subcutaneous and intraperitoneal tumors

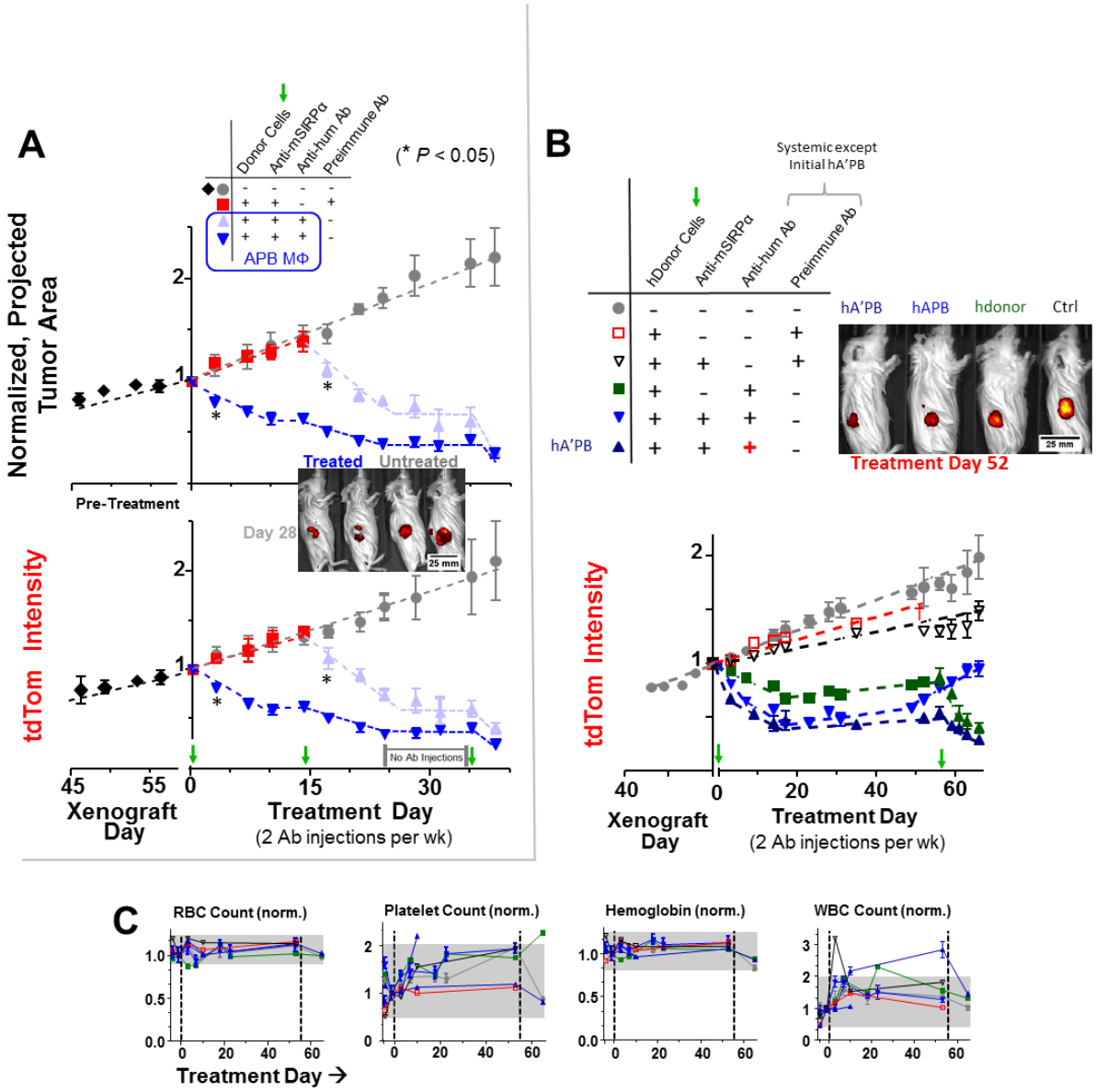

Figure 4.5. Single and multiple injections of mouse and human A'PB or APB MΦ cause rapid shrinkage of subcutaneous and intraperitoneal tumors. (**A**) *In vivo* growth curve of tdTom A549 tumor measured by cross sectional tumor area (upper) and tdTom intensity (lower). Mice were given biweekly antibody treatment and donor marrow on day 0, 14, and 35. Mice in pre-immune treatment group were switch to full treatment group on day 14 due to tumor burden. Approximately 10 million donor marrow cells were injected per mouse (n = 4-8 mice per group). (**A, inset**) Tumor imaging on treatment day 28 after two full donor marrow treatment cycles. Red regions are tdTom signal acquired from tumors. Two mice (left) were treated with APB macrophage and the other two mice (right) were untreated. (**B**) Treatment of tdTom A549 subcutaneous tumors that grew for 60 days with engineered human marrow. *In vivo* growth curve measure by tdTom intensity (n = 16 mice for each group). All tumors treated with human marrow + anti-hum reduced in size, but SIRPα inhibition further increased rate of shrinkage. Mice that received hA'PB MΦ with a nonspecific antibody all continued to grow similar to untreated ($n \geq 4$ mice per group). (**B, inset**) Representative tdTom images of treated and untreated mice on day 52 of treatment. Mice are arranged by treatment effectiveness with hA'PB > hAPB > hdonor > ctrl. (**C**) Blood profiles of all mice before and after treatment. Gray area shows the pretreatment and untreated variance in blood profiles (normal range). All treated mice remain in the normal during the 60 days of multiple engineered human donor treatment.

Blood profiles remain normal with engineered marrow treatments of tumors

Safety is a concern whenever inhibiting MΦ recognition of 'self' based on past findings that systemic injection of anti-CD47 rapidly clears blood cells (Weiskopf, Ring, Ho, Volkmer, Levin, Volkmer, Ozkan, *et al.*, 2013b; Willingham *et al.*, 2012) and that *Cd47*-knockout mice (NOD strain) exhibit auto-immunity, anemia, and premature death (Per-Ame Oldenborg *et al.*, 2002). Blood was therefore drawn periodically from the various mice before and after MΦ injections (**Fig. 4.5C, 4.S6**), and RBC count, hemoglobin levels, percent hematocrit, platelet count, and WBC count all remained within the normal range for all treated mice over the ~ 9 wk experiment (**Fig. 4.5C**). For all mice, a slight upward increase in WBC count was seen and could reflect inflammation associated with retro orbital bleeds (Nemzek, Bolgos, Williams, & Remick, 2001). Furthermore, no anomalous mouse behavior or Graft versus Host Disease (GvHD) was observed in any mouse treated with engineered human or mouse marrow after multiple injections of each over 30+ days of experimentation in 30+ mice. Intravenous injection of engineered donor MΦ thus appears safe during rapid and effective regression of solid tumors.

4.4 DISCUSSSION

For the dozens of conditions studied, the extent of MΦ phagocytosis of tumor cells *in vivo* as measured at the single cell level predicts initial rates of tumor shrinkage or growth (**Fig. 4.3E-F, 4.S2**). At least three features of a MΦ might therefore be optimized for efficient engulfment of cancer cells *in vivo*. First, the phagocytic potential must be considered: marrow MΦ – whether sorted or not from marrow (**Fig. 4.1H**) – can clearly be effective compared to TAMs (**Fig. 4.1D**). Second, CD47-SIRPα self-recognition should be inhibited; anti-SIRPα antibodies can enhance phagocytosis of opsonized targets by immobilizing SIRPα (by crosslinking *cis* homodimers (Lee *et al.*, 2010)) and thereby limiting SIRPα accumulation into the phagocytic synapse (**Fig. 4.S1**). The immunological synapse between an antigen-presenting cell and a T-cell also depends on molecular segregation for signaling. Third, the cancer cell should be specifically opsonized as illustrated here with both pre-loaded targeting Ab's and with systemic injections. A single antibody, such as anti-CD47, has been proposed to both inhibit 'self' signaling and to also efficiently opsonize a cancer cell (Willingham *et al.*, 2012), but this has become a subject of concern in terms of replication and statistical significance (Horrigan *et al.*, 2017).

Phagocytes are often considered highly motile, but inhibition of cell migration by the engulfment process could explain cell accumulation. MΦ derived from mouse marrow (NSG) or human marrow clearly infiltrate large solid tumors, and the MΦ accumulate in proportion to engulfment (**Fig. 4.1B-F, 4.S6**). With solid tumors of low porosity, immobilization can in part be due to an inability to 'eat and run' since engulfment of two nanobeads significantly reduced 3D migration through much larger micro-pores (**Fig. 4.2B-E**). Antagonism is already known between endocytic and migratory pathways for

very primitive cells such as Dyctiostilium amoeba (Veltman *et al.*, 2014) and fly haemocytes (Evans *et al.*, 2013) as well as dendritic cells (Chabaud *et al.*, 2015). Overlapping mechanisms in MΦ require further study, but competition is likely between pathways involving shared cytoskeleton components such as ARP2/3 or Myosin II. Nuclear lamins set nuclear stiffness, and a cell with high lamin levels (eg. **Fig. 4.S5**) is already known to be physically impeded in 3D migration (Shin *et al.*, 2013; Thiam *et al.*, 2016) as will engulfment of another cell with a stiff nucleus (**Fig. 4.1B,C**). The resulting engorge and accumulate mechanism for engineered donor MΦ in solid tumors also minimizes accumulation in other tissues (**Fig. 4.1G, 4.S3**).

No detectable impact on mouse health resulted from the cell + Ab injections that drive tumor phagocytosis and shrinkage (**Fig. 4.5C, 4.S6**). In comparison, systemic injection of anti-CD47 causes large decreases in blood cells and platelets (Oldenborg *et al.*, 2002; Weiskopf *et al.*, 2013; Willingham *et al.*, 2012), which reflects CD47's ubiquitous expression. Careful attention to species specificity of anti-CD47 is of course needed in such studies (Subramanian *et al.*, 2006; Tsai & Discher, 2008), but CD47 blockade in a clinical setting is expected to sensitize all healthy cells to phagocytosis by MΦ. Combinations of systemic anti-CD47 with tumor opsonizing antibodies nonetheless engage a small number of phagocytic TAMs (confirmed here in **Fig. 4.1F,** with quantitation of tumor cell uptake), and our CD47 knockdown studies document selective eating of cells with low CD47, enriching for CD47-high cancer cells (**Fig. 4.3C-D, 4.S4**). This can explain why cancer patients have CD47-high cancer cells (Willingham *et al.*, 2012).

For the infiltrating engineered macrophages studied here, microenvironment stiffness of tumors likely contributes to their eventual differentiation, which includes upregulation of SIRPα (**Fig. 4.4B-F, 4.S5**) that provides more opportunity to bind 'marker of self' CD47. Although RNAi knockdown of SIRPα can also increase phagocytosis of Ab-opsonized cells *in vitro* (**Fig. 4.S5**), SIRPα-knockdown macrophages can promote tumor growth *in vivo* (Pan *et al.*, 2013) – perhaps related to differentiation. Phagocytosis by differentiating donor MΦ here is expected to be gradually suppressed, consistent with observations from donor MΦ RNA-Seq that upregulation of SIRPα and M1/M2 markers occur simultaneously. Subsequent injections of marrow cells remain effective and safe (**Fig. 4.5C, 4.S6**), noting that multiple injections of marrow and leukocytes are already done in the clinic (Eapen *et al.*, 2004). The findings here thus provide insight into mechanisms, utility, and safety of engineering: (*i*) a highly phagocytic and motile macrophage, with (*ii*) inhibition of 'self' signaling by anti-SIRPα, combined with (*iii*) robust target opsonization.

4.5 SUPPLEMENT

Figure 4.S1. P84 SIRPα antibody binds to NSG macrophages and immobilizes SIRPα

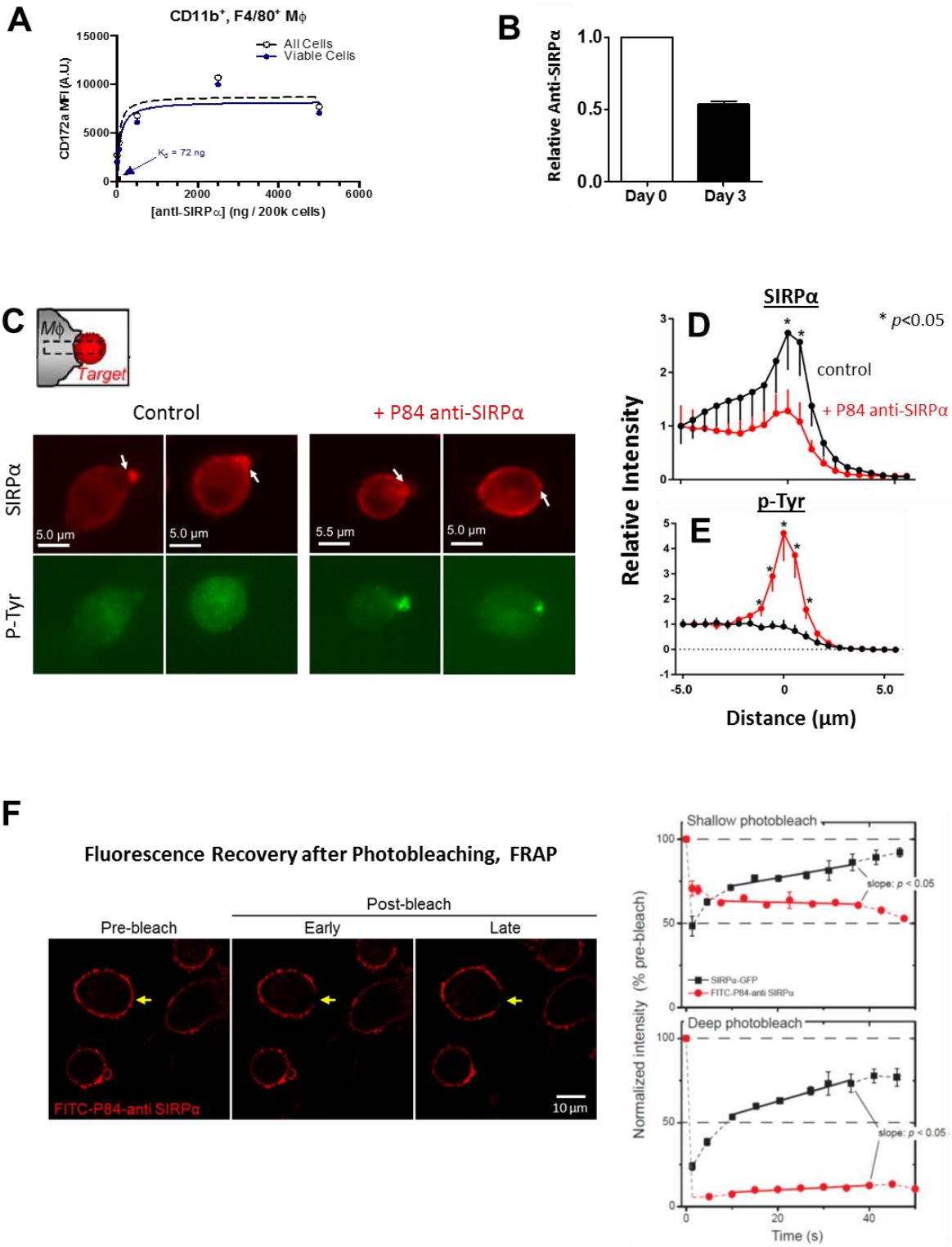

Figure 4.S1. P84 SIRPα antibody binds to NSG macrophages and immobilizes SIRPα. (**A**) Affinity of anti-SIRPα for NSG macrophages. Data fit using saturation a binding model (All cells: $R^2 = 0.73$, $K_d = 50$ ng; Viable cells: $R^2 = 0.78$, $K_d = 72$ ng). *In vitro* phagocytosis assay using phorbol myristate acetate (PMA) treated human monocytes (THP-1) cell line and a human lung carcinoma cell line (A549, WT and CD47 KD). (**B**) Normalized SIRPα inhibit between injections day 0 and day 3 when tumors are isolated. Approximately 53% of SIRPα inhibition remained on macrophages on day 3 (n = 3). (**C**) Representative images of mouse macrophages ± anti-mSIRPα (P84) incubated with opsonized mouse RBCs for 30 minutes. Following phagocytosis, cells were fixed and stained for mSIRPα and p-Tyr residues. Displayed are epifluorescent images used to quantify proteins in phagocytic synapse per (Tsai & Discher, 2008). (**D-E**) Quantification of SIRPα and phosphor-tyrosine residue accumulation in phagocytic synapse of mouse macrophages ± anti-mSIRPα. Fluorescent intensity was normalized to macrophages that were not undergoing phagocytosis (n = 7). (**F**) Representative images and analysis of FRAP SIRPα-GFP diffusion ± anti-mSIRPα (P84). Sides of cells were bleached and allowed to recover (n = 3).

Figure 4.S2. Targeting antibodies bind mainly to cancer cells and mouse macrophage

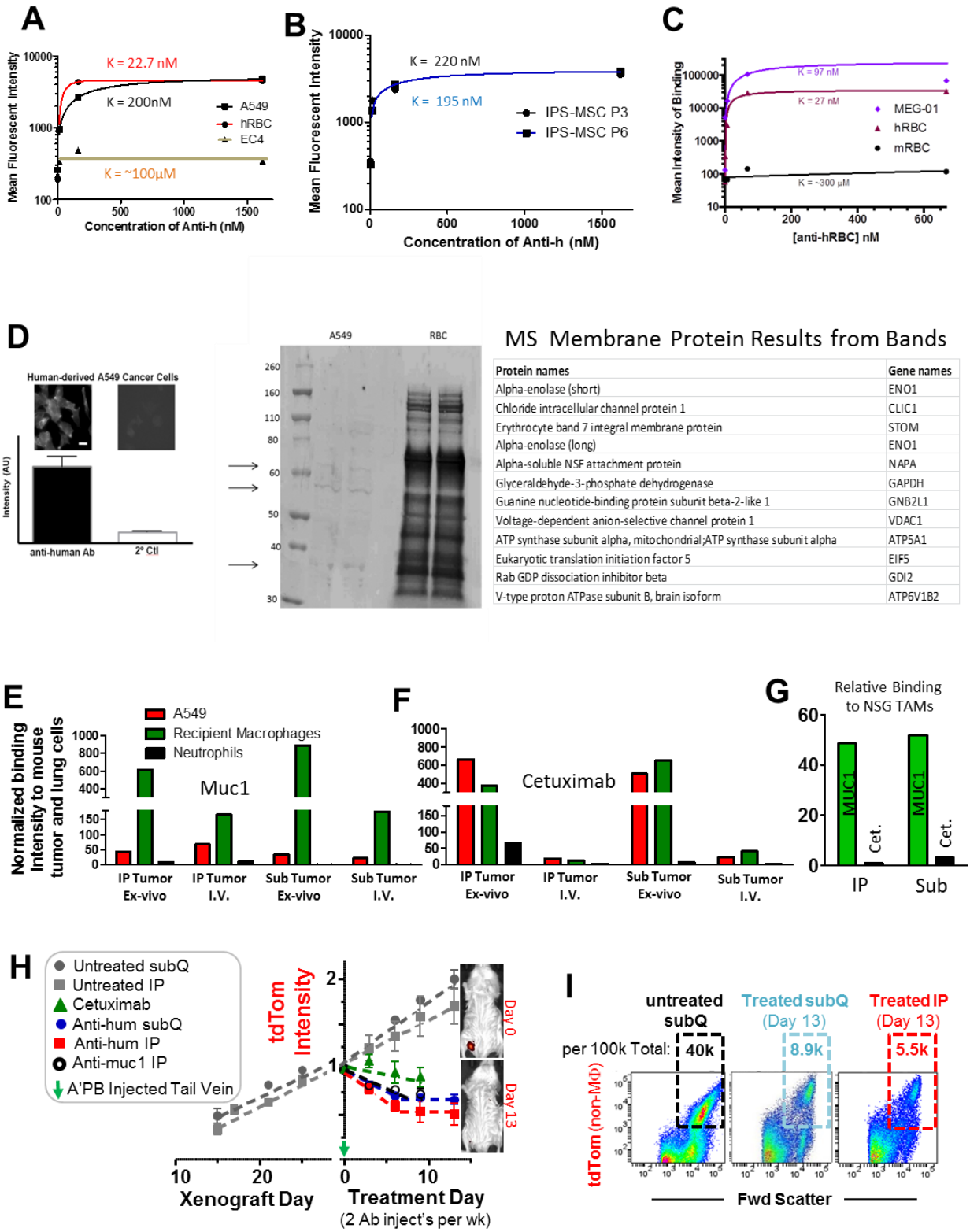

Figure 4.S2. Targeting antibodies bind mainly to cancer cells and mouse macrophage. (**A and B**) Binding curve for anti-hum against hRBC, A549, EC4s, and IPS-MSC of different passage number. Each point is composed of the average intensity of 10,000 cells for each. (**C**) Flow cytometry (gray=isotype control; black=MEG-01) of 67 nM Ab binding to MEG-01 cells. Fitting parameters indicate that when B is similar for mRBC and hRBC K for mRBC >> hRBC indicating weak affinity to mRBC. Mixing human and mouse RBCs did not affect binding to either species. Model: Y=A+B*X/(K+X); hRBC: A=80, B=35524, K=26.5nM, R^2=0.97; mRBC: A=80, B=14210, K=323427nM, R^2=0.22; MEG-01: A=80, B=262480, K=97nM, R^2=0.99. (**D**) Verification of anti-hum binding to A549 cells, immunofluorescence and Western blot. Immunofluorescence confirms anti-human antibody binding (left) to A549 *in vitro* compared to secondary antibody only control (right) (scale bar = 10 μm). Images have been adjusted to allow visualization of cells in control image. Bar graph below the images reflects true fluorescence of each unaltered image. The blot shows three main bands with several lower intensity bands which anti-hum binds to. Shown are possible surface proteins identified by mass spectrometry that correspond to the molecular weight from the 3 most intense bands. (**E-F**) Binding of systemically injected anti-hMUC1 and Cetuximab antibody into NSG mice bearing 8 wk old tdTom A549 tumors. Antibody could circulate for 3 hours then the mouse was then sacrificed, tumors isolated, disaggregated, and split into two samples. One sample was stained for targeting antibody and the other was directly incubated with anti-MUC1 or Cetuximab (*ex vivo*) to ensure specific binding and to test non-specific binding. After direct incubation, samples were then stained for targeting antibodies. (**G**) Normalized NSG TAM binding data from subcutaneous and intraperitoneal tdTom A549

tumors of anti-MUC1 and Cetuximab. 10ug of each antibody was systemically injected and 3 hours later the mouse was sacrificed, tumor tissue stained, and analyzed by flow cytometry. (**H**) Normalized *In vivo* growth curve of tdTom A549 subcutaneous and intraperitoneal tumors. Growth of tumors was monitors by tdTom fluorescent intensity. Tumors grew at a similar rate for 30 days then were treated with NSG A'PB MΦ. All tumors shrank comparably until days 9-13 when shrinkage plateaus (n = 3-6). (**H, inset**) Representative fluorescent images of tdTom signal from IP tumors comparing tumor intensities of treatment day 0 to day 13. (**I**) On Day 13, all tumors were removed and analyzed by flow cytometry. TdTom A549 cells remaining in the tumors were identified by forward scatter (size) and tdTom intensity, while excluding $CD11b^{+}$ $F4/80^{+}$ cells. Tumors treated with A'PB MΦ all showed decreased A549 populations in proportion to measured florescent intensity.

Figure 4.S3. Donor cells alone inhibit tumor growth, but priming Fcγ receptor on APB MΦ yields the most effective anti-tumor response

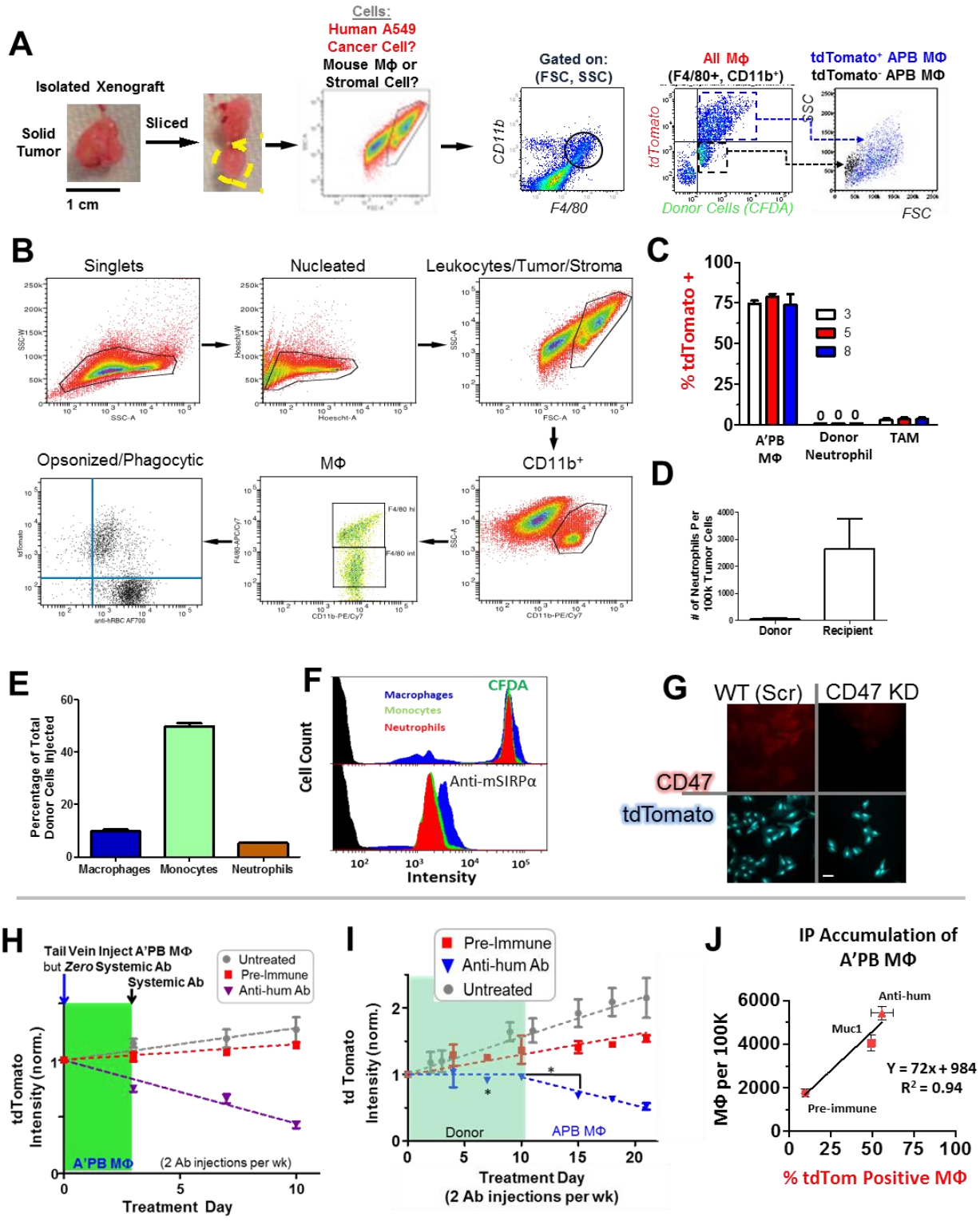

Figure 4.S3. Donor cells alone inhibit tumor growth, but priming Fcγ receptor on APB MΦ yields the most effective anti-tumor response. (**A**) Schematic of method used to analysis disaggregated tumor tissue. Following dissociation and antibody staining, samples are analyzed using flow cytometry. (**B**) Flow cytometry dot plots showing gating strategy used to identify and analysis macrophage eating and abundance in tissues. (**C**) Phagocytosis assay using disaggregated tdTom A549 tumors that were treated 24 hours prior with A'PB MΦ. Cells were platted for 24 hours and analyzed by flow cytometry focusing on phagocytosis of tdTom A549 cells by A'PB MΦ, donor neutrophils, or recipient MΦ (TAMs). (**D**) Three days after injection of APB engineered NSG mouse marrow, subcutaneous WT A549 tumor were harvest and analyzed by flow cytometry for neutrophils. Abundance of neutrophils in the tumor per 10^5 cells screened. Despite the moderate level of neutrophil eating, the small number of neutrophils in the tumor make them an ineffective anti-tumor effector cell type. Recipient neutrophils seem to have opposite problem, high number of neutrophils in the tumor, but they are non-phagocytic. (**E**) Immune cells makeup of engineered NSG mouse marrow cells before injections into tumor bearing mice. Together macrophages, monocytes, and neutrophils consist of 65% of the marrow injected (n=3). (**F**) Representative histogram of flow data from CFDA stained and anti-mSIRPα engineered NSG mouse marrow cells. (**G**) Fluorescent imaging of tdTom CD47 knockdown A549 compared to tdTom WT. (**H**) *In vivo* growth curve of subcutaneous tdTom A549 tumors. Tumor growth was measured by tdTom intensity. Tumor were approximately 70 mm^2 in size at the start of treatment. Male mice were treated with 10 million NSG mouse donor marrow cells that were SIRPα inhibited and Fcγ receptor pre-loaded with anti-hum or pre-immune antibody *ex-vivo* then tail vein

injected back into mice. Donor injection was giving on day 0 with no systemic antibody treatment. On treatment day 3, biweekly systemic injection of antibody (n = 6). (**I**) *In vivo* growth curve of subcutaneous WT tdTom A549 tumors. Tumor growth was measured by tdTom intensity. Tumor were approximately 70 mm^2 in size at the start of treatment. Treatment day 0-10 mice were injected with 10 million marrow donor cells with biweekly anti-hum injection. On day 10, a mixture of male and female mice received a second treatment donor cells, but with SIRPα inhibit. (n = 4). (**J**) A'PB MΦ accumulation in IP tdTom A549 tumors as a function of % tdTom+ MΦ within each pollution. Relative phagocytosis and accumulation depends on the antibody used to opsonize cancer cells with the following order: anti-hum › anti-hMuc1 › Pre-immune (n = 3; $R^2 = 0.94$).

Figure 4.S4. Engineered donor macrophages in recipient tumors are assayed for phagocytosis and 3D-motility

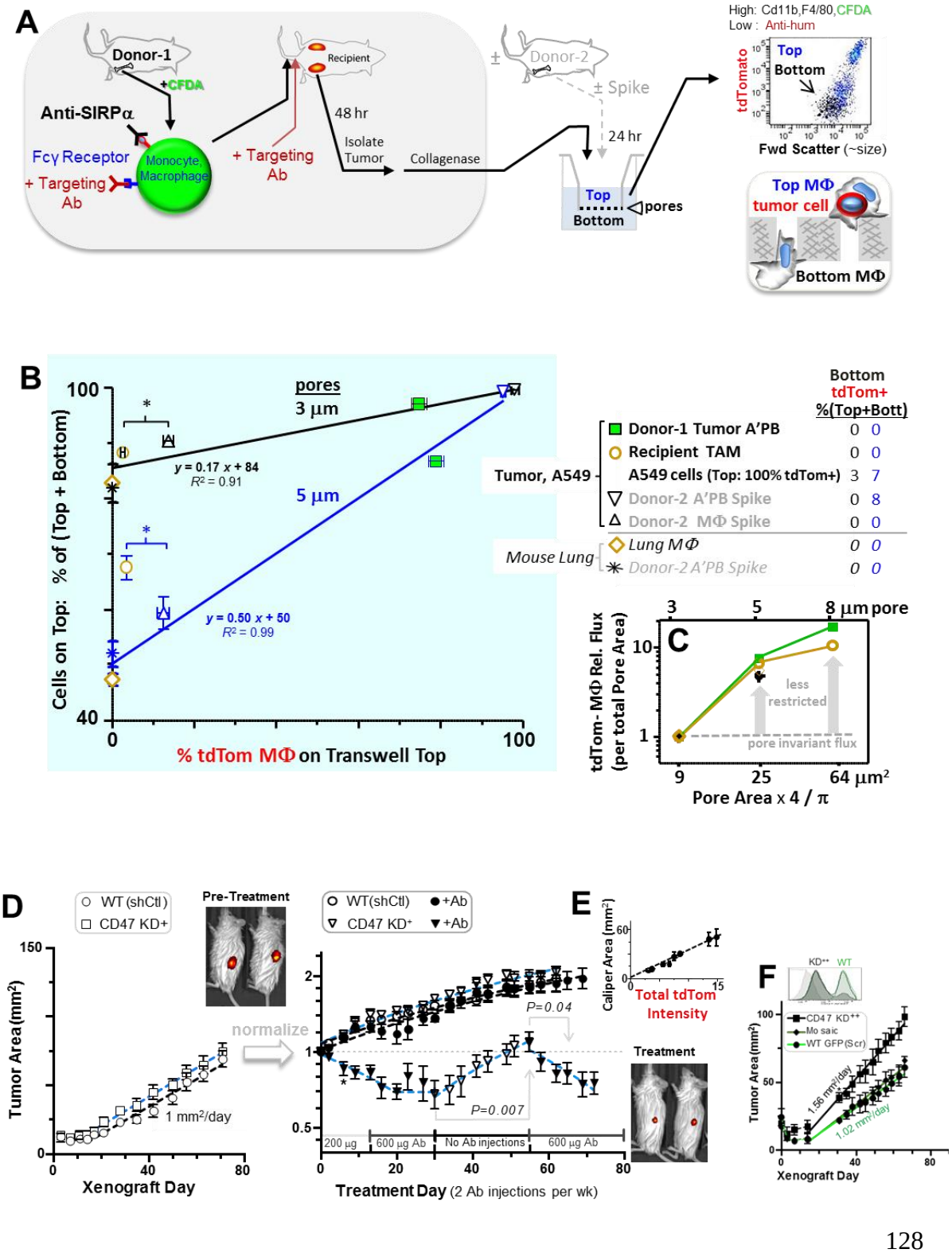

Figure 4.S4. Engineered donor macrophages in recipient tumors are assayed for phagocytosis and 3D-motility. (**A**) Schematic of the 3D-motility assay used to assess macrophage eating and migration from primary NSG mouse marrow, lung, and tdTom A549 subcutaneous tumors. Bone marrow from donor-1 was harvested, engineered (SIRPα inhibited and Fcγ receptor primed with anti-hum), and injected into NSG mice with 8 wk old subcutaneous tdTom A549 tumors on both flanks. Three days after injection a injection of anti-hum was given and 3 hours later tumors were isolated and plated on tops of 3 μm and 5 μm transwells at 300k cells per well and allowed to migrate for 24 hours. In some conditions marrow from a second donor was spiked with the disaggregated tumor. The transwells were scrapped, stained and analyzed by flow cytometry. (**B**) Plot of 3D migration of donor marrow, lung, and tumor macrophages as a function of macrophage phagocytic activity of tdTom A549 cells on 3 μm (black) and 5 μm (blue) pores ($n \geq 3$). (**B, inset table**) macrophage eating of tdTom A549 cells on the bottom of 3 μm (black) and 5 μm (blue) transwells along with migration of tdTom A549 tumor cells. Only one condition shows eating on bottom (most phagocytic with largest pores) (n =3 -7). (**C**) Transwells with different pore sizes have different numbers of pores (3 μm = $2x10^6$, 5 μm = $0.4x10^6$, etc.), which must be accounted for in the total pore area to calculate cell flux (#/area). Thus the flux of cells through 5 μm pores should be smaller by (5/3)^2($0.4x10^6/2x10^6$) = 0.56-fold, but the 5 μm transwell instead allows 3-fold more of each macrophage phenotype through because the 5 μm constriction is far less severe than the 3 μm. The plotted flux of macrophages is therefore 5.4-fold higher for this larger pore, whereas the much larger 8 μm pore does not greatly increase this flux, so that 3 μm pores are by far the most restrictive. (**D, Left)** *In vivo* growth curve of CD47 KD^+ during 2

periods of no treatment. (n = 8-12). Slope of linear fit = 1.02 mm^2/day corresponding to tumor growth rate (R^2=0.99). (**D, insets**) Representative fluorescent overlays of untreated (left) and Ab treated (right) mice at the end of the treatment period. (**D, Right**) Tumor response to 200 and 600 μg anti-human / mouse followed by removal of antibody and subsequent re-administration (n = 4-8). (**E**) *In vivo* measured growth of subcutaneous tdTom A549 tumors. Correlation of measuring tumors using calipers (cross sectional area) or by tdTom intensity over a 30 day period (n = 4 mice). (**F**) CD47 KD^{+} cells were further sorted to generate CD47 KD^{++}, an ultra-deep knockdown. Xenotransplants in NSG mouse flanks show a slight growth advantage for CD47 KD^{++} (linear fit slope = 1.56 mm^2/day, R^2=0.99) compared to tumors comprised of WT GFP Scr (same as WT/shCtl) either in part or in whole (linear fit slope = 1.02 mm^2/day, R^2=0.98) (n = 4 - 8). (**F, inset**) Flow cytometry of cells used in xenotransplants (gray=isotype; black=CD47 KD^{++}; green dashed outline=WT GFP Scr; green fill=Mosaic).

Figure 4.S5. Stiff matrix regulation of SIRPα and phagocytosis of a lung cancer cell line are enhanced by inhibition of hSIRPα

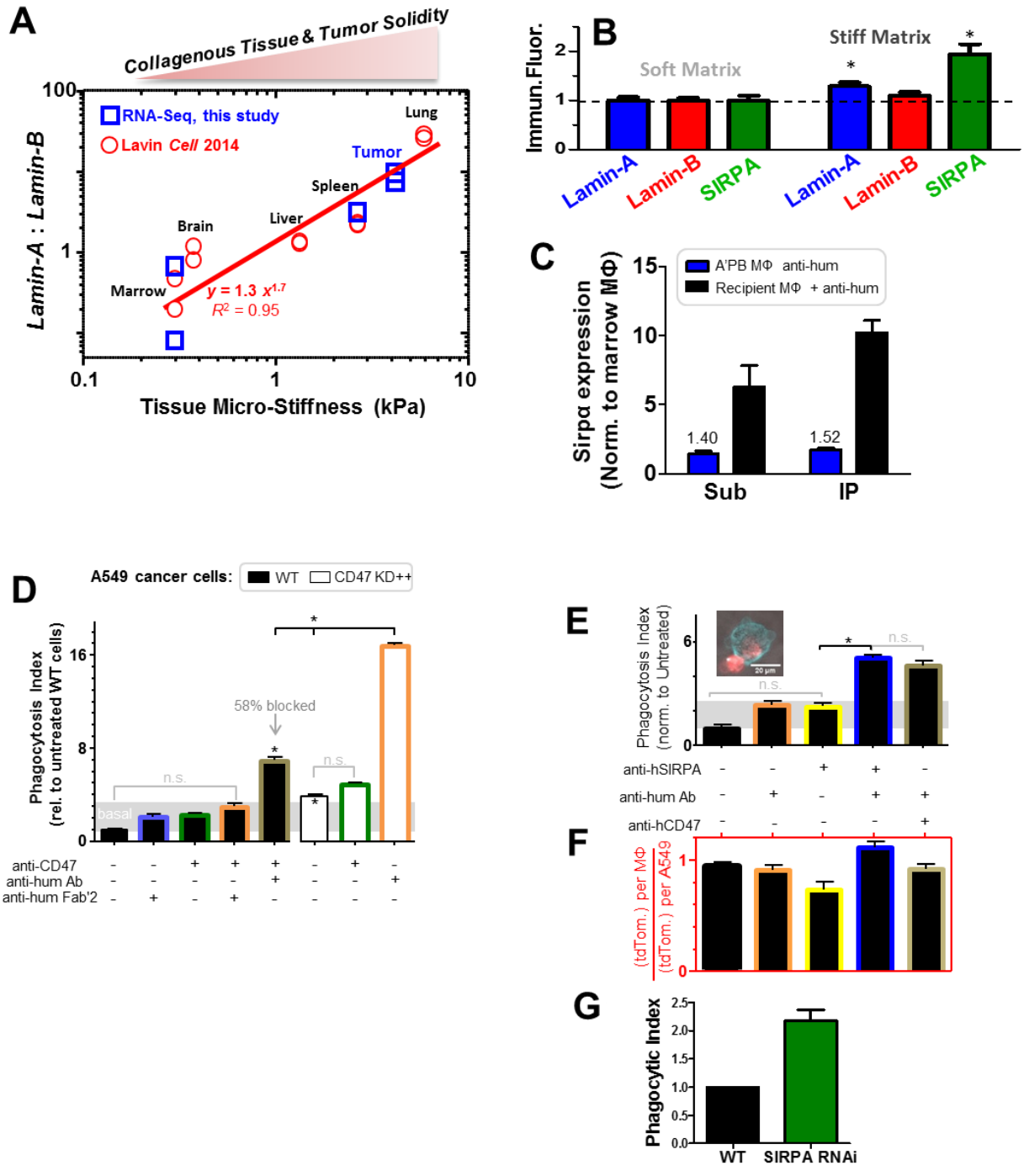

Figure 4.S5. Stiff matrix regulation of SIRPα and phagocytosis of a lung cancer cell line are enhanced by inhibition of hSIRPα. (**A**) Data mining published macrophage mRNA sequences for *Lamin-A* and *Lamin-B* shows that *Lamin-A : Lamin-B* ratios increase in macrophages with increasing stiffness of resident tissue and flows a linear trend on a log-log scale (R^2=0.95). *Lamin-A : Lamin-B* RNA sequence data from macrophages data from (4B) shows the same trend as published data. (**B**) *In vitro* experiment using PMA differentiating THP-1s on different matrix stiffness, (soft-marrow and stiff-tumor). After 7 days of culturing, THP-1s were fixed and stained for LAMIN-A, LAMIN-B, and SIRPα. Fluorescent intensity for each protein was normalized to the soft condition. LAMIN-B remained unchanged, but LAMIN-A and SIRPα significantly increased ($P<0.05$, n = 3). (**C**) Quantification of Sirpα on A'PB donor macrophages and recipient macrophages from large tdTom A549 IP and subcutaneous tumors in NSG mice. Tumors were isolated 3 days after tail-vein injection of donor cell. Data is normalized to macrophages taken from NSG marrow (n = 3). (**D**) THP-1 phagocytosis of WT and CD47 KD A549 was measured by counting the number tdTom A549 cells per THP-1 and normalizing to control (cells only) under different eating condition ($n\geq3$). (**E**) THP-1 phagocytosis of A549 was measured by counting the number A549 cells per THP-1 and normalizing to control (cells only) under different eating condition ($n \geq 4$). (**E, inset**) Image of a positive eating event with CD11b stain in green showing THP-1 and tdTom fluorescence indicating A549 cancer cell. (**F**) Quantification of internalized tdTom fluorescent intensity of THP-1s and normalizing to tdTom intensity from uneaten A549 cells. Quantification was done from the samples taken from figure 1A ($n \geq 4$). (**G**) *In vitro* phagocytosis assay using PMA treated THP-1s and human red blood cells. KD of SIRPα

in THP-1s resulted in 2.2-fold increase in eating of anti-hum opsonized RBCs over WT THP-1s (n = 4).

Figure 4.S6. Safety and *in vivo* confirmation of human donor efficacy

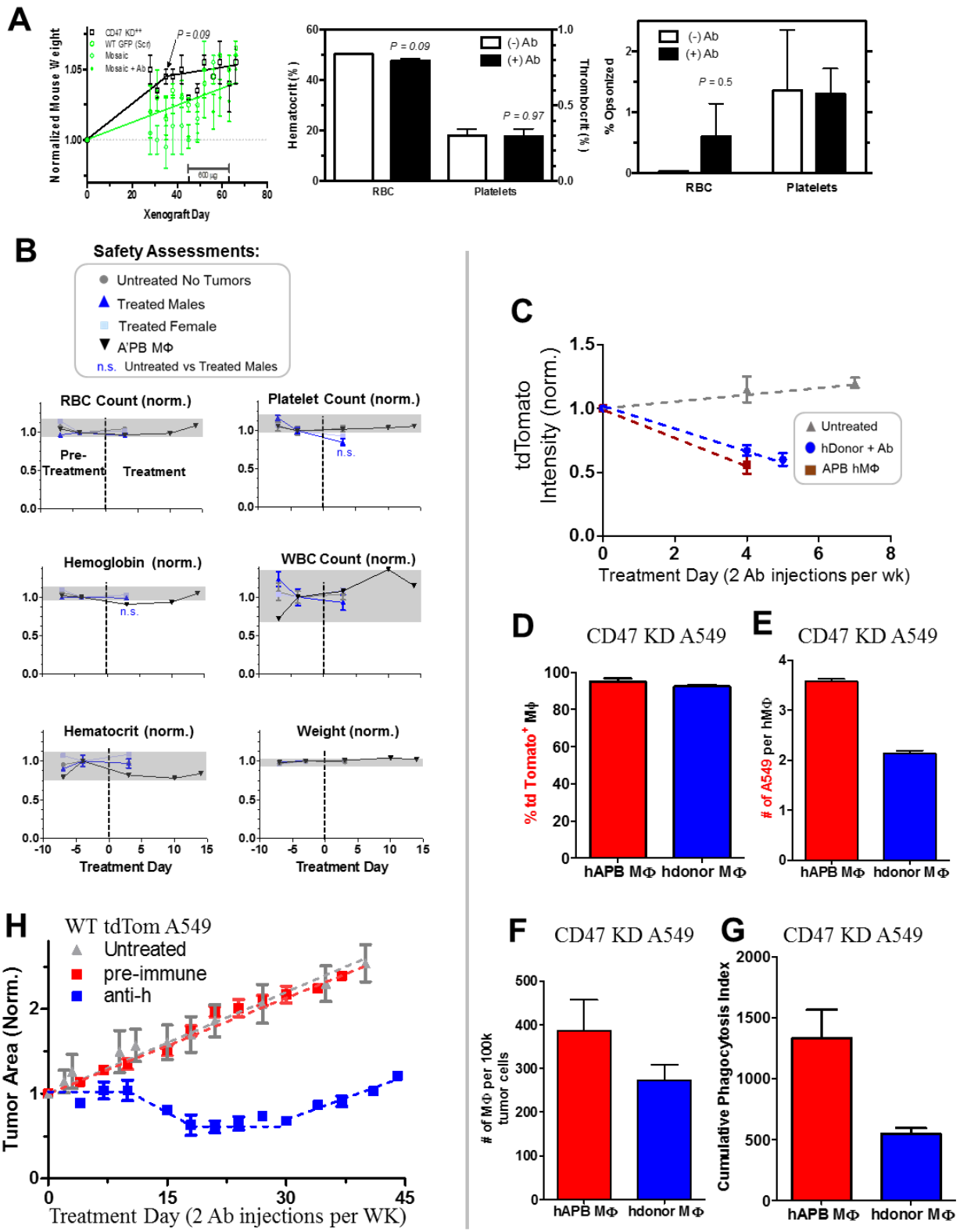

Figure 4.S6. Safety and *in vivo* confirmation of human donor efficacy. (**A**) Weight throughout duration of study (including pre-treatment, treatment, and post-treatment). Weight is normalized to weight at date of xenograft implantation. Mice used in Mosaic Study (n = 4-8). GFP WT/shCtl, Mosaic, Mosaic+Ab are grouped together and the green solid line reflects the linear fit. CD47 KD^{++} mice show slightly different weight responses as shown by the black solid line. Addition of antibody shows a slight decrease in hematocrit, but no change in thrombocrit ($n \geq 3$). I.V. injection of anti-hum antibody shows no specific binding to mouse RBC or platelets *in vivo* ($n \geq 3$ per group). (**B**) Blood profiles taken from male mice treated with APB macrophages ($n \geq 3$) before and after treatment. Parameters were normalized to day 4 of pre-treated. (**C**) *In vivo* growth curve of CD47 KD tdTom A549 tumors treated with NSG donor cells and anti-hum antibody. Growth was measured by tdTom fluorescent intensity. Tumor grew for 8 wks before treatment with human marrow. SIRPα inhibition didn't significantly increase anti-tumor effect in CD47 KD tumors (n = 3). (**D**) Quantification of $CD14^{+}$ $CD33^{+}$ $CD66b^{-}$ human macrophages eating in CD47 KD A549 tumors. Three days after injection tumors were harvested and human macrophages were analyzed by flow cytometry. Macrophages ± SIRPα inhibit had the same eating percentage, 95% (n = 4). (**E**) However, human macrophages with anti-hSIRPα had engulfed an average of 3.5 tdTom A549 tumor cells whereas donor only was only 2.2 (n = 4). (**F**) Quantification of the number of human macrophages per 10^5 cells screened on the flow cytometer (n = 4). (**G**) Calculation of the cumulative phagocytosis index using data from fig. S8D-F. The human APB MΦ indexes are comparable to indexes from NSG APB MΦ from figure 1. (**H**) *In vivo* growth curve of tdTom A549 tumors. Growth was measured by cross sectional tumor area. Tumor grew

for 8 wks before treatment with NSG marrow plus anti-hum at day 0 then (n = 4). Treatment day 0-10 mice were injected with 10 million marrow donor cells with biweekly anti-hum injection. On day 10, a mixture of male and female mice received a second treatment donor cells, but with SIRPα inhibition.

Table 4.S1. Relative IgG supplementation

	Total IgG	Adult mouse		Ab Injections
	mg/mL	Blood (mL)[1]	mg IgG	% of IgG
C57BL/6[2]	1.5	2.4	3.6	17%
Humanized NSG[3]	0.165	2.4	0.4	154%
		Adult Human		0.3 mg Rhogam
	mg/mL	Blood (mL)	mg IgG	% of IgG
Hu Serum	10	5000	50000	0.0006%

Table 4.S1. Relative IgG supplementation. Calculated estimate of the IgG percent in immunocompetent mouse strains. Calculation assumes a 30 g mouse and 0.6 mg Ab injection. % of IgG is calculated as 0.6 mg injected Ab / total mg IgG * 100%. This value provides a magnitude of the Ab dosage for comparison with what is present in immuncompetent animals. Also as a comparison, a typical 300 μg dose of Rhogam represents 0.0006% of total human IgG. Literature values: mouse blood volume[1] from, C57BL/6 IgG concentration[2] from, humanized NSG IgG concentration[3] from (Rajesh *et al.*, 2010).

Table 4.S2. Donor vs. TAM abundance in tumor periphery and core

Cell Type	Tumor Location	per 100K Cells
A'PB MΦ	Periphery	2921
A'PB MΦ	Periphery	3122
TAM	Periphery	3348
TAM	Periphery	3599
A'PB MΦ	Core	3399
A'PB MΦ	Core	1631
TAM	Core	6118
TAM	Core	5682

Table 4.S2. Donor vs. TAM abundance in tumor periphery and core. Flow cytometry population analysis of A'PB MΦ and TAMs in periphery and core of tdTom A549 subcutaneous xenografts in NSG mice.

Table 4.S3. CD47 cell surface density

			In Vitro		*In Vivo*	
		Area (μm²)	CD47 (norm)	CD47/μm²	CD47 (norm)	CD47/μm²
	WT Scr	382	5.00±0.04	463	5.5±0.2	509
	CD47 KD^{+}		2.12±0.05	196	4.1±0.1	379
	CD47 KD^{++}		1.26±0.04	117	2.37±0.07	219
Mosaic	GFP^{+}, CD47hi		6.20±0.02	574	3.9±0.2	361
Mosaic	GFP^{-}, CD47hi		4.73±0.03	438	2.7±0.2	250
Mosaic	GFP^{-}, CD47lo		0.41±0.05	38	0.66±0.03	61
	hRBC	141±3.0	1.00	250		
		Engstrom 1998		Tsai 2008		

Table 4.S3. CD47 cell surface density. *In vitro* (cells used for xenotransplant) and *in vivo* (cells recovered from excised tumors) CD47 surface density determined by flow cytometry and immunofluorescence. A549 cell area was determined by measuring area of well spread cells imaged by immunofluorescence. This value was multiplied by two assuming negligible height for well spread cells. We acknowledge that this method underestimates cell area and calculated values for CD47/μm^2 are thus likely overestimates. CD47 intensity was determined by flow cytometry mean fluorescence intensity and normalized to human red blood cells. Arrows indicate IgG treatment responsive cells. We previously reported a CD47 surface density value for hRBCs. Multiplying this value by the normalized CD47 intensity and scaling by the ratio of A549 area to hRBC area previously reported, results in the values presented in the table.

Table 4.S4. Validation of macrophage RNA isolation and sequencing

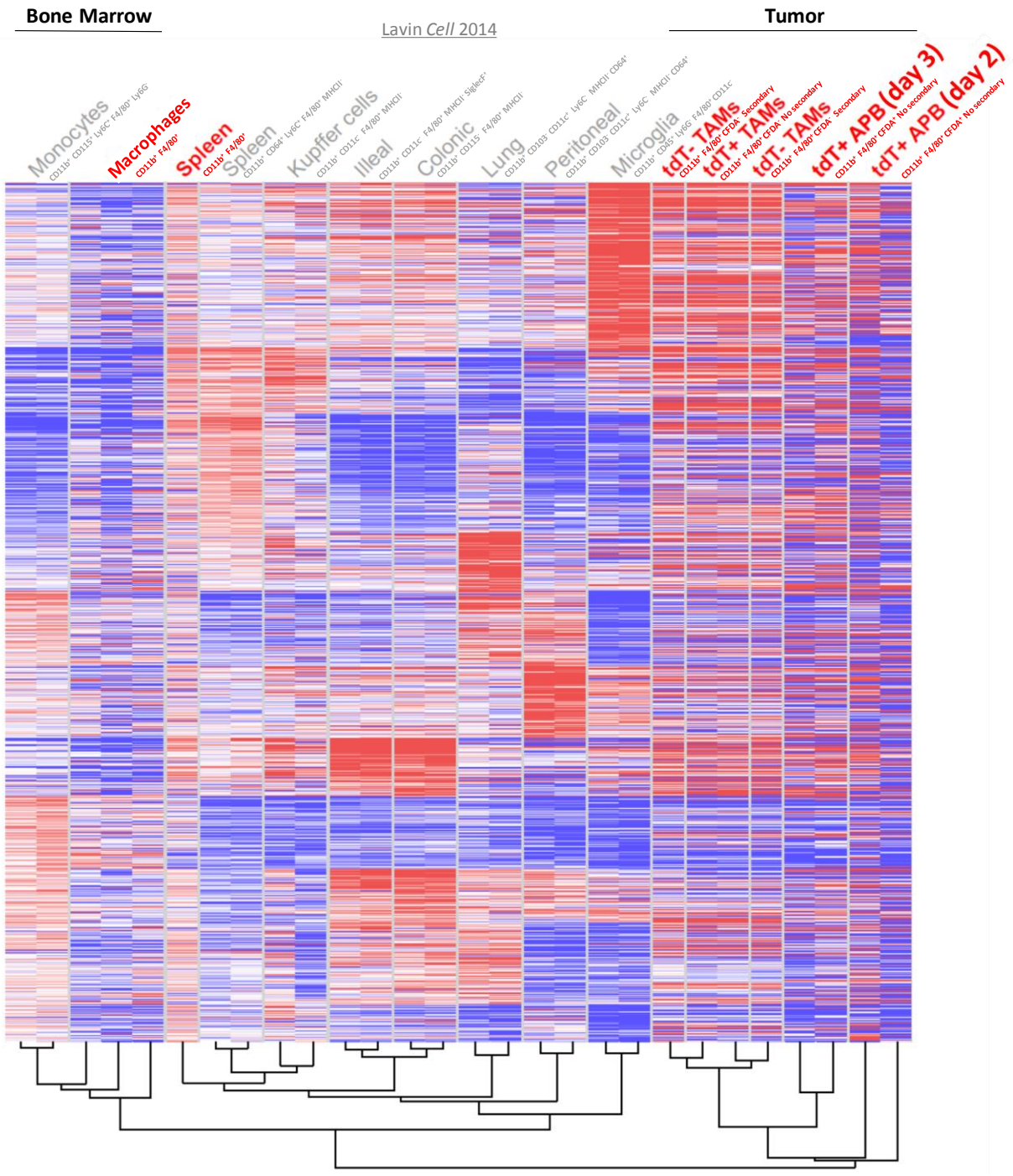

Table 4.S4. Validation of macrophage RNA isolation and sequencing. Macrophages were isolated from different NSG mouse tissues and sorted on CD11b, F4/80, CFDA, and tdTom. RNA was extracted from the sorted cells and sent for sequencing. To verify proper cell sorting and RNA isolation, our macrophage sequencing profiles were clustered to published data from (Lavin *et al.*, 2014). Our sorted macrophages clustered with the same tissues as in previously published works with tumor macrophages clustering differently from other tissue macrophages.

Table 4.S5. Profiles of human marrow donors

Age	Weight (lbs)	Height (Ft)	Gender	Race	Blood Type	Smoker
30	166	5'5"	Female	Non Hispanic White	O-	No
31	226	5'10"	Female	African American	B+	No
31	240	6'3"	Male	Irish/Italian	A+	No
22	180	5'8"	Male	Hispanic	O+	No

Table 4.S5. Profiles of human marrow donors. Human marrow was isolated from 4 different donors with varying profiles to ensure that donor to donor variation had no effect on treatment outcome.

Chapter 5: SIRPα inhibition in marrow macrophage initiates acquired immunity against primary and metastatic melanoma

This chapter presents work featured in a manuscript to be submitted to Science Immunology.

Contributing authors: Cory Alvey, Lucas Smith, and Dennis Discher.

Lucas Smith – Lung metastasis model (Fig. 5.2)

ABSTRACT

Marrow-derived macrophages (MDM)s can be highly phagocytic and have been previously shown to shrink human xenografts with SIRPα inhibition. Yet the ability of MDMs and tumor-associated macrophages (TAM)s to activate acquired immunity is unknown. By inhibiting MDMs from recognizing other cells as 'self', tail-vein injected donor cells accumulate in solid tumors in proportion to their engorgement on melanoma cells opsonized by anti-Trp1 antibody. TAMs failed to impact tumor growth despite a modest increase in eating with addition of anti-Trp1. In contrast, engineered macrophages had sustained tumor shrinkage for 7 days despite T-cell depletion. Treated tumors eventually regrew, but not for treated mice with intact T-cells. 'Cured' mice re-challenged with melanoma had significantly delayed tumor growth, whereas untreated mice grew tumors within days of challenge. Injection of engineered macrophages greatly reduced melanoma metastasis to the lungs compared to treatment with anti-Trp1 without donor cells. Surprisingly, systemic injection of 'self' inhibited macrophages had no measurable impact on blood profiles, weight, and did not cause GvHD even after activation of acquired immunity against syngeneic tumors.

5.1 INTRODUCTION

It was once thought that targeting of the immune system to a foreign invader was driven by the presence of an activation signal, but with discovery of 'self' markers it is now understood that activation of immune cells is facilitated by the absences of 'self' signaling, in addition to activation signals. A particularly interesting 'self' marker is CD47 as it binds to SIRPα on the surface of phagocytes, inhibiting phagocytosis (Oldenborg *et al.*, 2000; Willingham *et al.*, 2012). SIRPα signaling leads to myosin-II inhibition which normally makes phagocytosis efficient (Tsai & Discher, 2008). CD47 is expressed on all cells and was first identified on solid tumors (Mawby *et al.*, 1994) as most cancers overexpress it, with increasing expression correlating with negative clinical prognosis (Fujiwara *et al.*, 2011; Lan *et al.*, 2012; Lu-emerson *et al.*, 2013; Majeti *et al.*, 2009; Willingham *et al.*, 2012; Zhang *et al.*, 2013). Given this, it is unsurprising that common oncogenes regulate expression of 'self' markers (Casey *et al.*, 2016). In *mice* bearing *human* tumor xenografts, combining anti-hCD47 with a distinct Ab that can opsonize human tumor cells has been shown to shrink tumors (Chao *et al.*, 2010; Weiskopf *et al.*, 2013). In syngeneic mouse models of melanoma, *in situ* knockdown of mCD47 beginning ~1 week after engraftment can slow tumor growth over the subsequent ~2 weeks (>90%). The slowed growth is attributed to tumor-associated macrophages (TAMs), but does not include injection of TAM-activating factors (eg. tumor-opsonizing Ab) (Wang *et al.*, 2013). Indeed, a current controversy in the field is whether inhibition of *just* the CD47-SIRPα interaction alone is sufficient to reproducibly shrink tumors: a recent replication study (Horrigan *et al.*, 2017) not only failed to demonstrate efficacy as first reported for

anti-mCD47 inhibition (Willingham *et al.*, 2012), but also questioned significance of past data.

Conflicting effects of anti-CD47 therapy add to the safety concerns and questionable effector cell complications that already exist. Ubiquitous expression of CD47 causes rapid and reproducible (Horrigan *et al.*, 2017) decreases of blood cells in primates (Weiskopf *et al.*, 2013) as well as mice (Willingham *et al.*, 2012) with intravenous injection of species-appropriate anti-CD47 antibody. Furthermore, *Cd47* knockout mice can develop autoimmune disease with auto-antibodies, anemia, and ~60% shorter lifespan (Oldenborg *et al.*, 2002). Safety of CD47 inhibition is thus one critical metric in ten new clinical trials with intravenous anti-hCD47 or anti-hSIRPα (Archambeaud e atl., 2016; Burgess *et al.*, 2015; Chao *et al.*, 2016; Kang, 2011; Sievers *et al.*, 2016a, Takimoto, 2014). Safety of intravenous injection of anti-SIRPα is of equal concern (Rodriguez *et al.*, 2013), but our recent studies show that blocking SIRPα on marrow macrophages with anti-SIRPα before cell injection prevents loss of RBCs. In addition to the safety concerns, TAMs prove to be weakly phagocytic when compared to macrophages from other tissues (Rodriguez *et al.*, 2013), limiting their role as an effector cell in anti-CD47 therapy. Unlike TAMs, undifferentiated marrow-derived macrophages (MDMs) seem to be among the most phagocytic, but whether these cells alone can cause tumor remission remains unanswered. More evidence is arising that an acquired immune response is ideal for cancer therapy as it may eliminate primary and metastatic tumors with the potential to prevent relapse.

Recent anti-CD47 studies in immunocompetent mice suggest that tumor dendritic cells (DCs) are responsible for all of the therapeutic effect observed with anti-CD47

treatment (Liu *et al.*, 2015). Specifically, DCs phagocytose and then present neoantigens to active CD8 T-cells, which seem to be the main effector cell. Interestingly, knockdown of SIRPα in DCs enhances their ability to activate an acquired immune response (Liu *et al.*, 2016), but it is unknown whether SIRPα inhibited MDMs can initiate an acquired immune response or even if that is necessary for complete tumor regression.

We hypothesized that phagocytosis by MDMs alone has an important role in reducing early tumor growth in addition to being able to activate an acquired immune response. Here an immunocompetent, syngeneic, mouse model for orthotopic and metastatic melanoma is used to study the anti-cancer effect of donor MDMs. This model has proven reliable in evaluating the development of an adaptive immune response, while also being clinically relevant. Beginning with evidence of *in vivo* engulfment, engineered mouse MDMs (rather than donor DC or lymphocytes) are shown here to accumulate in tumors and cause substantial shrinkage before activation of T-cells. However, the development of an adaptive immune response is necessary for sustained tumor regression and prevention of tumor growth when re-challenged. Blood parameters here are unaffected by the SIRPα-inhibited, donor macrophages and their activation of the acquired immune system.

5.2 MATERIALS AND METHODS

Antibodies: Anti-mSIRPα antibody (rat anti-mouse CD172a, P84, BD Pharmingen). Opsonization Primary antibodies used for flow cytometry and imaging included CD11b-APC (Biolegend) as well as anti-mouse F4/80-APC/Cy7 (Biolegend) and CD11b-PE/Cy7 (Biolegend). Secondary antibodies included donkey anti-rabbit Alexa Fluor 488 (Invitrogen) and donkey anti-rabbit Alexa Fluor 647 (Invitrogen). When required, nuclei were stained by either 7-Amino-actinomycin D (7-AAD, Sigma) or Hoechst 33342 (Invitrogen).

Immunofluorescence: B16F10 cells were seeded on 18 mm circular microscope cover slips in a 6-well plate and allowed to adhere overnight. Cells were fixed with 4% paraformaldehyde for 15 minutes at room temperature (RT), and then washed three times with PBS. Next, cells were blocked for 30 minutes using 3% BSA + 0.05% Tween-20, followed by a 2-hour RT primary antibody incubation in blocking buffer. These primary antibodies were used at a 1:100 concentration. After incubation, cells were again washed three times with PBS. A 1:400 PBS dilution of donkey secondary antibodies (Alexa Fluor 488 and 647) was added for 1 hour at RT. Hoechst 33342—at a concentration of 1 μg/mL—was used to stain DNA for 15 minutes at RT. Cover slips were washed a final three times with PBS before being mounted on slides with ProLong Gold Antifade Reagent (Life Technologies), cured for 24 hours, and sealed with nail polish prior to imaging. Images were acquired by an Olympus IX71 inverted microscope with a 300W Xenon lamp illumination using 40×, 60×, or 150× objectives with or without 1.6× magnification. Image analysis was done in ImageJ (NIH).

Flow Cytometry of *In Vitro* Cultured Cells: B16F10 cells were dissociated using 10 mM trypsin in PBS, washed, and re-suspended in 2% FBS in PBS. Antibody incubation was done at RT for 1 hour, followed by washing and resuspension in 2% FBS. Samples were run on a BD LSRII.

Syngeneic Tumor Model: C57 mice were purchased from The Jackson Laboratory and were housed in a BSL 2 facility at the University of Pennsylvania. Mice were implanted with either 2×10^5 or 5×10^5 B16F10 (acquired from ATCC) cells injected into the subcutaneous tissue or intravenously. Tumors grew to 10 mm^2 before the start of treatment. Cross-sectional tumor area was measured by calipers to monitor growth of tumors. Fur was dampened to enhance accuracy. During each tumor measurement, mouse body mass was measured with an enclosed digital scale.

Antibody Treatment and T-cell Depletion: Mice were warmed under a heat lamp prior to tail vein injection. Anti-Trp1 (TA99, Bio X Cell) was given to mice 3-4 times per week at 250 μg per animal. CD4 and CD8 T-cells were depleted using anti-mouse CD4 (GK1.5, BE0003, Bio X Cell) and anti-mouse CD8 (2.43, BE0061, Bio X Cell), respectively. Depletion antibodies were given interperitoneally at 200 μg per mouse biweekly (Liu *et al.*, 2015).

Adoptive Transfer of Bone Marrow: Femurs and tibias of donor C57 mice were removed, and bone marrow was flushed with 5% FBS/PBS. Red cells were lysed by incubation with RBC lysis buffer (Sigma) in 4% FBS/PBS for 12 minutes at RT. Cells were washed twice and resuspended in warm 5% FBS/PBS. Following the addition of 1:1000 CFDA-SE (Invitrogen), cells were incubated for 15 minutes at 37°C, and then centrifuged again, resuspended in warm complete DMEM medium, and incubated for an additional 30-40 minutes at 37°C. When applicable, anti-mSIRPα antibody was added during this incubation period. Cells were then washed, resuspended in 5% FBS/PBS, counted, and volume was adjusted to allow injection of 10^6 cells. Remaining cells were analyzed by flow cytometry to establish initial composition.

Sorting of Marrow Cells: In some experiments, marrow phagocytes were sorted from non-phagocytes and dendritic cells. FACS Aria (Biosciences (Helft *et al.*, 2015)) was used to sort 60 million marrow cells using anti-CD135-BV421 (Biosciences,) and anti-SIRPα – FITC (P84, Biosciences) into 15 mL conical tubes containing 1mL FBS. This sorting process generated 20 tubes, which were subsequently centrifuged for 10 minutes at 4,000 rpm. After the supernatant was aspirated, cells were resuspended in 5% FBS/PBS, incubated with targeting antibody for 1 hour, and centrifuged again. Finally, cells were resuspended in 200 µL of 5% FBS/PBS per 10×10^6 cells and put on ice for tail-vein injection.

***Ex Vivo* Tumor Flow Cytometry Analysis:** Unless specified, on the day of tumor isolation mice in the treatment cohort were injected with the standard antibody dose, as

described above. Mice were euthanized by cervical dislocation 1.5-2 hours after injection. Tissues were removed and placed in 20% FBS, and tumor core and periphery tissue were segregated. Tumor tissue was cut into 1-3 mm pieces, transferred to 15 mL centrifuge tubes, and centrifuged to remove media. Tissue was then resuspended in 3 mL warm Dispase (STEMCELL Technologies) supplemented with 3 mg/mL Collagenase (Sigma) and 200 µL of 1 mg/mL DNase I (Roche). Samples were mixed by pipetting for 1-3 minutes until cloudy but not stringy. Dissociation was quenched by addition of 10 mL room temperature PBS, and then the suspension was filtered through a 70 µm cell strainer. The filtrate was centrifuged, the supernatant discarded, and the pellet resuspended in 2% FBS for antibody incubation. Spleens were prepared by mechanical dissociation, filtration, and red blood cell lysis using Red Cell Lysing Buffer (Sigma). Lysed samples were washed and resuspended in 2% FBS for antibody incubation. Prior to antibody incubation, samples were blocked with 1:500 Fc Block (BD Pharmingen) for at least 5 minutes at RT. CD47-AF647 (1:25), donkey anti-rabbit AF488 or AF700 (1:400), donkey anti-rat AF647 (1:400), F4/80 APC-Cy7 (3:50), CD11b PE-Cy7 (1:25), Gr-1 APC (1:25), hCD47 AF647 (1.5:50), and Hoescht 33342 (1:1250) were incubated at RT for 1 hour. Following incubation, cells were washed and resuspended in 2% FBS.

Analysis of Mouse Blood Profiles: 100 µL of blood was isolated from anesthetized mice by retro-orbital bleeds. Blood was collected in Eppendorf tubes containing EDTA. Blood was kept at room temperature and immediately analyzed using a Drew Scientific Hemovet (HV950).

Graft vs. Host Disease: Mice were monitored 3 times a week by researchers and veterinarian technicians at the University of Pennsylvania Perelman School of Medicine mouse facilities for general health and for development of GvHD. Classic signs of GvHD include weight loss (>15%), ruffled fur, loss of fur on the head and rear of the mouse, hunched posture, and reduced activity (Ali *et al.*, 2012; Hartung *et al.*, 2003; King *et al.*, 2009). Development of GvHD is a common occurrence at these facilities as numerous users study CAR T-cell therapies, which frequently cause GvHD (Covassin *et al.*, 2011; Jacoby *et al.*, 2016).

Quantification and Statistical Analysis: All statistical analyses were performed using GraphPad Prism 4. Unless otherwise noted, all statistical comparisons were made by unpaired two-tailed Student *t* tests and were considered significant if $p < 0.05$. Unless mentioned, all plots show mean ± SEM. "n" indicates the number of tumors, cells, or wells quantified in each experiment and is ≥3 in all experiments, except for RNA sequencing data which is for ≥ 2 samples per condition. Figure legends specify the exact meaning of "n" for each figure.

5.3 RESULTS

Donor macrophage phagocytose and accumulate in syngeneic melanoma tumors causing depletion of Trp1 positive cancer cells

Immunocompetent C57 mice were orthotopically challenged with the standard B16F10 mouse melanoma line. Unlike the first anti-mCD47 inhibition studies (Willingham *et al.*, 2012) that used an orthotopic mouse breast tumor that can spontaneously regress and undermine reproducibility (Horrigan *et al.*, 2017), we observed that (*i*) all subcutaneous injections of B16F10 cells (10^5) gave rise to palpable tumors with the similar growth rates (to ~100 mm^2 by 17 ± 3 days) as reported for studies of *in situ* knockdown of mCD47 (Wang *et al.*, 2013), and we observed that (*ii*) zero tumors spontaneously regressed. Previous studies using this model have transitioned to clinical trial(s) for melanoma immunotherapy within years after publishing [eg. (Ali *et al.*, 2009); ClinicalTrials.gov NCT01753089]. C57 mouse marrow was sorted for monocyte/macrophage, and both anti-mSIRPα inhibition and a targeting antibody (anti-Trp1) were added to the two separated fractions (**Fig. 5.1A**). Antibody inhibition of SIRPα is used as previous studies show that SIRPα knockdown in macrophages can promote tumor growth (Pan *et al.*, 2013). The melanocyte-specific protein Trp1 involved in melanin synthesis (Tyrosinase-related protein 1, TYRP1) is targetable (Steitz *et al.*, 2000) as it is expressed on the surface of melanomas (**Fig. 5.S1**).

Antibody primed plus anti-SIRPα blocked MDMs (A'PB MΦ) are abundant when isolated from the B16F10 tumors and show a dominant fraction of macrophages with high DNA intensity that indicates uptake of B16F10 tumor cells as the intensity is equivalent to one B16F10 (**Fig. 5.1B**). Recipient macrophages in tumors treated with anti-Trp1 show

the same shift, but with far fewer Hoechst high cells. The anti-Trp1 treatment significantly increases eating by TAMs, but this level of engulfment is matched by non-engineered donor cells (**Fig. 5.1C**). Fully primed donor macrophages (A'PB with anti-Trp1) showed the highest phagocytic activity with 75% of these cells engulfing a cancer cell. Inhibiting SIRPα on donor cells without anti-Trp1 causes a moderate level of eating, suggesting non-specific opsonizing signals in this immunocompetent C57 model to be consistent with previous studies (Wang *et al.*, 2013). Interestingly, A'PB MΦ shows the greatest donor accumulation in tumors (**Fig. 5.1D**), which approximates recipient macrophage numbers in untreated tumors. Furthermore, a plot of donor MΦ abundance as a function of the %-phagocytic MΦ shows that higher phagocytic activity strongly correlates with more tumor infiltration (**Fig. 5.1E**). The results thus suggest an "engorge and accumulate" mechanism in this syngeneic orthotopic tumor model, which was previously shown in human A549 tumor xenografts in NSG mice.

Tumor depletion of B16F10 cells by A'PB MΦ was assessed by the percent of Trp1 positive cells remaining in the tumor after 10 days post cell injection. Flow cytometry confirms that A'PB MΦ treated tumors had a reduction in Trp1 positive B16F10 cells (2%) whereas tumors treated with anti-Trp1 only were composed of ~35% (**Fig. 5.1G**). Indeed, multiple A'PB MΦ treated tumors had a 10-fold decrease in Trp1 expressing B16F10 cells compared to anti-Trp1 only and untreated tumors which were composed of 30% B16F10 cells (**Fig. 5.1F**). Despite anti-Trp1 increasing phagocytosis of recipient TAMs (**Fig. 5.1C**), this alone seems insufficient to deplete B16F10 tumor cells. This suggests two possible outcomes: (i) recruitment of adaptive immune cells may be necessary for sufficient B16F10 depletion and TAMs are poor activators or (ii) a high

level of phagocytosis is required to significantly disrupt B16F10 tumor growth with macrophages alone.

Figure 5.1. Donor macrophages phagocytose and accumulate in syngeneic melanoma tumors causing depletion of Trp1 positive cancer cells

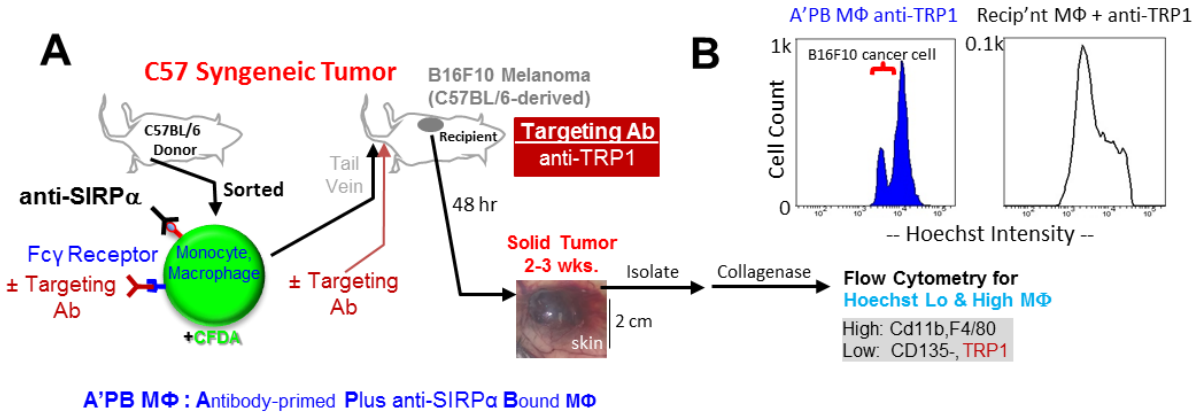

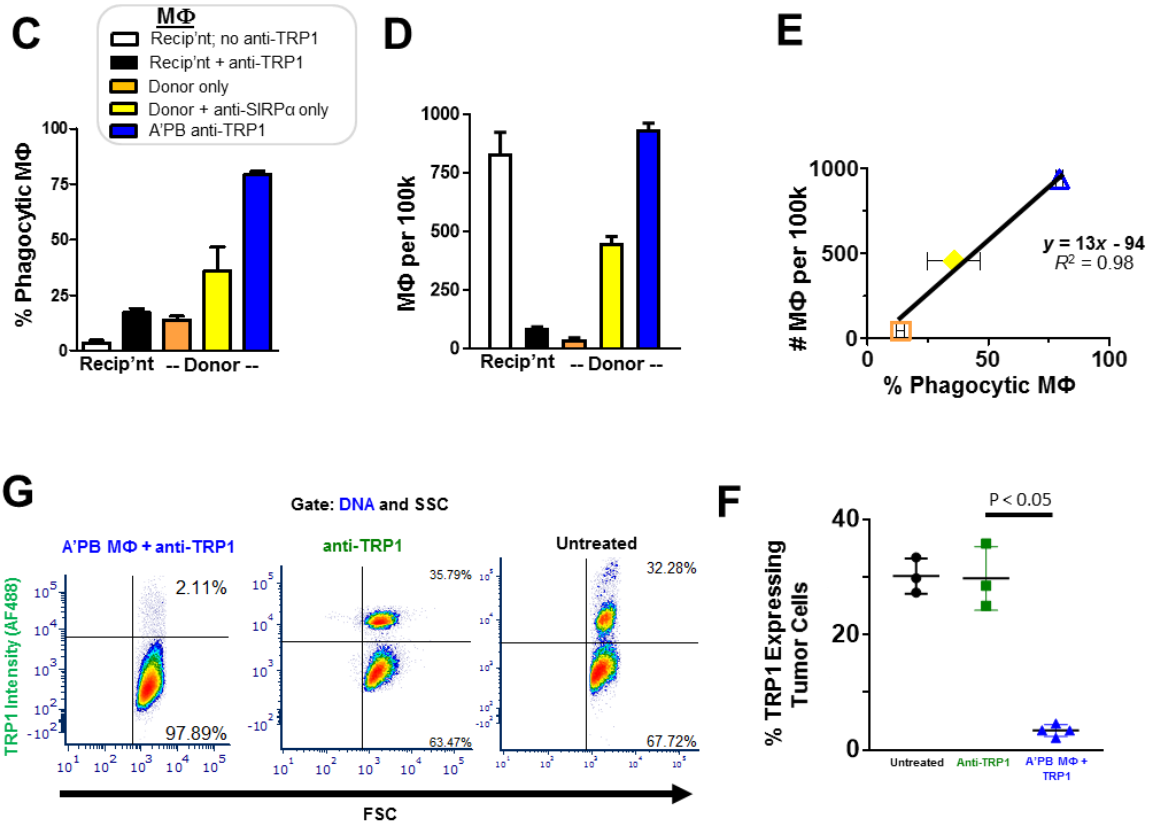

Figure 5.1. Donor macrophages phagocytose and accumulate in syngeneic melanoma tumors causing depletion of Trp1 positive cancer cells. (**A**) C57 mice with established melanoma tumors (B16F10) received tail-vein injections of SIRPα inhibited C57 donor marrow macrophages that were CFDA labeled. Mice also received tail-vein injections every other day of targeting antibody, anti-Trp1 (APB MΦ). In some experiments, Fc receptors on donor macrophages were primed with targeting Ab prior to cell injection (A'PB MΦ). (**B**) After anti-Trp1 Ab injection on day 2, mice were sacrificed ~2 hours later, and tumors were disaggregated for flow cytometry. Hoechst intensity for tumor-isolated donor A'PB MΦ and recipient TAM after anti-Trp1 injection shows two populations with the Hoechst-high macrophages shifted from Hoechst-low macrophages by an intensity equivalent to one B16F10 cancer cell, consistent with phagocytosis. (**C-D**) Hoechst high macrophages isolated from B16F10 tumors give % phagocytic MΦ among the total number of macrophages per 10^5 tumors cells ($n \geq 4$ tumors). (**E**) Plotting Donor macrophages accumulation as a function of phagocytic activity. (**F-G**) Flow cytometry analysis of B16F10 Trp1 expressing cells in disaggregated orthotopic B16F10 tumors. Analysis includes all non-aggregated cells that stain for Hoechst. Tumors were isolated when control mice reached $100mm^2$ ($n \geq 3$).

Donor macrophages reduce the growth of orthotopic melanoma and lung metastasis

To assess whether A'PB MΦ could impact B16F10 tumor growth, marrow cells engineered with SIRPα block and anti-Trp1 were sorted into a fraction of non-phagocytes (eg. lymphocytes) with DCs and a fraction of monocytes/macrophages. These cells were tail-vein injected at day 13 into mice with established tumors (10 mm^2 area). Sorted A'PB MΦ considerably delayed growth for 10 days compared to untreated mice and mice treated with non-phagocytes plus DCs (with SIRPα inhibition and anti-Trp1), which showed no effect on tumor growth (**Fig. 5.2A**). Marrow DCs are far less abundant than marrow MΦ's (by ~50-fold), and so it is possible that more DCs could impact tumor growth (*via* T-cells) as observed elsewhere (Liu *et al.*, 2015). Post treatment survival curves show A'PB MΦ significantly increases the survival of challenged mice compared to non-phagocytes plus DCs, anti-Trp1 only, and untreated mice which only survived ~7 days post treatment (**Fig. 5.2B**). Interestingly, ~50% of tumors treated with sorted A'PB MΦ completely regressed and never reappeared 30+ days after treatment.

Though A'PB MΦ can significantly reduce the growth of primary orthotopic melanoma tumors, metastasis is often the cause of death in most cancers. To evaluate A'PB MΦ effect on metastatic melanoma, lungs were isolated from mice challenged with melanoma at day 15 and 22 post challenge. Almost all A'PB MΦ treated mice had no lung metastasis at 22 days post challenge when treated with 20M cells, whereas anti-Trp1 only and untreated mice had ~15 melanoma lung nodules at day 15 post challenge (**Fig. 5.2C, 5.S2**). Reducing A'PB MΦ dose to10M cells, a standard adoptive T-cell injection (Garcia-Hernandez *et al.*, 2010; Sample *et al.*, 2008; Zoon *et al.*, 2015), still resulted in significant

reduction in melanoma lung nodules though more nodules were present than when treated with 20M cells.

In addition to efficacy, safety is a concern whenever inhibiting MΦ recognition of 'self' based on past findings that systemic injections of anti-CD47 rapidly clear some blood cells (Weiskopf *et al.*, 2013; Willingham *et al.*, 2012) and can lead to an adaptive immune response (Yi *et al.*, 2015). Blood was therefore drawn periodically from treated mice. Blood was isolated one and five days before treatment to establish pretreatment variation in blood profiles then again at day 11 and 14 (**Fig. 5.S2**). Along with blood collection, mice were observed 3 times a week for signs of anomalous mouse behavior (there were none). RBC count, hemoglobin levels, percent hematocrit, and platelet count all remained within the normal range for all treated mice at 4 days post treatment (**Fig. 5.2D**). There was a notable decrease in WBC for A'PB MΦ treated mice which may reflect A'PB MΦ ability to recruit other immune effector cells to tumors. When blood parameters are compared to pretreatment no significant change was observed (**Fig. 5.2S**). Furthermore, no mouse showed signs of weight change (**Fig. 5.2A, inset**) or acute signs of graft vs host disease (GvHD: weight loss, rough fur, and hair loss on face or rear) attributable to donor lymphocytes (Ali *et al.*, 2012; Hartung *et al.*, 2003; King *et al.*, 2009) over the 30+ days post injection. These results indicate that the engineered donor macrophages are the primary marrow effector cell and appear to be safe.

Figure 5.2. Donor macrophages reduce the tumor growth of orthotopic and lung metastasis of melanoma

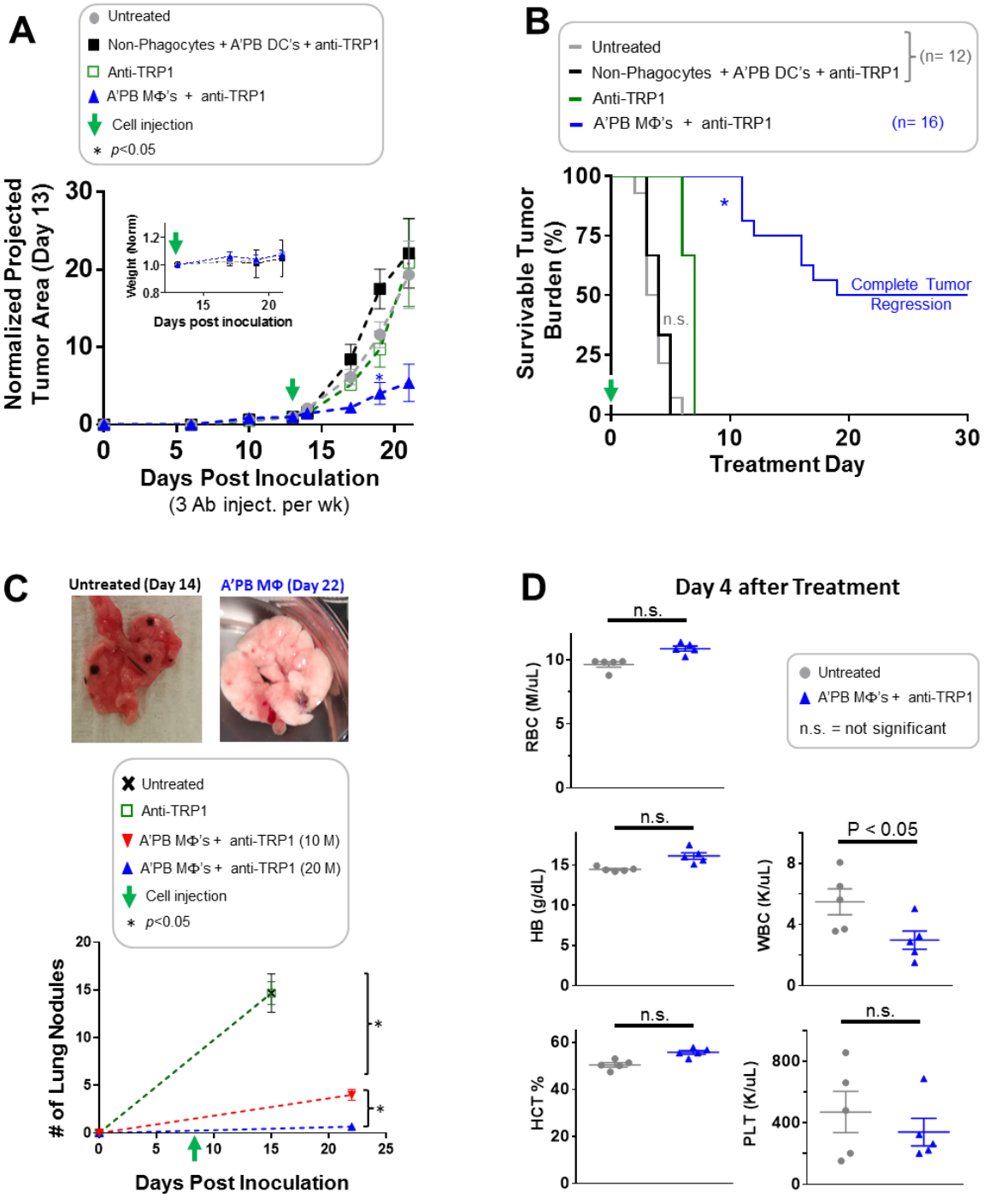

Figure 5.2. Donor macrophages reduce the tumor growth of orthotopic and lung metastasis of melanoma. Mice were challenged with $2x10^5$ orthotopic B16F10 tumor cells and allowed to grow until palpable (5-10 mm^2) before treated. Tumor growth was measured by calipers and normalized to individual tumors at treatment day. (**A**) On treatment day, mice received tail-vein injection of sorted MDM cells (10M sorted cells per mouse). Tumor growth was significantly delayed only with the A'PB MΦ fraction and not with the marrow DC fraction. (**Inset**) Weight measurements are normalized to the time of donor injection, and monitoring also proved negative for acute symptoms of GvHD: fur loss, hunched posture, and changes in activity ($n \geq 6$). (**B**) Kaplan-Meier curve for survivable B16F10 tumor burden in C57 mice. A tumor larger than 100 mm^2 was considered terminal as our IACUC does not allow death by tumor burden and recommends euthanization. The plateau for A'PB MΦ treated mice (blue line, treatment day 18+) indicates complete tumor regression ($n \geq 12$). (**C**) Number of lung nodules in C57 mice challenged with $5x10^5$ non-aggregated B16F10 cells. Mice were treated with A'PB MΦ anti-Trp1 at day 8 post challenge followed by lung isolation on day 15 and 22. Mice received 3 anti-Trp1 injections per week after treatment started ($n \geq 3$). (**D**) Blood profiles from C57 mice challenged with $2x10^5$ non-aggregated B16F10 cells. Mice started treatment on day 10 post challenge followed by injection of anti-Trp1 on day 11 and 13 ($n = 5$).

Donor macrophages initiate initial shrinkage, but acquired immunity is necessary for long-term tumor regression

To determine whether T-cells contribute to shrinkage of syngeneic tumors within 2 days of treatment as concluded recently from injections of anti-mCD47 without opsonizing Ab (Liu *et al.*, 2015), CD4 and CD8 T-cells were depleted prior to tail-vein injection of A'PB MΦ. Surprisingly, depletion of T-cells lacked any significant effect on tumor shrinkage for 6+ days after treatment (**Fig. 5.3A**) and no systemic toxicity from either T-cell depletion nor treatment with A'PB MΦ was observed (**Fig. 5.3A, inset**). This is consistent with little to no activation of T-cells by MDMs upon inhibiting mCD47 as concluded in the same studies (Liu *et al.*, 2015). Therefore, the initial effector cell again seems to be the A'PB MΦ, but after day 18 a significant difference in tumor size was observed between T-cell depleted mice and control mice treated with A'PB MΦ (**Fig. 5.3A**). To address whether T-cells are important for long-term tumor regress, tumor survival was compared between the two treatment groups. Indeed, all T-cell depleted mice died within 12 days after treatment. Although this was significantly longer survival than untreated mice, which had a max survival of 5 days, mice treated with A'PB MΦ with no T-cell depletion had 50% of all tumors completely regress for 30+ days post treatment (**Fig. 5.3B**). This suggests that not only is A'PB MΦ phagocytosis important for acute tumor shrinkage, but may also be efficient at presenting and activating T-cells for long-term tumor regression when compared to TAMs.

To ensure that an acquired immune response against B16F10 contributes to long-term regression, mice treated with A'PB MΦ that had complete regression (cured) were re-challenged with $2x10^5$ B16F10 cells 100 days after the start of treatment. No

measurable tumor growth occurred in cured mice until day 26 post challenge whereas control mice had measurable growth at day 5 (**Fig. 5.3C**). Tumor analysis of cured mice that were re-challenged shows depletion of Trp1 positive B16F10 similar to initial treatment with A'PB MΦ (**Fig. 5.3D**). This suggests that A'PB MΦ treated mice develop acquired immunity against Trp1 expressing cancer cells and possibly other neoantigens expressed in B16F10. However, negative selection against these antigens leaves cancer cells that are unable to be cleared by the immune system leading to eventual tumor growth. Taken together, A'PB MΦ macrophages, not TAMs, can shrink tumors and initiate an acquired immune response which is necessary for complete regression of orthotopic melanoma tumors.

Figure 5.3. Donor macrophages initiate initial shrinkage, but acquired immunity is necessary for long-term tumor regression

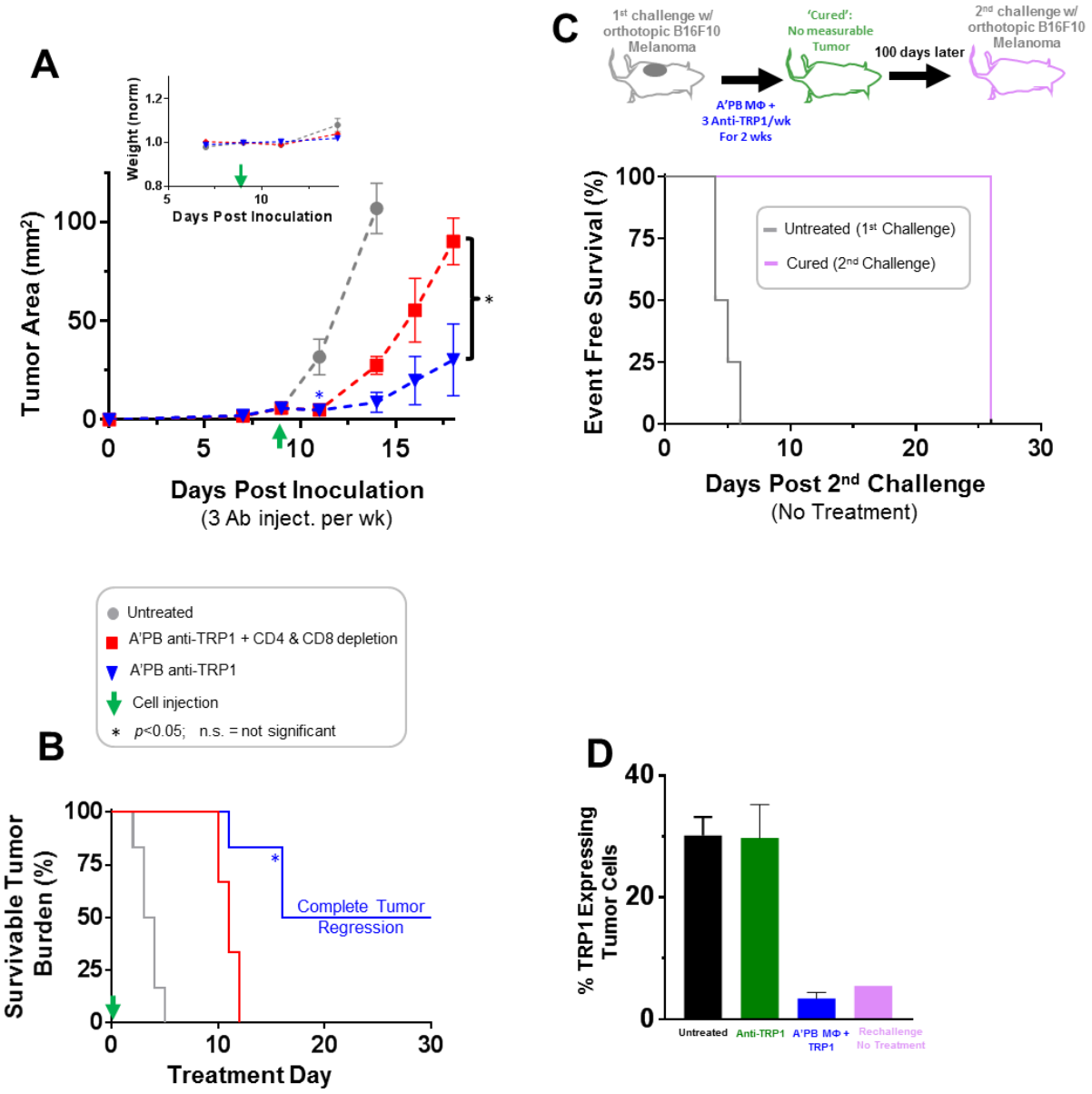

Figure 5.3. Donor macrophages initiate initial shrinkage, but acquired immunity is necessary for long-term tumor regression. (**A**) At day-9, donor marrow cells (20M; ~half are MΦ) prepared as A'PB MΦ were tail-vein injected. CD4 and CD8 T-cells were depleted with biweekly (IP) injection of anti-CD4 and anti-CD8 Abs beginning at the time of donor cell injection ($n \geq 6$). (**Inset**) Weight measurements are normalized to the time of donor injection, and monitoring also proved negative for acute symptoms of GvHD: fur loss, hunched posture, and changes in activity ($n \geq 6$). (**B**) Kaplan-Meier curve for survivable B16F10 tumor burden in C57 mice with T cell depletion. A tumor larger than 100 mm^2 was considered terminal as our IACUC does not allow death by tumor burden and recommends euthanization. The plateau for A'PB MΦ treated mice (blue line, treatment day 18+) indicates complete tumor regression. (**C**) Kaplan-Meier curve of event free survival of A'PB MΦ cured mice re-challenged with B16F10 tumor cells. Re-challenge started 100 days after initial treatment of A'PB MΦ. (**D**) Flow cytometry analysis of B16F10 Trp1 expressing cells in disaggregated orthotopic B16F10 tumors. Analysis includes all non-aggregated cells that stain for Hoechst. Tumors were isolated if B16F10 re-challenged tumors grew and reached 100mm^2.

5.4 DISCUSSION

A'PB MΦ alone can acutely shrink tumors without the need for T-cell activation, but T-cell recruitment and activation is necessary to prevent tumor recursion (**Fig. 5.3A**). Recent studies identified DCs as an important activator of T-cells with anti-CD47 treatment (Liu *et al.*, 2015). Here, SIRPα blocked, anti-Trp1 targeted DCs had no impact on tumor growth (**Fig. 5.2A-B**). This could reflect the aggressiveness of the melanoma model used or an insufficient dose of DCs as only 1% of all marrow cells are mature DCs. Regardless, T-cell influence on tumor shrinkage adds complexity in predicting cancer cell depletion solely by measuring MΦ phagocytosis (**Fig. 5.1C, 5.2A**) as injection of anti-Trp1 increases eating by TAMs, but has no impact on tumor growth (**Fig. 5.1F, 5.2B-C**). TAMs have proven to be weakly phagocytic (Rodriguez *et al.*, 2013) which could contribute to their poor activation of acquired immunity as a minimum phagocytic threshold may be required, or perhaps TAMs have low expression of key proteins involved in presentation (i.e. MHCII). Unlike TAMs, undifferentiated SIRPα inhibited marrow macrophages can initiate an acquired immune response, leading to sustained primary tumor regression (**Fig. 5.3B-D**). Interestingly, SIRPα inhibition of MDMs without addition of anti-Trp1 significantly increased phagocytosis compared to MDMs without SIRPα blocking (**Fig. 5.1C**). This suggests non-specific opsonizing signals in this immunocompetent C57 model which is consistent with previous studies (Wang *et al.*, 2013) rather than opsonization from dissociating SIRPα blocking antibodies. Though B16F10 cells have high SIRPα expression (**Fig. 5.S1**), it unlikely that 5 μg of SIRPα blocking antibody (amount added to cells before washout) has any opsonizing effect as recent studies show injection of 200 μg of this antibody given 3 times a week for 2 weeks

(1200 µg, ~240-fold more) only reduces tumor growth by 50% (Yanagita *et al.*, 2017). Regardless, addition of anti-Trp1 to A'PB MΦ can also greatly reduce lung metastasis of melanoma at 22 days post challenge, with almost no melanoma lung nodules detected across numerous mice and experiments (**Fig. 5.2C, 5.S2**).

Along with being efficacious, A'PB MΦ had no detectable impact on mouse health which resulted from phagocytosis of melanoma cells or activation of acquired immunity. Blood profiles, body weight (**Fig. 5.2A, 5.2D, 5.3A, 5.S2**), and close observation of mouse activity for development of GvHD all suggest a degree of safety to the overall approach. In comparison, systemic injection of anti-CD47 causes reproducible decreases in blood cells and platelets as well as increased reticulocytes (Oldenborg *et al.*, 2002; Weiskopf *et al.*, 2013; Willingham *et al.*, 2012), which are all a consequence of ubiquitous expression of CD47 and perhaps some level of opsonization of these components. Careful attention to species specificity of anti-CD47 is, of course, needed in such studies (Subramanian *et al.*, 2006; Tsai & Discher, 2008), but CD47 blockade in a clinical setting is expected to sensitize all healthy cells to clearance by MΦ. Increased reticulocyte production may mask the loss of RBCs at late time points, reinforcing the need for blood collection at early and late time points (Yanagita *et al.*, 2017). Although reticulocytes may compensate for the loss of RBCs, increased clearance by phagocytes can lead to auto immunity against RBCs, causing severe anemia (Oldenborg *et al.*, 2002). The findings here thus provide insight into macrophage dependent shrinkage of tumors and illustrate the role T-cells play. Furthermore, SIRPα inhibited marrow macrophages can efficiently and safely activate acquired immunity against syngeneic melanoma tumors.

5.5 SUPPLEMENT

Figure 5.S1. Antibody binding and protein profiles in B16F10 cancer cells

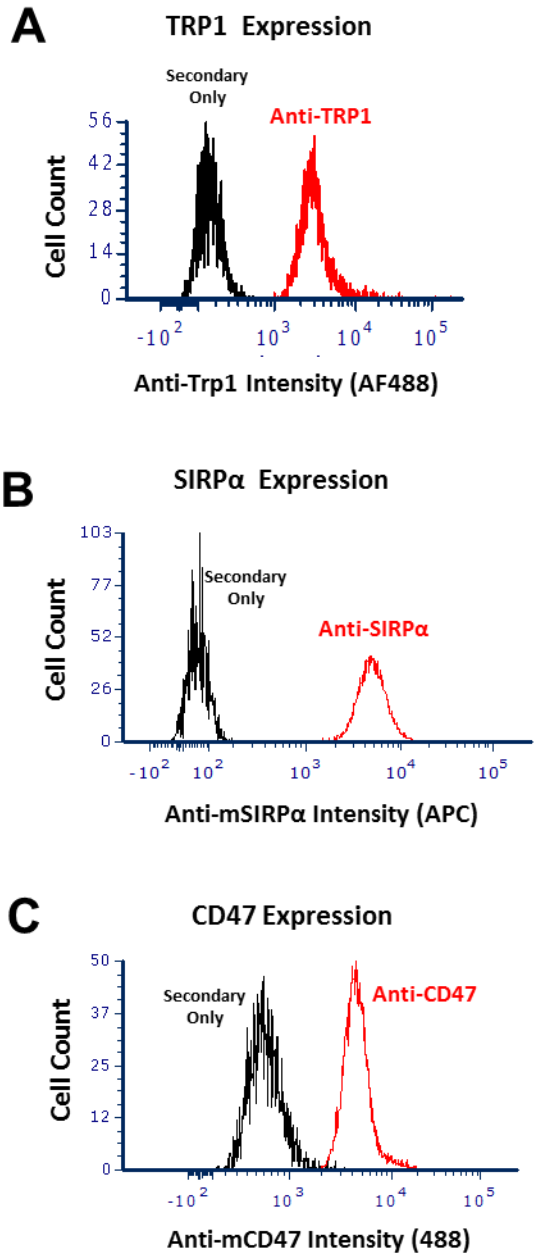

Figure 5.S1. Antibody binding and protein profiles in B16F10 cancer cells. (**A**) Verification of anti-Trp1 binding to disaggregated orthotopic B16F10 tumors in C57 mice. Histogram is composed 5k B16F10 cells for each condition with ~10-fold intensity shift. (**B-C**) mSirpα and mCd47 expression and antibody binding.

Figure 5.S2. Safety and efficacy of A'PB MΦ treatments in mice with lung melanoma metastasis

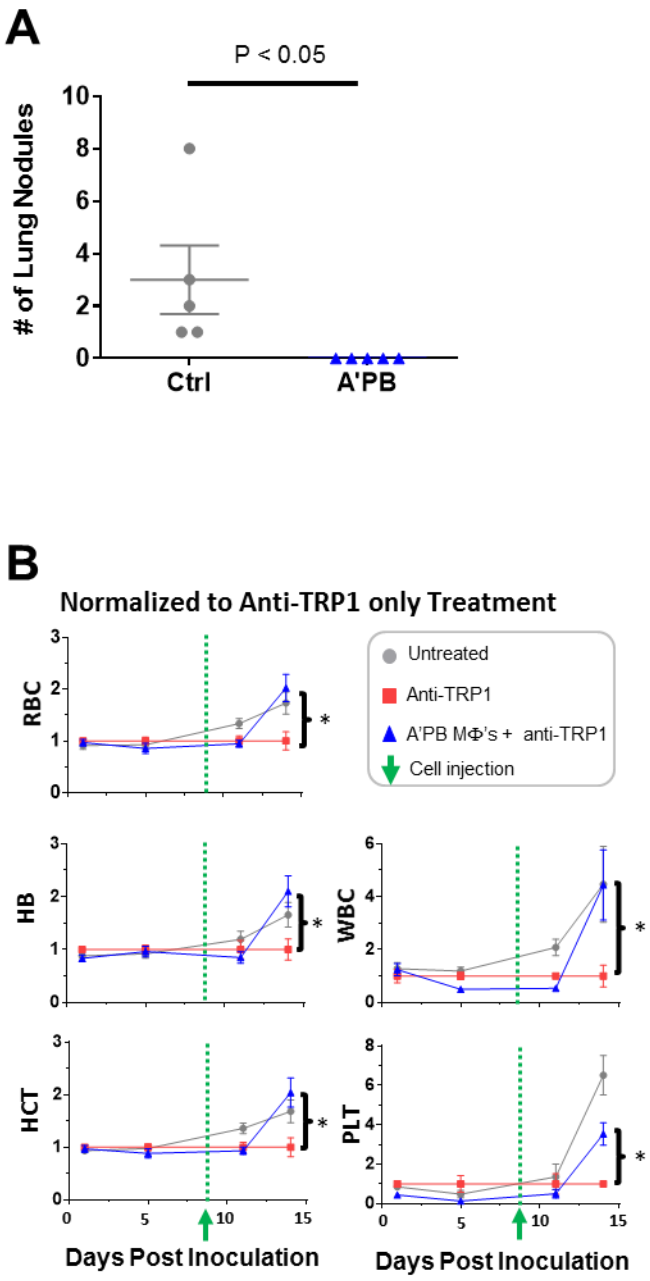

Figure 5.S2. Safety and efficacy of A'PB MΦ treatment in mice with lung melanoma metastasis. (**A**) Number of lung nodules in C57 mice challenged with $2x10^5$ non-aggregated B16F10 cells. Mice were treated with A'PB MΦ anti-Trp1 at day 10 post challenge followed by lung isolation on day 14. Mice received additional antibody injections on day 11 and 13 (n = 5). (**B**) Blood profiles from C57 mice challenged with $5x10^5$ non-aggregated B16F10 cells. Each parameter is normalized to mice treated with anti-Trp1 only. Mice started treatment on day 8 post challenge followed by every other day injection of Trp1 antibody ($n \geq 3$).

Chapter 6: Conclusions and Future Work

This dissertation provides evidence that at least three features of a macrophage must be optimized for efficient engulfment of cancer cells *in vivo*. First, the phagocytic potential must be considered. Prior to this dissertation TAMs were thought to be sufficient at controlling tumor growth with anti-CD47 treatment and in some studies requiring an additional opsonization antibody (Gholamin *et al.*, 2017; Weiskopf *et al.*, 2013; Willingham *et al.*, 2012). Here we found that even with >80% KD of CD47 and high opsonization, TAMs can only shrink tumors by 20% over 1-2 weeks compared to a A'PB MΦ shrinkage of 50% in 10 days. We conclude that the difference in phagocytic potential between marrow macrophages and TAMs is caused by a 10-fold higher expression of SIRPα in TAMs. However, changes in other proteins important for phagocytosis could be occurring as well. Future work should focus on isolating TAMs, then inhibiting or knocking down SIRPα followed by phagocytosis assays comparing TAMs and marrow macrophages. If marrow macrophages continue to have a higher phagocytic index, then it would suggest that other mechanisms, in addition to high SIRPα, cause TAMs to be poor eaters.

The second parameter that should be considered for a macrophage anti-cancer therapy is CD47-SIRPα inhibition. Anti-SIRPα antibodies can enhance phagocytosis of opsonized targets by immobilizing SIRPα (by crosslinking *cis* homodimers (Lee *et al.*, 2010)), and thereby limiting SIRPα accumulation into the phagocytic synapse (**Fig. 4.S1**). In recent *in vitro* experiments using THP-1s and human RBCs, we have found macrophages to be more efficient at eating CD47 expressing targets when plated on extremely stiff surfaces (**Fig. 6.1A**). On softer, more biologically relevant matrixes, phagocytosis is independent of matrix stiffness. When CD47-SIRPα signaling is inhibited

phagocytosis across all degrees of stiffness becomes equivalent (**Fig. 6.1B**). This suggests that CD47-SIRPα signaling is hindered when macrophages are plated on extremely stiff matrix. Staining of SIRPα on macrophages shows that SIRPα increases with increasing surface stiffness as previously shown (**Fig. 6.1C**). However, a minimal increase in SIRPα is found between the highest biologically relevant matrix and plastic (extremely stiff). Given these data, we hypothesis that SIRPα motility decreases with increasing matrix stiffness, likely reducing phagocytic synapse accumulation and preventing recognition of CD47. To compensate, macrophages increase surface expression of SIRPα, but this upregulation of SIRPα has a maximum. When macrophages are plated on plastic, a relatively small increase in SIRPα occurs which does not compensate for a relatively large decrease in SIRPα motility. Future work will verify this hypothesis using FRAP analysis to quantify SIRPα motility when macrophages are plated on matrices with a range of stiffness.

Lastly, a cancer cell should be specifically opsonized for sufficient engulfment by macrophages to occur. A single antibody, such as anti-CD47, has been proposed to both inhibit 'self' signaling and to also efficiently opsonize a cancer cell (Willingham *et al.*, 2012), but this has become a subject of concern in terms of replication and statistical significance (Horrigan *et al.*, 2017). In this dissertation, SIRPα inhibition of MDMs without addition of anti-Trp1 in immunocompetent mice significantly increased phagocytosis compared to MDMs without SIRPα blocking (**Fig. 5.1C**). This suggested that non-specific opsonizing signals in this immunocompetent C57 model which was consistent with previous studies (Wang *et al.*, 2013), rather than opsonization from dissociating SIRPα blocking antibody. Other studies have proposed that calreticulin,

which is highly expressed on apoptotic and cancerous cells, is sufficient to drive eating with anti-CD47 inhibition (Chao *et al.*, 2010; Feng *et al.*, 2015; Gardai *et al.*, 2005). However, the consensus from researchers, and the conclusion of this dissertation, is that additional antibody opsonization is required. Use of human-specific antibodies that target human cancers in mice yield relatively low off-target toxicity (i.e. antibodies against hRBC, hMucin-1, and hEGFR). However, finding antibodies that target mouse cancers in mice or human cancers in human that do not produce toxic side effects with donor macrophage therapy is challenging. Emerging RNA sequencing technology will be critical at developing personalized medicine where a patient's neoantigens are identified and appropriate antibodies are selected. Future work will utilize the metastatic B16F10 tumor model to study DNA damage that occurs at primary and metastatic tumor sites. We will focus on DNA damage that occurs as a cancer cell travels in the blood and whether damage at these two sites cause new neoantigens to develop.

Given these 3 requirements, this dissertation has shown that SIRPα inhibition combined with adoptive macrophage therapy using marrow-derived macrophages is an effective approach for shrinking primary solid tumors. A'PB MΦ were also shown to greatly reduce lung metastasis of melanoma, as 22 days post challenge almost no melanoma lung nodules were detected across numerous mice and experiments (**Fig. 5.2C, 5.S2**). Using tumor growth to evaluate macrophage based therapies is useful, but profiling macrophages directly from tumors has revealed additional information which was previously unknown. In this dissertation, macrophage phagocytosis of tumor cells *in vivo* measured at the single cell level predicted initial rates of tumor shrinkage. Donor macrophages proved to be more effective at phagocytosing cancer cells than TAMs, and

accumulate in tumors in various tissues based on their phagocytic potential. This method of analyzing macrophages builds on past studies that use clodronate, which depletes phagocytic cells, or tissue staining for F4/80 abundance to implicate a role for macrophages as the primary effector cell (Gholamin *et al.*, 2017; Wang *et al.*, 2013). However, clodronate causes high variability in tumor growth, making statistical analysis difficult and using one simple surface marker to distinguish macrophages from the 10-20 different cell types in a tumor is unreliable at best. Our single cell analysis also gave us insight into macrophage differentiation. Previous studies concluded that anti-CD47 treatment enhanced eating by macrophages and drove them to an M1 phenotype (Zhang *et al.*, 2016). The studies conducted here suggest that no matter the phagocytic potential of a macrophage, prolonged residency in stiff tumors drives differentiation towards SIRPα high, non-phagocytic, tumor promoting macrophages (**Fig. 4.4B-F, 4.S5**). It is likely that anti-CD47 antibody treatments lead to recruitment of circulating monocytes into tumors which would have a higher M1/M2 ratio rather than directly converting TAMs into a phagocytic phenotype.

Though this dissertation implicates microenvironment stiffness of tumors as a contributor to macrophage differentiation, phagocytosis could also be involved as it is a mechanically intensive process which causes similar cytoskeleton stress. Phagocytosis is favored by the stiffness of a cell or particle, and myosin-II has again been shown to be key (Sosale *et al.*, 2015; Tsai & Discher, 2008). Myosin-II thus has a vital role in multiple, cytoskeletal-intensive activities of macrophages which could control differentiation. Intuitively, it seems possible that nature has designed macrophages to negatively regulate phagocytosis to prevent off-target eating and autoimmune response from presentation of

‘self’ antigens. Future work will focus on the relationship between phagocytosis and differentiation by setting up time dependent phagocytosis experiments followed by M1/M2 staining and RNA Sequencing.

Understanding factors that influence macrophage differentiation is currently a hot topic and a major hurdle for donor macrophage therapy which is thoroughly studied in this dissertation. RNAi knockdown of SIRPα seems like an obvious approach to prevent differentiation of macrophages to non-phagocytic TAMs, but SIRPα-knockdown macrophages can enhance tumor growth *in vivo* (Pan *et al.*, 2013). Staining of M1/M2 markers and SIRPα on differentiating donor MΦ shows simultaneous upregulation of SIRPα and M2 marker. Unfortunately, a causal relationship cannot be established between SIRPα and macrophage differentiation given the data in this dissertation. Future work should consider the transcriptional changes that occur in macrophages with SIRPα knockdown or overexpression and how it affects macrophage differentiation, and maybe even migration, as TAMs seemed to migrate less than marrow macrophages (**Fig. 4.S4**).

It is well established that phagocytes are highly motile, but whether macrophage migration could be inhibited by phagocytosis of cancers was unknown. Marrow-derived macrophages from mouse (NSG) or human infiltrated large solid tumors and accumulated proportionally to their engulfment of cancer cells (**Fig. 4.1B-F, 4.S6**). In solid tumors of low porosity, immobilization can in part be due to an inability to ‘eat and run.’ The stiffness of the nucleus is well-known to hinder migration (Harada *et al.*, 2014; Shin *et al.*, 2013; Thiam *et al.*, 2016). Therefore, it is unsurprising that a macrophage with two nuclei (one from the cancer cell and one of its own) has difficulty migrating. However, engulfment of two nanobeads significantly reduced 3D migration through much larger

micro-pores (**Fig. 4.2B-E**). This suggests an antagonism exists between phagocytic and migratory pathways in macrophages, which has already been proposed for very primitive cells such as *Dyctiostilium* amoeba (Veltman *et al.*, 2014) and fly haemocytes (Evans *et al.*, 2013), as well as dendritic cells (Chabaud *et al.*, 2015). We hypothesize that this antagonism causes competition between overlapping proteins involved in cytoskeleton components such as ARP2/3 or Myosin II wherein the proteins are sequestered by the dominate function, phagocytosis. Future work should focus on identifying the overlapping proteins and use live imaging during migration eating experiments to confirm protein reallocation from migration to phagocytosis.

The "engorge and accumulate" mechanism for engineered donor macrophage in solid tumors adds an additional safety component to this therapy as it minimizes accumulation of engineered macrophages in other tissues (**Fig. 4.1G, 4.S3**). Throughout this dissertation, there was no detectable impact on mouse health resulting from the numerous donor cell injections that drive tumor phagocytosis and shrinkage (**Fig. 4.5C, 4.S6**) even in immunocompetent mice where T-cells were activated against melanoma cells (**Fig. 5.2A, 5.2D, 5.3A, 5.S2**). Subsequent injections of marrow cells remain effective and safe (**Fig. 4.5C, 4.S6**), and it is worth noting that multiple injections of marrow and leukocytes are already done in the clinic (Eapen *et al.*, 2004). Our approach of adding SIRPα blocking antibody directly to monocyte/macrophage *ex vivo* greatly reduces the amount of blocking antibody required compared to systemic injections of anti-CD47 or anti-SIRPα aiming to block 'self' on tumor cells. Furthermore, most of the engineered marrow cells injected are monocytes which may require tissue residency to differentiate into phagocytic macrophages and, therefore, are unable to eat RBCs they

encounter in circulation. Once monocytes infiltrate a tissue (likely the tumor, according to our research), strong opsonization toward cancer cells directs them to phagocytose tumor cells rather than RBCs. In comparison, systemic injection of anti-CD47 causes blockade of CD47 on blood cells and platelets (Oldenborg *et al.*, 2002; Weiskopf *et al.*, 2013; Willingham *et al.*, 2012) leading to clearance by splenic and liver macrophages which normally screen the blood for foreign cells. Our CD47 knockdown studies document selective eating of cells with low CD47, enriching for CD47-high cancer cells (**Fig. 4.3C-D, 4.S4**). Therefore, older RBCs with less CD47 are likely cleared first. This can also explain why cancer patients have CD47-high cancer cells (Willingham *et al.*, 2012) and oncogenes that drive CD47 expression are favored (Casey *et al.*, 2016). Careful attention to species specificity of anti-CD47 is, of course, needed in all safety studies (Subramanian *et al.*, 2006; Tsai & Discher, 2008) as CD47 blockade in a clinical setting is expected to sensitize all healthy cells to phagocytosis by macrophages. Acute depletion of RBCs can be compensated with erythropoietin injection or blood transfusion, but autoimmune concerns exist leading to chronic anemia as IgG against mouse RBCs is observed in preclinical models (Oldenborg *et al.*, 2002). Therefore, understanding activation of acquired immunity by macrophages is an important area of study not only for chronic autoimmune diseases, but cancer therapy.

This dissertation has shown that A'PB MΦ alone can acutely shrink tumors without the need for T-cell activation in immune incompetent and competent mice that are T-cells depleted. However, T-cell recruitment and activation is necessary to prevent tumor recursion (**Fig. 5.3A**). Recent studies identified DCs as an important activator of T-cells with anti-CD47 treatment (Liu *et al.*, 2015). Here, SIRPα blocked, antibody targeted

DCs had no impact on tumor growth. This could have reflected the aggressiveness of the tumor models used, or an insufficient dose of DCs, as only 1% of all marrow cells are mature DCs. Regardless, T-cell influence on tumor shrinkage added complexity in predicting cancer cell depletion solely by measuring macrophage phagocytosis. TAMs have proven to be weakly phagocytic (Rodríguez *et al.*, 2013) which could have contributed to their poor activation of acquired immunity (Liu *et al.*, 2015), as a minimum phagocytic threshold may be required, or perhaps TAMs have low expression of key proteins involved in presentation (i.e. MHCII). Unlike TAMs, undifferentiated SIRPα inhibited marrow macrophages could initiate an acquired immune response leading to sustained primary tumor regression (**Fig. 5.3B-D**). However, the understanding of T-cell activation by macrophages reached in this dissertation is incomplete (chapter 5).

Our immediate work will be directed towards proving donor macrophages not only activate T-cells, but are more efficient than TAMs. The re-challenge experiment conducted in this dissertation is unfinished and should be replicated with more mice (**Fig. 5.3C, D**). If successful, we would identify which B16F10 antigens T-cells are targeting. Based on the depletion of Trp1 expressing cells in re-challenged mice, we are concerned that T-cells are only being developed against Trp1. Therefore, we plan to knockout Trp1 in B16F10 and create mosaic tumors, then treat with A'PB MΦ targeting Trp1. Since A'PB MΦ selectively phagocytosis opsonized cells, Trp1 knockout cells should be unaffected by macrophages. If 60% (% regression observed in WT B16F10 tumors) of tumors continue to regress it would suggest that T-cells are targeting different antigens beside Trp1, and confirms that other immune cells must be involved as macrophages are unable to clear Trp1 knockout cells. Once T-cell activation by donor macrophages is

verified, these experiments will be repeated using TAMs as a source of donor cells to study their ability to initiate an acquired immune response.

The findings in his dissertation thus provide insight into the mechanisms, utility, and safety of engineering (*i*) a highly phagocytic and motile macrophage, with (*ii*) inhibition of 'self' signaling by anti-SIRPα, combined with (*iii*) robust target opsonization.

Figure 6.1. Matrix stiffness inhibits SIRPα motility

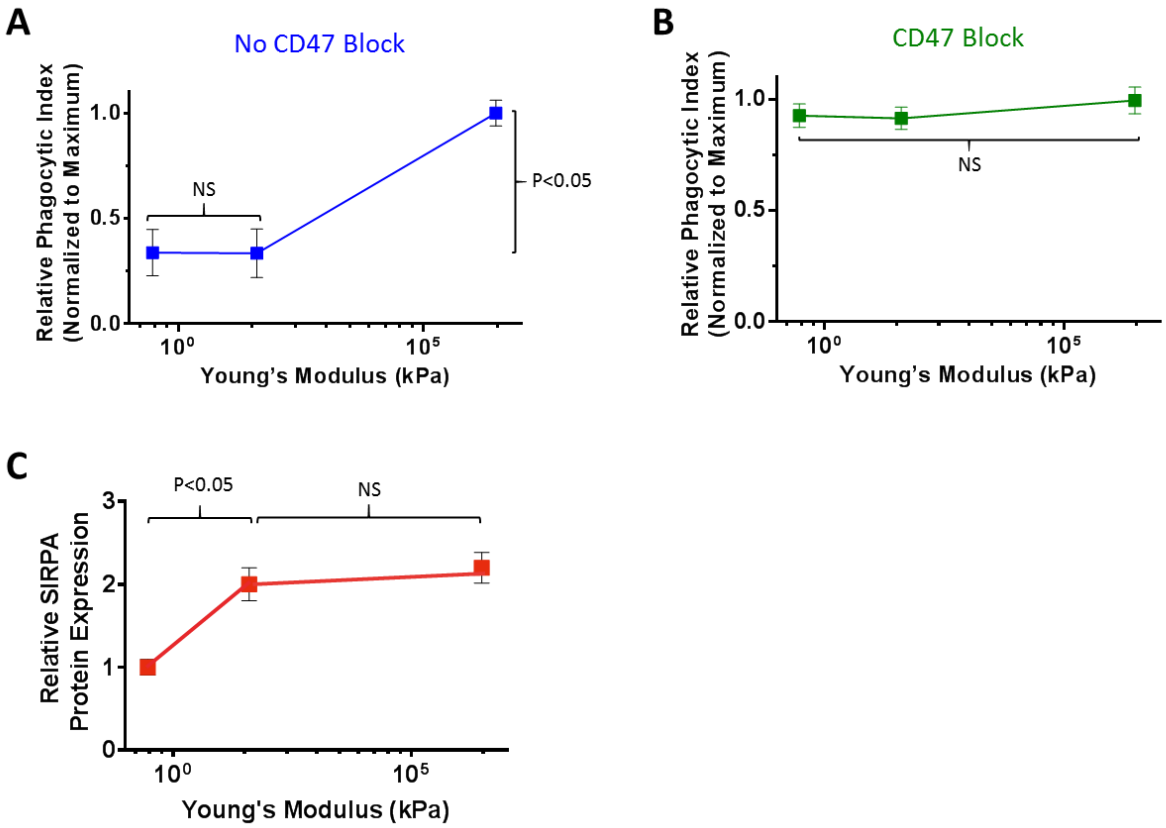

Figure 6.1. Matrix stiffness inhibits SIRPα motility. Phagocytosis assay using a THP-1 cell line co-cultured with opsonized human RBCs for 30 mins on gels with varying stiffness. (**A**) Normalized phagocytic index (Percent phagocytic THP-1s multiplied by the number of cells engulfed per THP-1) as a function of matrix stiffness without CD47 inhibition and (**B**) with CD47 inhibition. It appears THP-1s on very stiff matrix are more efficient at phagocytosis, but with CD47 inhibition THP-1 engulfment of RBCs is independent of matrix stiffness. (**C**) SIRPα staining of THP-1s on different degrees of stiffness. In a biologically relevant range of matrix stiffness SIRPα increases, but no significant difference is measured beyond this range.

BIBLIOGRAPHY

Aderem, A., & Underhill, D. M. (1999). Mechanisms of phagocytosis in macrophages. *Annual review of immunology*, *17*, 593–623.

Adlerz, K. M., Aranda-Espinoza, H., & Hayenga, H. N. (2016). Substrate elasticity regulates the behavior of human monocyte-derived macrophages. *European Biophysics Journal*, *45*(4), 301–309.

Alenghat, F. J., Baca, Q. J., Rubin, N. T., Pao, L. I., Matozaki, T., Lowell, C. a, … Swanson, K. D. (2012). Macrophages require Skap2 and Sirpα for integrin-stimulated cytoskeletal rearrangement. *Journal of cell science*, *125*(Pt 22), 5535–45.

Alexandrov, L. B., Nik-Zainal, S., Wedge, D. C., Aparicio, S. A. J. R., Behjati, S., Biankin, A. V, … Stratton, M. R. (2013). Signatures of mutational processes in human cancer. *Nature*, *500*, 415–421.

Ali, N., Flutter, B., Rodriguez, R. S., Sharif-paghaleh, E., Barber, L. D., Lombardi, G., & Nestle, F. O. (2012). Xenogeneic Graft-versus-Host-Disease in NOD-scid IL- 2R c null Mice Display a T-Effector Memory Phenotype. *PLoS ONE*, *7*(8), 1–10.

Ali, O. A., Emerich, D., Dranoff, G., & Mooney, D. J. (2009). In Situ Regulation of DC Subsets and T Cells Mediates Tumor Regression in Mice. *Science translational medicine*, *19*(8).

Alvey, C. M., & Discher, D. E. (2017). Engineering macrophages to eat cancer: from "Marker of Self" CD47 and phagocytosis to differentiation. *Journal of leukocyte biology*, *102*, 1–10.

Andreesen, R., Hennemann, B., & Krause, S. W. (1998). Adoptive immunotherapy of cancer using monocyte-derived macrophages: rationale, current status, and perspectives. *Journal of Leukocyte Biology*, *64*(October), 419–426.

Andreesen, R., Scheibenbogen, C., Brugger, W., Krause, S., Meerpohl, H. G., Leser, H. G., … Löhr, G. W. (1990). Adoptive Transfer of Tumor Cytotoxic Macrophages Generated in Vitro from Circulating Blood Monocytes: A New Approach to Cancer Immunotherapy. *Cancer Research*, *50*(23), 7450–7456.

ARCHAMBEAUD, I. (2016). Myeloid Derived Suppressor Cells Control by Signal Regulatory Protein-alpha: Investigation in Hepatocellular Carcinoma (MDScan). *Clinicaltrial.gov*.

Assarsson, E., Sidney, J., Oseroff, C., Pasquetto, V., Bui, H., Frahm, N., … Sette, A. (2007). A quantitative analysis of the variables affecting the repertoire of T cell specificities recognized after vaccinia virus infection. *The Journal of Immunology*, *178*, 7890–7901.

Bancaud, A., Huet, S., Daigle, N., Mozziconacci, J., Beaudouin, J., & Ellenberg, J. (2009). Molecular crowding affects diffusion and binding of nuclear proteins in heterochromatin and reveals the fractal organization of chromatin. *The EMBO Journal*, *28*, 3785–3798.

Bencherif, S. A., Warren Sands, R., Ali, O. A., Li, W. A., Lewin, S. A., Braschler, T. M., … Mooney, D. J. (2015). Injectable cryogel-based whole-cell cancer vaccines. *Nature Communications*, *6*(May), 7556.

Beningo, K. a, & Wang, Y. (2002). Fc-receptor-mediated phagocytosis is regulated by

mechanical properties of the target. *Journal of cell science*, *115*, 849–856.
Bogdanik, L., Lall, D., Wolf, A. J., Muhammad, A. K. M. G., Ho, R., Carmona, S., … Baloh, R. H. (2016). C9orf72 is required for proper macrophage and microglial function in mice. *sc*, *351*(6279).
Boyd, N. F., Guo, H., Martin, L. J., Sun, L., Stone, J., Fishell, E., … Yaffe, M. J. (2007a). Mammographic density and the risk and detection of breast cancer. *The New England Journal of Medicine*, *356*(3), 227–236.
Boyd, N. F., Guo, H., Martin, L. J., Sun, L., Stone, J., Fishell, E., … Yaffe, M. J. (2007b). Mammographic density and the risk and detection of breast cancer. *The New England journal of medicine*, *356*(3), 227–236.
Boyer, A., Andreu, G., Romet-Lemonne, J. L., Fridman, W. H., & Teillaud, J. L. (1999). Generation of phagocytic MAK and MAC-DC for therapeutic use: Characterization and in vitro functional properties. *Experimental Hematology*, *27*(4), 751–761.
Brown, E. J., & Frazier, W. A. (2001). Intergrin-associated protein (CD47) and its ligands. *Trends in Cell Biology*, *11*(3), 130–135.
Bruce, L. J., Ghosh, S., King, M. J., Mark Layton, D., Mawby, W. J., Stewart, G. W., … Tanner, M. J. A. (2002). Absence of CD47 in protein 4.2-deficient hereditary spherocytosis in man: An interaction between the Rh complex and the band 3 complex. *Blood*, *100*(5), 1878–1885.
Burgess, M. (2015a). A Phase 1, Dose Finding Study of CC-90002 in Subjects With Advanced Solid and Hematologic Cancers. *Clinicaltrial.gov*.
Burgess, M. (2015b). A Study of CC-90002 in Subjects With Acute Myeloid Leukemia (AML) and High-risk Myelodysplastic Syndrome (MDS). *Clinicaltrial.gov*.
Buxboim, A., Swift, J., Irianto, J., Spinler, K. R., Dingal, P. C. D. P., Athirasala, A., … Discher, D. E. (2014). Matrix elasticity regulates lamin-A,C phosphorylation and turnover with feedback to actomyosin. *Current Biology*, *24*(16), 1909–1917.
Carbone, D. P., Ciernik, I. F., Kelley, M. J., Smith, M. C., Nadaf, S., Kavanaugh, D., … Berzofsky, J. A. (2005). Immunization with mutant p53- and K-ras-derived peptides in cancer patients: Immune response and clinical outcome. *Journal of Clinical Oncology*, *23*(22), 5099–5107.
Casey, S. C., Tong, L., Li, Y., Do, R., Walz, S., Fitzgerald, K. N., … Felsher, D. W. (2016). MYC regulates the antitumor immune response through CD47 and PD-L1. *Science*, *53*(9), 1689–1699.
Chabaud, M., Heuzé, M. L., Bretou, M., Vargas, P., Maiuri, P., Solanes, P., … Lennon-Duménil, A.-M. (2015). Cell migration and antigen capture are antagonistic processes coupled by myosin II in dendritic cells. *Nature communications*, *6*(May), 7526.
Champion, J. A., & Mitragotri, S. (2006). Role of target geometry in phagocytosis. *Proceedings of the National Academy of Sciences of the United States of America*, *103*(13), 4930–4.
Chao, M. (2016). Trial of Hu5F9-G4 in Combination With Rituximab in Relapsed/Refractory B-cell Non-Hodgkin's Lymphoma. *Clinicaltrial.gov*.
Chao, M., Alizadeh, A., Tang, C., Myklebust, J. H., Varghese, B., Gill, S., … Majeti, R. (2010). Anti-CD47 antibody synergizes with rituximab to promote phagocytosis and eradicate non-Hodgkin lymphoma. *Cell*, *142*(5), 699–713.

Chao, M. P., Jaiswal, S., Weissman-Tsukamoto, R., Alizadeh, A. a, Gentles, A. J., Volkmer, J., … Weissman, I. L. (2010). Calreticulin is the dominant pro-phagocytic signal on multiple human cancers and is counterbalanced by CD47. *Science translational medicine*, *2*(63), 63ra94.

Chaturvedi, P., Gilkes, D. M., Takano, N., & Semenza, G. L. (2014). Hypoxia-inducible factor-dependent signaling between triple-negative breast cancer cells and mesenchymal stem cells promotes macrophage recruitment. *Proceedings of the National Academy of Sciences of the United States of America*, *111*(20), E2120-9.

Chen, X., Bahrami, A., Pappo, A., Easton, J., Dalton, J., Hedlund, E., … Dyer, M. A. (2014). Recurrent somatic structural variations contribute to tumorigenesis in pediatric osteosarcoma. *Cell Reports*, *7*(1), 104–112.

Chokri, M., Girard, A., Borrelly, M. C., Oleron, C., Romet-Lemonne, J. L., & Bartholeyns, J. (1992). Adoptive immunotherapy with bispecific antibodies: targeting through macrophages. *Research in Immunology*, *143*(1), 95–99.

Cioffi, M., Trabulo, S., Hidalgo, M., Costello, E., Greenhalf, W., Erkan, M., … Heeschen, C. (2015). Inhibition of CD47 Effectively targets pancreatic cancer stem cells via dual mechanisms. *Clinical Cancer Research*, *21*(10), 2325–2337.

Colegio, O. R., Chu, N.-Q., Szabo, A. L., Chu, T., Rhebergen, A. M., Jairam, V., … Medzhitov, R. (2014). Functional polarization of tumour-associated macrophages by tumour-derived lactic acid. *Nature*, *513*(7519), 559–63.

Condeelis, J., & Pollard, J. W. (2006). Macrophages: Obligate partners for tumor cell migration, invasion, and metastasis. *Cell*, *124*(2), 263–266.

Costello, M., Pugh, T. J., Fennell, T. J., Stewart, C., Lichtenstein, L., Meldrim, J. C., … Getz, G. (2013). Discovery and characterization of artifactual mutations in deep coverage targeted capture sequencing data due to oxidative DNA damage during sample preparation. *Nucleic Acids Research*, *41*(6).

Covassin, L., Laning, J., Abdi, R., Langevin, D. L., Phillips, N. E., Shultz, L. D., & Brehm, M. A. (2011). Human peripheral blood CD4 T cell-engrafted non-obese diabetic-scid IL2ry null H2-Ab1 tm1Gru Tg (human leucocyte antigen D-related 4) mice: A mouse model of human allogeneic graft-versus-host disease. *Clinical and Experimental Immunology*, *166*(2), 269–280.

Cox, D., & Greenberg, S. (2001). Phagocytic signaling strategies: Fc(gamma)receptor-mediated phagocytosis as a model system. *Seminars in immunology*, *13*(6), 339–45.

Cross, S. E., Jin, Y.-S., Lu, Q.-Y., Rao, J., & Gimzewski, J. K. (2011). Green tea extract selectively targets nanomechanics of live metastatic cancer cells. *Nanotechnology*, *22*(21), 215101.

Cross, S. E., Yu-Sheng, J., Jianyu, R., & Gimzewski, J. K. (2007). Nanomechanical analysis of cells from cancer patients. *Nature Nanotechnology*, *2*(12), 780–783.

Dahal, L. N., Roghanian, A., Beers, S. A., & Cragg, M. S. (2015). Fc (gamma) R requirements leading to successful immunotherapy. *Immunological Reviews*, *268*(1), 104–122.

Dahl, K. N., Parthasarathy, R., Westhoff, C. M., Layton, D. M., & Discher, D. E. (2004). Protein 4.2 is critical to CD47-membrane skeleton attachment in human red cells. *Blood*, *103*(3), 1131–1136.

de Bruin, E. C., Mcgranahan, N., Mitter, R., Salm, M., Wedge, D. C., Yates, L., …

Swanton, C. (2013). Spatial and temporal diversity in genomic instability processes defines lung cancer evolution. *Science*, *346*(6206), 251–256.
Denais, C. M., Gilbert, R. M., Isermann, P., Mcgregor, A. L., te Lindert, M., Weigelin, B., … Lammerding, J. (2016). Nuclear envelope rupture and repair during cancer cell migration. *Science*, *352*(6283), 353–358.
Diridollou, S., Vabre, V., Berson, M., Black, D., Lagarde, J. M., Gregoire, J. M., & Gall, Y. (2001). Skin ageing: Changes of physical properties of human skin in vivo. *International Journal of Cosmetic Science*, *23*, 353–362.
Discher, D. E., Ortis, V., Srinivas, G., Klein, M. L., & Kim, Y. (2014). Emerging Applications of Polymerosomes in Delivery: from Molecular Dynamics to Shrinkage of Tumors. *Prog Polym Sci.*, *32*, 838–857.
Dorward, D. a, Lucas, C. D., Alessandri, A. L., Marwick, J. a, Rossi, F., Dransfield, I., … Rossi, A. G. (2013). Technical Advance: Autofluorescence-based sorting: rapid and nonperturbing isolation of ultrapure neutrophils to determine cytokine production. *Journal of leukocyte biology*, *94*(July), 1–10.
Dupont, S., Morsut, L., Aragona, M., Enzo, E., Giulitti, S., Cordenonsi, M., … Piccolo, S. (2011). Role of YAP/TAZ in mechanotransduction. *Nature*, *474*, 179–183.
Eapen, M., Giralt, S. a, Horowitz, M. M., Klein, J. P., Wagner, J. E., Zhang, M.-J., … deLima, M. (2004). Second transplant for acute and chronic leukemia relapsing after first HLA-identical sibling transplant. *Bone marrow transplantation*, *34*(8), 721–727.
Egeblad, M., Rasch, M. G., & Weaver, V. M. (2010). Dynamic interplay between the collagen scaffold and tumor evolution. *Current Opinion in Cell Biology*, *22*(5), 697–706.
Ely, P., Wallace, P. K., Givan, a L., Graziano, R. F., Guyre, P. M., & Fanger, M. W. (1996). Bispecific-armed, interferon gamma-primed macrophage-mediated phagocytosis of malignant non-Hodgkin's lymphoma. *Blood*, *87*(9), 3813–3821.
Engler, A. J., Sen, S., Sweeney, H. L., & Discher, D. E. (2006). Matrix Elasticity Directs Stem Cell Lineage Specification. *Cell*, *126*(4), 677–689.
Evans, I., Ghai, P., Urbancic, V., Tan, K., & Wood, W. (2013). SCAR/WAVE mediated processing of apoptotic corpses is essential for effective macrophage migration in Drosophila. *Cell Death and Differentiation*, (20), 709–720.
Faradji, A., Bohbot, A., Frost, H., Schmitt-Goguel, M., Siffert, J. C., Dufour, P., … Oberling, F. (1991a). Phase I study of liposomal MTP-PE-activated autologous monocytes administered intraperitoneally to patients with peritoneal carcinomatosis. *Journal of Clinical Oncology*, *9*(7), 1251–1260.
Faradji, A., Bohbot, A., Frost, H., Schmitt-Goguel, M., Siffert, J. C., Dufour, P., … Oberling, F. (1991b). Phase I study of liposomal MTP-PE-activated autologous monocytes administered intraperitoneally to patients with peritoneal carcinomatosis. *Journal of Clinical Oncology*, *9*(7), 1251–1260.
Feng, M., Chen, J. Y., Weissman-Tsukamoto, R., Volkmer, J.-P., Ho, P. Y., McKenna, K. M., … Weissman, I. L. (2015). Macrophages eat cancer cells using their own calreticulin as a guide: Roles of TLR and Btk. *Proceedings of the National Academy of Sciences*, 201424907.
Fidler, I. J., & Kleinerman, E. S. (1984). Lymphokine-activated human blood monocytes

destroy tumor cells but not normal cells under cocultivation conditions. *Journal of Clinical Oncology*, *2*(8), 937–943.
Fousek, K., & Ahmed, N. (2015). The evolution of T-cell therapies for solid malignancies. *Clinical Cancer Research*, *21*(15), 3384–3392.
Franco, R. S., Puchulu-Campanella, M. E., Barber, L. A., Palascak, M. B., Joiner, C. H., Low, P. S., & Cohen, R. M. (2013). Changes in the properties of normal human red blood cells during in vivo aging. *american journal of hematology*, *88*(1), 44–51.
Franklin, R. a, Liao, W., Sarkar, A., Kim, M. V, Bivona, M. R., Liu, K., … Li, M. O. (2014). The Cellular and Molecular Origin of Tumor-Associated Macrophages. *Science (New York, N.Y.)*, *921*.
Fuhrmann, A., Staunton, J. R., Nandakumar, V., Banyai, N., Davies, P. C. W., & Ros, R. (2011). AFM stiffness nanotomography of normal, metaplastic and dysplastic human esophageal cells. *Physical Biology*, *8*(1), 15007.
Fujiwara, T., Fukushi, J.-I., Yamamoto, S., Matsumoto, Y., Setsu, N., Oda, Y., … Iwamoto, Y. (2011). Macrophage infiltration predicts a poor prognosis for human ewing sarcoma. *The American journal of pathology*, *179*(3), 1157–1170.
Gabrielle Faure-André, Vargas, P., Yuseff, M.-I., Heuzé, M., Diaz, J., Lankar, D., … Lennon-Duménil, A.-M. (2008). Regulation of Dendritic Cell Migration by CD74, the MHC Class II–Associated Invariant Chain. *Science*, *322*(December), 1705.
Garcia-Hernandez, M. de la L., Hamada, H., Reome, J. B., Misra, S. K., Tighe, M. P., & Dutton, R. W. (2010). Adoptive transfer of tumor-specific Tc17 effector T cells controls the growth of B16 melanoma in mice. *Journal of immunology (Baltimore, Md. : 1950)*, *184*(8), 4215–27.
Gardai, S. J., McPhillips, K. a, Frasch, S. C., Janssen, W. J., Starefeldt, A., Murphy-Ullrich, J. E., … Henson, P. M. (2005). Cell-surface calreticulin initiates clearance of viable or apoptotic cells through trans-activation of LRP on the phagocyte. *Cell*, *123*(2), 321–34.
Gerlinger, M., Rowan, A. J., Horswell, S., Larkin, J., Endesfelder, D., Gronroos, E., … Swanton, C. (2012). Intratumor heterogeneity and branched evolution revealed by multiregion sequencing. *The New England Journal of Medicine*, *366*(10), 883–892.
Gholamin, S., Mitra, S. S., Feroze, A. H., Liu, J., Kahn, S. A., Zhang, M., … Cheshier, S. H. (2017). Disrupting the CD47-SIRPα anti-phagocytic axis by a humanized anti-CD47 antibody is an efficacious treatment for malignant pediatric brain tumors. *Science Translational Medicine*, *9*(381), 1–13.
Gosselin, D., Link, V. M., Romanoski, C. E., Fonseca, G. J., Eichenfield, D. Z., Spann, N. J., … Glass, C. K. (2014). Environment Drives Selection and Function of Enhancers Controlling Tissue-Specific Macrophage Identities. *Cell*, *159*(6), 1327–1340.
Greenberg, S., Chang, P., & Silverstein, S. C. (1994). Tyrosine phosphorylation of the gamma subunit of Fc gamma receptors, p72syk, and paxillin during Fc receptor-mediated phagocytosis in macrophages. *Journal of Biological Chemistry*, *269*(5), 3897–3902.
Gregory, C. D., & Brown, S. B. (2005). Apoptosis: eating sensibly. *Nature cell biology*, *7*(12), 1161–3.
Guz, N., Dokukin, M., Kalaparthi, V., & Sokolov, I. (2014). If cell mechanics can be

described by elastic modulus: Study of different models and probes used in indentation experiments. *Biophysical*, *107*(3), 564–575.
Harada, T., Swift, J., Irianto, J., Shin, J. W., Spinler, K. R., Athirasala, A., … Discher, D. E. (2014). Nuclear lamin stiffness is a barrier to 3D migration, but softness can limit survival. *Journal of Cell Biology*, *204*(5), 669–682.
Hartung, G., Zeis, M., Glass, B., Dreger, P., Steinmann, J., Schmitz, N., & Uharek, L. (2003). Enhanced antileukemic activity of allogeneic peripheral blood progenitor cell transplants following donor treatment with the combination of granulocyte colony-stimulating factor (G-CSF) and stem cell factor (SCF) in a murine transplantation model. *Bone marrow transplantation*, *32*(1), 49–56.
Heemskerk, B., Kvistborg, P., & Schumacher, T. N. M. (2013). The cancer antigenome. *The EMBO Journal*, *32*(2), 194–203.
Helft, J., Böttcher, J., Chakravarty, P., Zelenay, S., Huotari, J., Schraml, B. U., … Reis e Sousa, C. (2015). GM-CSF Mouse Bone Marrow Cultures Comprise a Heterogeneous Population of CD11c+MHCII+ Macrophages and Dendritic Cells. *Immunity*, *42*(6), 1197–1211.
Hennemann, B., Beckmann, G., Eichelmann, A., Rehm, A., & Andreesen, R. (1998). Phase I trial of adoptive immunotherapy of cancer patients using monocyte-derived macrophages activated with interferon g and lipopolysaccharide. *Cancer Immunology, Immunotherapy*, *45*, 250–256.
Hennemann, B., Rehm, A., Kottke, A., Meidenbauer, N., & Andreesen, R. (1997). Adoptive Immunotherapy with Tumor-cytotoxi macrophages Derived from Recombinant Human Granulocyte-Macrophage Colony-Stimulating Factor Mobilized Peripheral Blood Monocytes. *Journal of immunotherapy*, 365–371.
Ho, C. C. M., Guo, N., Sockolosky, J. T., Ring, A. M., Weiskopf, K., Özkan, E., … Garcia, K. C. (2015). "Velcro" engineering of high affinity CD47 Ectodomain as signal regulatory protein (alpha) (SIRPa) antagonists that enhance antibody-dependent cellular phagocytosis. *Journal of Biological Chemistry*, *290*(20), 12650–12663.
Hodi, F. S., O'Day, S. J., McDermott, D. F., Weber, R. W., Sosman, J. A., Haanen, J. B., … Urba, W. J. (2010). Improved survival with ipilimumab in patients with metastatic melanoma. *The New England Journal of Medicine*, *363*(8), 711–723.
Horrigan, S. K., Iorns, E., Williams, S. R., Perfito, N., & Errington, T. M. (2017). Replication Study: The CD47-signal regulatory protein alpha (SIRPa) interaction is a therapeutic target for human solid tumors. *eLIFE*, 1–12.
Hoyt, K., Castaneda, B., Zhang, M., Nigwekar, P., di Sant'Agnese, P. A., Joseph, J. V, … Parker, K. J. (2008). Tissue elasticity properties as biomarkers for prostate cancer. *Cancer Biomarkers*, *4*(585), 213–225.
Hsu, Y.-F., Ajona, D., Corrales, L., Lopez-Picazo, J. M., Gurpide, A., Montuenga, L. M., & Pio, R. (2010). Complement activation mediates cetuximab inhibition of non-small cell lung cancer tumor growth in vivo. *Molecular cancer*, *9*, 139.
Irianto, J., Pfeifer, C. R., Bennett, R. R., Xia, Y., Ivanovska, I. L., Liu, A. J., … Discher, D. E. (2016). Nuclear constriction segregates mobile nuclear proteins away from chromatin. *Molecular Biology of the Cell*, *27*, 4011–4020.
Irianto, J., Pfeifer, C. R., Ivanovska, I. L., Swift, J., & Discher, D. E. (2016). Nuclear

lamins in cancer. *Cellular and Molecular Bioengineering*, *9*(2), 258–267.
Irianto, J., Pfeifer, C. R., Xia, Y., & Discher, D. E. (2016). SnapShot: Mechanosensing matrix. *Cell*, *165*, 1820--1820.e1.
Irianto, J., Xia, Y., Pfeifer, C. R., Athirasala, A., Ji, J., Alvey, C., … Discher, D. E. (2017a). DNA Damage Follows Repair Factor Depletion and Portends Genome Variation in Cancer Cells after Article DNA Damage Follows Repair Factor Depletion and Portends Genome Variation in Cancer Cells after Pore Migration. *Current Biology*, 1–14.
Irianto, J., Xia, Y., Pfeifer, C. R., Athirasala, A., Ji, J., Alvey, C., … Discher, D. E. (2017b). DNA damage follows repair factor depletion and portends genome variation in cancer cells after pore migration. *Current Biology*, *27*(2), 210–223.
Jablonski, K. A., Amici, S. A., Webb, L. M., Ruiz-Rosado, J. D. D., Popovich, P. G., Partida-Sanchez, S., & Guerau-De-arellano, M. (2015). Novel markers to delineate murine M1 and M2 macrophages. *PLoS ONE*, *10*(12), 5–11.
Jacoby, E., Yang, Y., Qin, H., Chien, C. D., Kochenderfer, J. N., & Fry, T. J. (2016). Murine allogeneic CD19 CAR T cells harbor potent antileukemic activity but have the potential to mediate lethal GVHD. *Blood*, *127*(10), 1361–1370.
Jo, P., König, A., Schirmer, M., Kitz, J., Conradi, L.-C., Azizian, A., … Gaedcke, J. (2016). Heterogeneity of KRAS mutation status in rectal cancer. *PLOS ONE*, *20*.
Johanna A. Joyce, & Fearon, D. T. (2015). T cell exclusion, immune privilege, and the tumor microenvironment. *Cancer immunology, immunotherapy : CII*, *348*(6230), 74–79.
Kakarla, S., & Gottschalk, S. (2014). CAR T Cells for Solid Tumors - Armed and Ready to Go ? *The Cancer Journal*, *20*(2), 151–155.
Kandoth, C., McLellan, M. D., Vandin, F., Ye, K., Niu, B., Lu, C., … Ding, L. (2013). Mutational landscape and significance across 12 major cancer types. *Nature*, *502*, 333–339.
Kang, Y. (2011). Prognostic Potential of Cell Surface Markers and Pim Kinases in Multiple Myeloma. *Clinicaltrial.gov*.
Kaur, S., Soto-Pantoja, D. R., Stein, E. V, Liu, C., Elkahloun, A. G., Pendrak, M. L., … Roberts, D. D. (2013). Thrombospondin-1 signaling through CD47 inhibits self-renewal by regulating c-Myc and other stem cell transcription factors. *Scientific reports*, *3*, 1673.
Kawano, S., Kojima, M., Higuchi, Y., Sugimoto, M., Ikeda, K., Sakuyama, N., … Saito, N. (2015). Assessment of elasticity of colorectal cancer tissue, clinical utility, pathological and phenotypical relevance. *Cancer Science*, *106*(9), 1232–1239.
King, M. A., Covassin, L., Brehm, M. A., Racki, W., Pearson, T., Leif, J., … Greiner, D. L. (2009). Human peripheral blood leucocyte non-obese diabetic-severe combined immunodeficiency interleukin-2 receptor gamma chain gene mouse model of xenogeneic graft-versus-host-like disease and the role of host major histocompatibility complex. *Clinical and Experimental Immunology*, *157*(1), 104–118.
Klein, E. A., Castagnino, P., Kothapalli, D., Yin, L., Byfield, F. J., Xu, T., … Assoian, R. K. (2009). Cell cycle control by physiological matrix elasticity and in vivo tissue stiffening. *Current Biology*, *19*(18), 1511–1518.

Klein, O., Clements, A., Menzies, A. M., O'Toole, S., Kefford, R. F., & Long, G. V. (2013). BRAF inhibitor activity in V600R metastatic melanoma – Response. *European Journal of Cancer*, *49*(7), 1797–1798.

Kovac, M., Blattmann, C., Ribi, S., Smida, J., Mueller, N. S., Engert, F., … Baumhoer, D. (2015). Exome sequencing of osteosarcoma reveals mutation signatures reminiscent of BRCA deficiency. *Nature Communications*.

Kufe, D. W. (2009). Mucins in cancer: function, prognosis and therapy. *Nature reviews. Cancer*, *9*(12), 874–85.

Lacerna, L. V., Stevenson, G. W., & Stevenson, H. C. (1988). Adoptive cancer immunotherapy utilizing lymphokine activated killer cells and gamma interferon activated killer monocytes. *Pharmacology and Therapeutics*, *38*(3), 453–465.

Lam, W. a, Rosenbluth, M. J., Fletcher, D. a, & Dc, W. (2009). Chemotherapy exposure increases leukemia cell stiffness Brief report Chemotherapy exposure increases leukemia cell stiffness. *Blood*, *109*(8), 3505–3508.

Lan, C., Huang, X., Lin, S., Huang, H., Cai, Q., Wan, T., … Liu, J. (2012). Expression of M2-Polarized Macrophages is Associated with Poor Prognosis for Advanced Epithelial Ovarian Cancer. *Technol Cancer Res Treat*, *12*(3).

Lavin, Y., Winter, D., Blecher-gonen, R., David, E., Keren-shaul, H., Merad, M., … Amit, I. (2014). Tissue-Resident Macrophage Enhancer Landscapes Are Shaped by the Local Microenvironment. *Cell*, *159*(6), 1312–1326.

Lavin, Y., Winter, D., Blecher-Gonen, R., David, E., Keren-Shaul, H., Merad, M., … Amit, I. (2014). Tissue-resident macrophage enhancer landscapes are shaped by the local microenvironment. *Cell*, *159*(6), 1312–1326.

Lawrence, M. S., Stojanov, P., Polak, P., Kryukov, G. V, Cibulskis, K., Sivachenko, A., … Getz, G. (2013). Mutational heterogeneity in cancer and the search for new cancer-associated genes. *Nature*, *499*, 214–218.

LeBlanc, V. G., & Marra, M. A. (2015). Next-generation sequencing approaches in cancer: Where have they brought us and where will they take us? *Cancers*, *7*, 1925–1958.

Lee, W. Y., Weber, D. A., Laur, O., Stowell, S. R., McCall, I., Andargachew, R., … Parkos, C. A. (2010). The role of cis dimerization of signal regulatory protein alpha (SIRPA) in binding to CD47. *Journal of Biological Chemistry*, *285*(49), 37953–37963.

Leek, R. D., Lewis, C. E., Whitehouse, R., Greenall, M., Clarke, J., & Harris, A. L. (1996). Association of Macrophage Infiltration with angiogenesis and Prognosis in Invasive Breast Carinoma. *Cancer Research*, *56*(16), 4625–4629.

Lekka, M., Gil, D., Pogoda, K., Dulinska-Litewka, J., Jach, R., Gostek, J., … Laidler, P. (2012). Cancer cell detection in tissue sections using AFM. *Archives of Biochemistry and Biophysics*, *518*, 151–156.

Lekka, M., Pogoda, K., Gostek, J., Klymenko, O., Prauzner-Bechcicki, S., Wiltowska-Zuber, J., … Stachura, Z. (2012). Cancer cell recognition – mechanical phenotype. *Micron*, *43*(12), 1259–1266.

Levental, K. R., Yu, H., Kass, L., Lakins, J. N., Egeblad, M., Erler, J. T., … Weaver, V. M. (2009). Matrix Crosslinking Forces Tumor Progression by Enhancing Integrin Signaling. *Cell*, *139*(5), 891–906.

Levental, K. R., Yu, H., Kass, L., Lakins, J. N., Egeblad, M., Erler, J. T., … Weaver, V. M. (2010). Matrix crosslinking forces tumor progression by enhancing integrin signaling. *Cell*, *139*(5), 891–906.

Li, Y., Bare, L. A., Bender, R. A., Sninsky, J. J., Wilson, L. S., Devlin, J. J., & Waldman, F. M. (2015). Cost effectiveness of sequencing 34 cancer-associated genes as an aid for treatment selection in patients with metastatic melanoma. *Molecular Diagnosis {&} Therapy*, *19*, 169–177.

Lim, Y.-J., Deo, D., Singh, T. P., Jones, D. B., & De, S. (2009). In situ measurement and modeling of biomechanical response of human cadaveric soft tissues for physics-based surgical simulation. *Surgical Endoscopy*, *23*(6), 1298–1307.

Lindberg, F. P., Lublin, D. M., Telen, M. J., Veile, R. A., Miller, Y. E., Donis-Keller, H., & Brown, E. J. (1994). Rh-related antigen CD47 is the signal-transducer integrin-associated protein. *Journal of Biological Chemistry*, *269*(3), 1567–1570.

Liotta, L. A., Steeg, P. S., & Stetler-Stevenson, W. G. (1991). Cancer metastasis and angiogenesis: An imbalance of positive and negative regulation. *Cell*, *64*(2), 327–336.

Liu, Q., Wen, W., Tang, L., Qin, C.-J., Lin, Y., Zhang, H.-L., … Yan, H.-X. (2016). Inhibition of SIRP$α$ in dendritic cells potentiates potent antitumor immunity. *OncoImmunology*, *5*(9).

Liu, Q., Wen, W., Tang, L., Qin, C.-J., Lin, Y., Zhang, H.-L., … Yan, H.-X. (2016). Inhibition of SIRPα in dendritic cells potentiates potent antitumor immunity. *OncoImmunology*, *5*(August), e1183850.

Liu, X., Pu, Y., Cron, K., Deng, L., Kline, J., Frazier, W. a, … Xu, M. M. (2015). CD47 blockade triggers T cell–mediated destruction of immunogenic tumors. *Nature Medicine*, *21*(10), 1209–1215.

Lockhart, A. C., Bukowski, R., Rothenberg, M. L., Wang, K. K., Cooper, W., Grover, J., … Zhu, A. X. (2007). Phase I trial of oral MAC-321 in subjects with advanced malignant solid tumors. *Cancer Chemotherapy and Pharmacology*, *60*(2), 203–209.

Lopez, J. I., Kang, I., You, W.-K., McDonald, D. M., & Weaver, V. M. (2011). In situ force mapping of mammary gland transformation. *Integrative Biology*, *3*(9), 910–921.

Lu-emerson, C., Snuderl, M., Kirkpatrick, N. D., Goveia, J., Davidson, C., Huang, Y., … Batchelor, T. T. (2013). Increase in tumor-associated macrophages after antiangiogenic therapy is associated with poor survival among patients with recurrent glioblastoma. *NEURO-ONCOLOGY*, *15*(8), 1079–1087.

Lu-Emerson, C., Snuderl, M., Kirkpatrick, N. D., Goveia, J., Davidson, C., Huang, Y., … Jain, R. K. (2013). Increase in tumor-associated macrophages after antiangiogenic therapy is associated with poor survival among patients with recurrent glioblastoma. *Neuro-Oncology*, *15*(8), 1079–1087.

Lundqvist, M., Stigler, J., Elia, G., Lynch, I., Cedervall, T., & Dawson, K. A. (2008). Nanoparticle size and surface properties determine the protein corona with possible implications for biological impacts. *Proceedings of the National Academy of Sciences of the United States of America*, *105*(38), 14265–70.

Ly, L. V, Sluijter, M., van der Burg, S. H., Jager, M. J., & van Hall, T. (2013). Effective cooperation of monoclonal antibody and peptide vaccine for the treatment of mouse

melanoma. *Journal of immunology (Baltimore, Md. : 1950)*, *190*(1), 489–96.
Maciejowski, J., Li, Y., Bosco, N., Campbell, P. J., Maciejowski, J., Li, Y., … Lange, T. De. (2015). Chromothripsis and kataegis induced by telomere crisis. *Cell*, *163*(7), 1641–1654.
Majeti, R., Chao, M. P., Alizadeh, A. a, Pang, W. W., Jaiswal, S., Gibbs, K. D., … Weissman, I. L. (2009). CD47 is an adverse prognostic factor and therapeutic antibody target on human acute myeloid leukemia stem cells. *Cell*, *138*(2), 286–99.
Mantovani, A., Bottazzi, B., Colotta, F., Sozzani, S., & Ruco, L. (1992). The origin and function of tumor-associated macrophages. *Immunology today*, *13*(7), 265–270.
Mantovani, A., Sozzani, S., Locati, M., Allavena, P., & Sica, A. (2002). Macrophage polarization: Tumor-associated macrophages as a paradigm for polarized M2 mononuclear phagocytes. *Trends in Immunology*, *23*(11), 549–555.
Martin, S. D., Brown, S. D., Wick, D. A., Nielsen, J. S., Kroeger, D. R., Twumasi-Boateng, K., … Nelson, B. H. (2016). Low mutation burden in ovarian cancer may limit the utility of neoantigen-targeted vaccines. *PLOS ONE*, *11*(5).
Martin, S. D., Coukos, G., Holt, R. A., & Nelson, B. H. (2015). Targeting the undruggable: Immunotherapy meets personalized oncology in the genomic era. *Annals of Oncology*, *26*, 2367–2374.
Martincorena, I., & Campbell, P. J. (2015). Somatic mutation in cancer and normal cells. *Science*, *349*(6255), 961–968.
Martincorena, I., Roshan, A., Gerstung, M., Ellis, P., Loo, P. Van, Mclaren, S., … Campbell, P. J. (2015). High burden and pervasive positive selection of somatic mutations in normal human skin. *Science*, *348*(6237), 880–886.
Massuger, L., Claessens, R., Kenemans, P., Hanseiaar, T., & Corstens, F. (1990). Nonantigen-Specific Tissue Localization of Monoclonal Antibodies. *Journal of nuclear medicine : official publication, Society of Nuclear Medicine*, *31*(8).
Massuger, L. F. A. G., Kenemans, P., Claessens, R. A. M. J., Verheijen, R. H. M., Schijf, C. P. T., Strijk, S. P., … Corstens, F. H. M. (1990). Immunoscintigraphy of ovarian cancer with indium-111-labeled OV-TL 3 F(ab')2 monoclonal antibody. *Journal of Nuclear Medicine*, *31*(11), 1802–1810.
Mathur, A. B., Collinsworth, A. M., Reichert, W. M., Kraus, W. E., & Truskey, G. A. (2001). Endothelial, cardiac muscle and skeletal muscle exhibit different viscous and elastic properties as determined by atomic force microscopy. *Journal of Biomechanics*, *34*, 1545–1553.
Matsushita, H., Sato, Y., Karasaki, T., Nakagawa, T., Kume, H., Ogawa, S., … Kakimi, K. (2016). Neoantigen load, antigen presentation machinery, and immune signatures determine prognosis in clear cell renal cell carcinoma. *Cancer Immunology Research*, *4*(5), 463–471.
Mawby, W. J., Holmes, C. H., Anstee, D. J., Spring, F. a, & Tanner, M. J. (1994). Isolation and characterization of CD47 glycoprotein: a multispanning membrane protein which is the same as integrin-associated protein (IAP) and the ovarian tumour marker OA3. *The Biochemical journal*, *304 (Pt 2*, 525–530.
McArthur, G. A., Chapman, P. B., Robert, C., Larkin, J., Haanen, J. B., Dummer, R., … Hauschild, A. (2014). Safety and efficacy of vemurafenib in BRAFV600E and BRAFV600K mutation-positive melanoma (BRIM-3): Extended follow-up of a

phase 3, randomised, open-label study. *The Lancet Oncology*, *15*, 323–332.
Mcgranahan, N., Favero, F., de Bruin, E. C., Birkbak, N. J., Szallasi, Z., & Swanton, C. (2015). Clonal status of actionable driver events and the timing of mutational processes in cancer evolution. *Science Translational Medicine*, *7*(283).
McIntosh, B. E., Brown, M. E., Duffin, B. M., Maufort, J. P., Vereide, D. T., Slukvin, I. I., & Thomson, J. A. (2015). Nonirradiated NOD,B6.SCID ll2r gamma-/-kitW41/W41 (NBSGW) mice support multilineage engraftment of human hematopoietic cells. *Stem Cell Reports*, *4*(2), 171–180.
Michon, J., Moutel, S., Barbet, J., Romet-Lemonne, J. L., Deo, Y. M., Fridman, W. H., & Teillaud, J. L. (1995). In vitro killing of neuroblastoma cells by neutrophils derived from granulocyte colony-stimulating factor-treated cancer patients using an anti-disialoganglioside/anti-Fc gamma RI bispecific antibody. *Blood*, *86*(3), 1124–1130.
Moore, K. J., Sheedy, F. J., & Fisher, E. A. (2013). Macrophages in atherosclerosis: a dynamic balance. *Nature reviews. Immunology*, *13*(10), 709–21.
Motegi, S. I., Okazawa, H., Murata, Y., Kanazawa, Y., Saito, Y., Kobayashi, H., … Matozaki, T. (2008). Essential roles of SHPS-1 in induction of contact hypersensitivity of skin. *Immunology Letters*, *121*(1), 52–60.
Murdoch, C., Muthana, M., Coffelt, S. B., & Lewis, C. E. (2008). The role of myeloid cells in the promotion of tumour angiogenesis. *Nature reviews. Cancer*, *8*(8), 618–631.
Nair, P., Karthick, S., Spinler, K., Vakili, M., Lavasanifar, A., & Discher, D. (2016). Filomicelles from aromatic diblock copolymers increase paclitaxel-induced tumor cell death and aneuploidy compared with aliphatic copolymers. *Nanomedicine*, *May 13 201*.
Nemzek, J. A., Bolgos, G. L., Williams, B. A., & Remick, D. G. (2001). Differences in normal values for murine white blood cell counts and other hematological parameters based on sampling site. *Inflammation research*, *50*(10), 523–527.
Nicol, a J., Tokuyama, H., Mattarollo, S. R., Hagi, T., Suzuki, K., Yokokawa, K., & Nieda, M. (2011). Clinical evaluation of autologous gamma delta T cell-based immunotherapy for metastatic solid tumours. *British journal of cancer*, *105*(6), 778–786.
Nowak, M. A., & Waclaw, B. (2017). Genes, environment, and "bad luck." *Science*, *355*, 1266–1267.
Okazawa, H., Motegi, S., Ohyama, N., Ohnishi, H., Tomizawa, T., Kaneko, Y., … Alerts, E. (2005). Negative regulation of phagocytosis in macrophages by the CD47-SHPS-1 system. *Journal of immunology (Baltimore, Md. : 1950)*, *174*(4), 2004–11.
Oldenborg, P.-A., Gresham, H. D., Chen, Y., Izui, S., & Lindberg, F. P. (2002). Lethal autoimmune hemolytic anemia in CD47-deficient nonobese diabetic (NOD) mice. *Blood*, *99*(10), 3500–3504.
Oldenborg, P.-A., Zheleznyak, A., Fang, Y.-F., Lagenaur, C. F., Gresham, H. D., & Lindberg, F. P. (2000). Role of CD47 as a Marker of Self on Red Blood Cells. *Science*, *288*(5473), 2051–2054.
Oldenborg, P., Zheleznyak, A., Fang, Y., Lagenaur, C. F., Gresham, H. D., & Lindberg,

F. P. (2000). Role of CD47 as a marker of self on red blood cells. *Science*, *288*(June), 2051–2054.
Overdijk, M. B., Verploegen, S., Ortiz Buijsse, A., Vink, T., Leusen, J. H. W., Bleeker, W. K., & Parren, P. W. H. I. (2012). Crosstalk between Human IgG Isotypes and Murine Effector Cells. *The Journal of Immunology*, *189*(7), 3430–3438.
Pallasch, C. P., Leskov, I., Braun, C. J., Vorholt, D., Drake, A., Soto-Feliciano, Y. M., … Hemann, M. T. (2014). Sensitizing protective tumor microenvironments to antibody-mediated therapy. *Cell*, *156*(3), 590–602.
Pan, Y. fei, Tan, Y. xiong, Wang, M., Zhang, J., Zhang, B., Yang, C., … Wang, H. yang. (2013). Signal regulatory protein α is associated with tumor-polarized macrophages phenotype switch and plays a pivotal role in tumor progression. *Hepatology*, *58*(2), 680–691.
Pan, Y., Tan, Y., Wang, M., Zhang, J., Zhang, B., Yang, C., … Wang, H. (2013). Signal regulatory protein a is associated with tumor-polarized macrophages phenotype switch and plays a pivotal role in tumor progression. *Hepatology*, *58*(2), 680–691.
Pardoll, D. M. (2016). The blockade of immune checkpoints in cancer immunotherapy. *Nature Reviews Cancer*, *12*(4), 252–264.
Patel, N. R., Bole, M., Chen, C., Hardin, C. C., Kho, A. T., Mih, J., … Koziel, H. (2012). Cell Elasticity Determines Macrophage Function. *PLoS ONE*, *7*(9), 1–10.
Paul, S., Weiskopf, D., Angelo, M. A., Sidney, J., Peters, B., & Sette, A. (2013). NIH Public Access. *The Journal of Immunology*, *191*(12), 5831–5839.
Pearson, T., Shultz, L. D., Miller, D., King, M., Laning, J., Fodor, W., … Greiner, D. L. (2008). Non-obese diabetic-recombination activating gene-1 (NOD-Rag1 null) interleukin (IL)-2 receptor common gamma chain (IL2r gamma null) null mice: A radioresistant model for human lymphohaematopoietic engraftment. *Clinical and Experimental Immunology*, *154*(2), 270–284.
Pelham, R. J., & Wang, Y. (1997). Cell locomotion and focal adhesions are regulated by substrate flexibility. *PNAS*, *94*, 13661–13665.
Petrie, R. J., Gavara, N., Chadwick, R. S., & Yamada, K. M. (2012). Nonpolarized signaling reveals two distinct modes of 3D cell migration. *The Journal of Cell Biology*, *197*(3), 439–455.
Pirker, R. (2013). EGFR-directed monoclonal antibodies in non-small cell lung cancer. *Targeted Oncology*, *8*(1), 47–53.
Posey, A. D., Schwab, R. D., Boesteanu, A. C., Steentoft, C., Mandel, U., Engels, B., … al., et. (2016). Engineered CAR T Cells Targeting the Cancer-Associated Tn-Glycoform of the Membrane Mucin MUC1 Control Adenocarcinoma. *Immunity*, *44*(6), 1444–1454.
Prabhune, M., Belge, G., Dotzauer, A., Bullerdiek, J., & Radmacher, M. (2012). Comparison of mechanical properties of normal and malignant thyroid cells. *Micron*, *43*(12), 1267–1272.
Przybyla, L., Muncie, J. M., & Weaver, V. M. (2016). Mechanical control of epithelial-to-mesenchymal transitions in development and cancer. *Annual Review of Cell and Developmental Biology*, *32*, 527–554.
Quintana, E., Piskounova, E., Shackleton, M., Weinberg, D., Eskiocak, U., Fullen, D. R., … Morrison, S. J. (2012). Human Melanoma Metastasis in NSG Mice

Correlates with Clinical Outcome in Patients. *Science translational medicine*, *149*(159).
Raab, M., Gentili, M., de Belly, H., Thiam, H. R., Vargas, P., Jimenez, A. J., … Piel, M. (2016). ESCRT III repairs nuclear envelope ruptures during cell migration to limit DNA damage and cell death. *Science*, *352*(6283), 359–362.
Rahma, O. E., Hamilton, J. M., Wojtowicz, M., Dakheel, O., Bernstein, S., Liewehr, D. J., … Khleif, S. N. (2014). The immunological and clinical effects of mutated ras peptide vaccine in combination with IL-2, GM-CSF, or both in patients with solid tumors. *Journal of Translational Medicine*, *12*, 55–67.
Rajasagi, M., Shukla, S. A., Fritsch, E. F., Keskin, D. B., DeLuca, D., Carmona, E., … Wu, C. J. (2014). Systematic identification of personal tumor-specific neoantigens in chronic lymphocytic leukemia. *Blood*, *124*(3), 453–463.
Rajesh, D., Zhou, Y., Jankowska-Gan, E., Roenneburg, D. A., Dart, M. L., Torrealba, J., & Burlingham, W. J. (2010). Th1 and Th17 immunocompetence in humanized NOD/SCID/IL2rgammanull mice. *Human immunology*, *71*(6), 551–9.
Ramachandra, L., Noss, E., Boom, W. H., & Harding, C. V. (1999). Microreview Phagocytic processing of antigens for presentation by class II major histocompatibility complex molecules. *Cellular Microbiology*, *1*(3), 205–214.
Ramos, C. A., Savoldo, B., & Dotti, G. (2015). CD19-CAR trials, *20*(2), 112–118.
Rettig, M. P., Low, P. S., Gimm, J. a, Mohandas, N., Wang, J., & Christian, J. a. (1999). Evaluation of biochemical changes during in vivo erythrocyte senescence in the dog. *Blood*, *93*(1), 376–84.
Richard N. Hanna, Cekic, C., Sag, D., Tacke, R., Thomas, G. D., Nowyhed, H., … Hedrick, C. C. (2015). Patrolling monocytes control tumor metastasis to the lung. *Science*, *350*(6263), 985–990.
Riihimaki, M., Hemminki, A., Fallah, M., Thomsen, H., Sundquist, K., Sundquist, J., & Hemminki, K. (2014). Metastatic sites and survival in lung cancer. *Lung Cancer*, *86*(1), 78–84.
Rizvi, N. A., Hellmann, M. D., Snyder, A., Kvistborg, P., Makarov, V., Havel, J. J., … Chan, T. A. (2015). Mutational landscape determines sensitivity to PD-1 blockade in non-small cell lung cancer. *Science*, *348*(6230), 124–128.
Robbins, P. F., Lu, Y.-C., El-Gamil, M., Li, Y. F., Gross, C., Gartner, J., … Rosenberg, S. A. (2013). Mining exomic sequencing data to identify mutated antigens recognized by adoptively transferred tumor-reactive T cells. *Nature Medicine*, *19*(6), 747–752.
Rodriguez, D., Silvera, R., Carrio, R., Nadji, M., Caso, R., Rodriguez, G., … Torroella-Kouri, M. (2013). Tumor microenvironment profoundly modifies functional status of macrophages: Peritoneal and tumor-associated macrophages are two very different subpopulations. *Cellular Immunology*, *283*(1–2), 51–60.
Rodríguez, D., Silvera, R., Carrio, R., Nadji, M., Caso, R., Rodríguez, G., … Torroella-Kouri, M. (2013). Tumor microenvironment profoundly modifies functional status of macrophages: Peritoneal and tumor-associated macrophages are two very different subpopulations. *Cellular Immunology*, *283*, 51–60.
Rodriguez, P. L., Harada, T., Christian, D. a, Pantano, D. a, Tsai, R. K., & Discher, D. E. (2013). Minimal "Self" peptides that inhibit phagocytic clearance and enhance

delivery of nanoparticles. *Science (New York, N.Y.)*, *339*(6122), 971–5.
Roghanian, A., Teige, I., Mårtensson, L., Cox, K. L., Kovacek, M., Ljungars, A., … Cragg, M. S. (2015). Antagonistic Human FcγRIIB (CD32B) Antibodies have anti-tumor activity and overcome resistance to antibody therapy invivo. *Cancer Cell*, *27*(4), 473–488.
Roos, W. P., & Kaina, B. (2013). DNA damage-induced cell death: from specific DNA lesions to the DNA damage response and apoptosis. *Cancer letters*, *332*(2), 237–48.
Sabbatini, P. J., Ragupathi, G., Hood, C., Aghajanian, C. A., Juretzka, M., Iasonos, A., … Livingston, P. O. (2007). Pilot study of a heptavalent vaccine-keyhole limpet hemocyanin conjugate plus QS21 in patients with epithelial ovarian, fallopian tube, or peritoneal cancer. *Clinical Cancer Research*, *13*(5), 4170–4177.
Salmon, H., Franciszkiewicz, K., Damotte, D., Validire, P., Trautmann, A., Mami-chouaib, F., & Donnadieu, E. (2012). Matrix architecture defines the preferential localization and migration of T cells into the stroma of human lung tumors. *Journal of Clinical Investigation*, *122*(3), 899–910.
Sample, P. A., Boden, C., Zhang, Z., Pascual, J., Lee, T., Zangwill, L. M., … Goldbaum, M. (2008). T-Cell Receptor Gene Therapy of Established Tumors in a Murine Melanoma Model. *Journal of immunotherapy*, *31*(1), 1–6.
Schumacher, T., Bunse, L., Pusch, S., Sahm, F., Wiestler, B., Quandt, J., … Platten, M. (2014). A vaccine targeting mutant IDH1 induces antitumour immunity. *Nature*, *512*, 324–327.
Schumacher, T. N., & Schreiber, R. D. (2015). Neoantigens in cancer immunotherapy. *Science*, *348*(6230), 69–74.
Schwaederle, M., Parker, B. A., Schwab, R. B., Fanta, P. T., Boles, S. G., Daniels, G. A., … Kurzrock, R. (2014). Molecular tumor board: The University of California San Diego Moores Cancer Center experience. *The Oncologist*, *19*, 631–636.
Segal, N. H., Parsons, D. W., Peggs, K. S., Velculescu, V., Kinzler, K. W., Vogelstein, B., & Allison, J. P. (2008). Epitope landscape in breast and colorectal cancer. *Cancer Research*, *68*(3), 889–892.
Seshadri, R., Kutlaca, R. J., Trainor, K., Matthews, C., & Morley, A. A. (1987). Mutation rate of normal and malignant human lymphocytes. *Cancer Research*, *47*, 407–409.
Shain, A. H., Yeh, I., Kovalyshyn, I., Sriharan, A., Talevich, E., Gagnon, A., … Bastian, B. C. (2015). The genetic evolution of melanoma from precursor lesions. *The New England Journal of Medicine*, *373*, 1926–1936.
Shin, J., Buxboim, A., Spinler, K. R., Swift, J., Christian, D. A., Hunter, C. A., … Discher, D. E. (2014). Contractile forces sustain and polarize hematopoiesis from stem and progenitor cells. *Cell Stem Cell*, *14*(1), 81–93.
Shin, J., Spinler, K. R., Swift, J., Chasis, J. a, Mohandas, N., & Discher, D. E. (2013). Lamins regulate cell trafficking and lineage maturation of adult human hematopoietic cells. *Proceedings of the National Academy of Sciences*, *110*(47), 18892–18897.
Sievers, E. (2016a). A Trial of TTI-621 for Patients With Hematologic Malignancies. *Clinicaltrial.gov*.

Sievers, E. (2016b). Trial of Intratumoral Injections of TTI-621 in Subjects With Relapsed and Refractory Solid Tumors and Mycosis Fungoides. *Clinicaltrial.gov*.

Singh, S., Fujii, L. L., Murad, M. H., Wang, Z., Asrani, S. K., Ehman, R. L., … Talwalkar, J. A. (2013). Liver stiffness is associated with risk of decompensation, liver cancer, and death in patients with chronic liver diseases: A systematic review and meta-analysis. *Clinical Gastroenterology and Hepatology*, *11*(12), 1573–1584.

Singh, S., Fujii, L. L., Murad, M. H., Wang, Z., Asrani, S. K., Ehman, R. L., … Talwalkar, J. A. (2014). Liver stiffness is associated with risk of decompensation, liver cancer, and death in patients with chronic liver diseases: A systematic review and meta-analysis. *Clinical Gastroenterology and Hepatology*, *11*(12), 1573–1584.

Sockolosky, J. T., Dougan, M., Ingram, J. R., Ho, C. C. M., Kauke, M. J., Almo, S. C., … Garcia, K. C. (2016). Durable antitumor responses to CD47 blockade require adaptive immune stimulation. *Proceedings of the National Academy of Sciences*, *113*(19), 201604268.

Sosale, N. G., Ivanovska, I. I., Tsai, R. K., Swift, J., Hsu, J. W., Alvey, C. M., … Discher, D. E. (2016). "Marker of Self" CD47 on lentiviral vectors decreases macrophage-mediated clearance and increases delivery to SIRPA-expressing lung carcinoma tumors. *Molecular Therapy — Methods & Clinical Development*, *3*(October), 16080.

Sosale, N. G., Rouhiparkouhi, T., Bradshaw, A. M., Dimova, R., Lipowsky, R., & Discher, D. E. (2015). Cell rigidity and shape override CD47's " self " signaling in phagocytosis by hyperactivating myosin-II. *Blood*, *125*(3).

Spencer, V. A., Xu, R., & Bissell, M. J. (2007). Extracellular matrix, nuclear and chromatin structure, and gene expression in normal tissues and malignant tumors: A work in progress. *Advanced Cancer Research*, *97*, 275–294.

Steitz, J., Brück, J., Steinbrink, K., Alexander, E., Knop, J., & Tüting, T. (2000). Genetic immunization of mice with human tyrosinase-related protein 2: Implications for the immunotherapy of melanoma. *International Journal of Cancer*, *86*(1), 89–94.

Strickland, K. C., Howitt, B. E., Shukla, S. A., Rodig, S., Ritterhouse, L. L., Liu, J. F., … Konstantinopoulos, P. A. (2016). Association and prognostic significance of BRCA1/2-mutation status with neoantigen load, number of tumor-infiltrating lymphocytes and expression of PD-1/PD-L1 in high grade serous ovarian cancer. *Oncotarget*, *7*(12), 13587–13598.

Subramanian, S., Parthasarathy, R., Sen, S., Boder, E. T., & Discher, D. E. (2006). Species- and cell type-specific interactions between CD47 and human SIRPa. *Blood*, *107*(6), 2548–2556.

Swamydas, M., Luo, Y., Dorf, M. E., & Lionakis, M. S. (2015). Isolation of mouse neutrophils. *Current Protocols in Immunology*, *2015*, 3.20.1-3.20.15.

Swift, J., Ivanovska, I. L., Buxboim, A., Harada, T., Dingal, D. P., Pinter, J. J., … Discher, D. E. (2013a). Nuclear Lamin-A Scales with Tissue Stiffness and Enhances Matrix-Directed Differentiation. *Science*, *341*, 1–15.

Swift, J., Ivanovska, I. L., Buxboim, A., Harada, T., Dingal, P. C. D. P., Pinter, J., … Discher, D. E. (2013b). Nuclear lamin-A scales with tissue stiffness and enhances matrix-directed differentiation. *Science*, *341*, 1240104.

Takimoto, C. (2014). Phase 1 Trial of Hu5F9-G4, a CD47-targeting Antibody.

Clinicaltrial.gov.
Takimoto, C. (2016). Trial of Hu5F9-G4 in Combination With Cetuximab in Patients With Solid Tumors and Advanced Colorectal Cancer. *Clinicaltrial.gov*.
Tamiello, C., Kamps, M. A. F., van den Wijngaard, A., Verstraeten, V. L. R. M., Baaijens, F. P. T., Broers, J. L. V, & Bouten, C. C. V. (2013). Soft substrates normalize nuclear morphology and prevent nuclear rupture in fibroblasts from a laminopathy patient with compound heterozygous LMNA mutations. *Nucleus*, *4*(1), 61–73.
Thiam, H.-R., Vargas, P., Carpi, N., Crespo, C. L., Raab, M., Terriac, E., … Piel, M. (2016). Perinuclear Arp2/3-driven actin polymerization enables nuclear deformation to facilitate cell migration through complex environments. *Nature communications*, *7*, 1–14.
Tomasetti, C., Li, L., & Vogelstein, B. (2017). Stem cell divisions, somatic mutations, cancer etiology, and cancer prevention. *Science*, *355*, 1330–1334.
Tsai, R. K., & Discher, D. E. (2008). Inhibition of "self" engulfment through deactivation of myosin-II at the phagocytic synapse between human cells. *The Journal of cell biology*, *180*(5), 989–1003.
Tseng, D., Volkmer, J.-P., Willingham, S. B., Contreras-Trujillo, H., Fathman, J. W., Fernhoff, N. B., … Weissman, I. L. (2013). Anti-CD47 antibody-mediated phagocytosis of cancer by macrophages primes an effective antitumor T-cell response. *Proceedings of the National Academy of Sciences of the United States of America*, *110*(27), 11103–8.
Turrini, F., Arese, P., Yuan, J., & Low, P. S. (1991). Clustering of integral membrane proteins of the human erythrocyte membrane stimulates autologous IgG binding, complement deposition, and phagocytosis. *Journal of Biological Chemistry*, *266*(35), 23611–23617.
Turtle, C. J., Hanafi, L.-A., Berger, C., Gooley, T. A., Cherian, S., Hudecek, M., … Maloney, D. G. (2016). CD19 CAR-T cells of defined CD4+:CD8+ composition in adult B cell ALL patients. *The Journal of Clinical Investigation*, *126*(6), 2123–2138.
Veltman, D. M., Lemieux, M. G., Knecht, D. A., & Insall, R. H. (2014). PIP3-dependent macropinocytosis is incompatible with chemotaxis. *Journal of Cell Biology*, *204*(4), 497–505.
Verdegaal, E. M. E., de Miranda, N. F. C. C., Visser, M., Harryvan, T., van Buuren, M. M., Andersen, R. S., … van der Burg, S. H. (2016). Neoantigen landscape dynamics during human melanoma–T cell interactions. *Nature*, *536*, 91–95.
von Zglinicki, T., Saretzki, G., Ladhoff, J., d'Adda di Fagagna, F., & Jackson, S. P. (2005). Human cell senescence as a DNA damage response. *Mechanisms of Ageing and Development*, *126*, 111–117.
Wang, Y., Xu, Z., Guo, S., Zhang, L., Sharma, A., Robertson, G. P., & Huang, L. (2013). Intravenous delivery of siRNA targeting CD47 effectively inhibits melanoma tumor growth and lung metastasis. *Molecular therapy : the journal of the American Society of Gene Therapy*, *21*(10), 1919–29.
Weiskopf, K., Ring, A. M., Ho, C. C. M., Volkmer, J.-P., Levin, A. M., Volkmer, A. K., … Garcia, K. C. (2013). Engineered SIRPa variants as immunotherapeutic

adjuvants to anticancer antibodies. *Science*, *341*, 88–91.
Weiskopf, K., Ring, A. M., Ho, C. C. M., Volkmer, J.-P., Levin, A. M., Volkmer, A. K., … Garcia, K. C. (2013a). Engineered SIRPα variants as immunotherapeutic adjuvants to anticancer antibodies. *Science (New York, N.Y.)*, *341*(6141), 88–91.
Weiskopf, K., Ring, A. M., Ho, C. C. M., Volkmer, J.-P., Levin, A. M., Volkmer, A. K., … Garcia, K. C. (2013b). Supplement: Engineered SIRPα variants as immunotherapeutic adjuvants to anticancer antibodies. *Science (New York, N.Y.)*, *341*, 88–91.
Wick, D. A., Webb, J. R., Nielsen, J. S., Martin, S. D., Kroeger, D. R., Milne, K., … Nelson, B. H. (2014). Surveillance of the tumor mutanome by T cells during progression from primary to recurrent ovarian cancer. *Clinical Cancer Research*, *20*(5), 1125–1134.
Wilflingseder, D., Banki, Z., Garcia, E., Pruenster, M., Pfister, G., Muellauer, B., … Stoiber, H. (2007). IgG opsonization of HIV impedes provirus formation in and infection of dendritic cells and subsequent long-term transfer to T cells. *Journal of immunology (Baltimore, Md. : 1950)*, *178*(12), 7840–7848.
Willingham, S. B., Volkmer, J.-P., Gentles, A. J., Sahoo, D., Dalerba, P., Mitra, S. S., … Weissman, I. L. (2012). The CD47-signal regulatory protein alpha (SIRPa) interaction is a therapeutic target for human solid tumors. *Proceedings of the National Academy of Sciences of the United States of America*, *109*(17), 6662–7.
Xu, W., Mezencev, R., Kim, B., Wang, L., Mcdonald, J., & Sulchek, T. (2012). Cell stiffness is a biomarker of the metastatic potential of ovarian cancer cells. *PLOS ONE*, *7*(10), e46609.
Yanagita, T., Murata, Y., Tanaka, D., Motegi, S., Arai, E., Daniwijaya, E. W., … Matozaki, T. (2017). Anti-SIRPα antibodies as a potential new tool for cancer immunotherapy. *JCI Insight*, *2*(1), 1–15.
Yang, Y., Leone, L. M., & Kaufman, L. J. (2009). Elastic moduli of collagen gels can be predicted from two-dimensional confocal microscopy. *Biophysical Journal*, *97*(7), 2051–2060.
Yi, T., Li, J., Chen, H., Wu, J., An, J., Xu, Y., … Cyster, J. G. (2015). Splenic Dendritic Cells Survey Red Blood Cells for Missing Self-CD47 to Trigger Adaptive Immune Responses. *Immunity*, *43*(4), 764–775.
Zhang, H., Lu, H., Xiang, L., Bullen, J. W., Zhang, C., Samanta, D., … Semenza, G. L. (2015). HIF-1 regulates CD47 expression in breast cancer cells to promote evasion of phagocytosis and maintenance of cancer stem cells. *Proceedings of the National Academy of Sciences*, *112*(45), E6215–E6223.
Zhang, M., Hutter, G., Kahn, S. A., Azad, T. D., Gholamin, S., Xu, C. Y., … Cheshier, S. H. (2016). Anti-CD47 treatment stimulates phagocytosis of glioblastoma by M1 and M2 polarized macrophages and promotes M1 polarized macrophages in vivo. *PLoS ONE*, *11*(4), 1–21.
Zhang, Y., Cheng, S., Zhang, M., Zhen, L., Pang, D., Zhang, Q., & Li, Z. (2013). High-Infiltration of Tumor-Associated Macrophages Predicts Unfavorable Clinical Outcome for Node-Negative Breast Cancer. *PLoS ONE*, *8*(9), 1–8.
Zhu, D., Pan, C., Li, L., Bian, Z., Lv, Z., Shi, L., … Zen, K. (2013). MicroRNA-17/20a/106a modulate macrophage inflammatory responses through targeting

signal-regulatory protein alpha. *Journal of Allergy and Clinical Immunology*, *132*(2), 426–436.e8.

Zoon, C. K., Wan, W., Graham, L., & Bear, H. D. (2015). Addition of interleukin-21 for expansion of T-cells for adoptive immunotherapy of murine melanoma. *International Journal of Molecular Sciences*, *16*(4), 8744–8760.